School of Civil, Environmental and Mining Engineering

Thesis submitted for the Degree of Doctor of Philosophy (PhD)

Experimental and Numerical Analysis of Rolling Dynamic Compaction

Yue Chen

October 2021

This thesis is dedicated to my mother.

Table of Contents

List of Figures

List of Tables

Abstract

Rolling dynamic compaction (RDC) is a ground improvement technique, which involves towing heavy (typically 6–15 tonnes) non-circular modules (3-, 4- and 5-sided) behind a towing unit to achieve soil compaction. RDC has gained increased popularity in recent years since it has a greater influence depth and it can be operated at a higher speed. Although RDC has been successfully applied to many construction projects, there is currently very limited understanding of the behaviour of soil beneath the ground during the RDC process. In addition, the relationships between soil response and the effectiveness of RDC are still not well understood. These often results in the use of RDC being based on intuition or experience obtained from previous projects with similar soils and site conditions.

To address the current knowledge gap, this research aims to quantify the soil response during the RDC process and then investigate the relationships between the mechanism of soil movement and the effects of RDC. This research focusses solely on the 4-sided impact roller. A series of physical scale model tests with the use of transparent soils, high speed photography and the image correlation technique were conducted to capture soil internal displacements subjected to RDC in real-time. The soil displacement field during the RDC process was measured and quantified. The loading and unloading response of soil subjected to a single roller impact was investigated and reported. In addition, the effects of operating speed and module mass on the internal displacements of the soil were determined. It was found that operating speed influenced soil displacements and the depth of improvement of the roller, and speeds between 12–14 km/h were recommended as the optimum operating speed. Soil displacements and improvement depth increased as speed rose to the optimal operating speed. After that, both soil displacements and improvement depth showed no further improvement and may even decrease due to the changes in the

kinematics of the roller. In addition, the heavier roller induced greater soil displacements at each operating speed.

A numerical scale model was developed and validated against physical scale model tests using the combined finite element method (FEM) and discrete element method (DEM) approach to simulate ground improvement induced by RDC. The numerical results were in good agreement with laboratory results. Relationships between porosity variations, soil movement and the motion of the roller were assessed using the developed numerical model. Porosities were also plotted against the number of passes, with the number of passes of approximately 35 found to be optimum. The numerical scale model was also modified, upscaled and compared against field measurements. It was found that the numerical scale model was able to provide reasonable predictions of ground improvement due to RDC, which offered the potential of obtaining an estimation of the performance of RDC before its application in practice.

Finally, a numerical parametric study was performed to evaluate the effects of module mass, operating speed and various ground conditions on the effectiveness of RDC based on some aspects that are difficult to be measured in field tests. The results show that a heavier roller and a faster operating speed deliver greater compactive energies to the ground. The modelling results suggest that soil with a higher initial Young's modulus and a higher internal angle of friction decreases the magnitude of soil displacements, which confirms that the impact roller is less able to significantly improve soils that are stiff or have a high initial shear strength.

It is concluded that the proposed physical scale model captures the internal soil response during the RDC process, which provides greater insight into the mechanisms of soil

movement due to RDC. This work expands the current knowledge of RDC theory and improves the confidence of RDC applications. The developed numerical model has demonstrated abilities in predicting ground improvement induced by RDC, which indicates the potential of applying the numerical model in predicting the performance of RDC and planning RDC-related ground improvement projects. In addition, the numerical model further evaluates the ground response subjected to RDC, which allows the effectiveness of RDC to be assessed from several aspects that are difficult to be measured using conventional investigation methods. In general, the results of this research provide a better understanding of the effectiveness of RDC, which are likely to reduce design conservatism, such as, excessive compaction requirements and overestimated costs, and also accelerate the adoption of RDC in ground improvement projects worldwide.

Statement of Originality

I certify that this work contains no material which has been accepted for the award of any other degree or diploma in my name, in any university or other tertiary institution and, to the best of my knowledge and belief, contains no material previously published or written by another person, except where due reference has been made in the text. In addition, I certify that no part of this work will, in the future, be used in a submission in my name, for any other degree or diploma in any university or other tertiary institution without the prior approval of the University of Adelaide and where applicable, any partner institution responsible for the joint-award of this degree.

The author acknowledges that copyright of published works contained within the thesis resides with the copyright holder(s) of those works.

I also give permission for the digital version of my thesis to be made available on the web, via the University's digital research repository, the Library Search and also through web search engines, unless permission has been granted by the University to restrict access for a period of time.

Signature: Date: 19/10/2021

Acknowledgements

First and foremost, I would like to express my sincere gratitude to my primary supervisor, Professor Mark Jaksa from the School of Civil, Environmental and Mining Engineering at the University of Adelaide, for his invaluable advice, motivation, continuous support and patience during my Ph.D. study. His immense knowledge and plentiful experience have helped me in all the time of my research and daily life. He always gave his time to offer me valuable comments to improve my work. Mark has stimulated my interest in geotechnical engineering through a fourth-year course, which inspired me to pursue a higher degree of research on geotechnical engineering. I still remember how nervous I was when I sent an email to him to seek his supervision towards the Ph.D. degree, and how lucky I felt when he agreed to be my supervisor. As a supervisor, he has helped and taught me more than I could ever give him credit for here. I could not have imagined having a better supervisor!

I would like to extend my gratitude to my co-supervisors, Drs. Yien Lik Kuo and Brendan Scott from the School of Civil, Environmental and Mining Engineering at the University of Adelaide, for their countless hours of help, support and advice throughout my Ph.D. candidature. Yien Lik has offered me great help with my experimental tests, in terms of test designs and setup. Brendan has shared his knowledge, valuable suggestions and the field test databases with me, which were really influential in shaping the direction of my research and critiquing my results. I would not have the opportunity to extend my research on the scale model tests to the field scale without his comments, encouragement and support.

I wish to acknowledge the School of Civil, Environmental and Mining Engineering, particularly Mr. Gary Bowman, for his support and advice on the experimental work.

I would like to thank my friends and colleagues who I have met during my candidature. They have offered me kind support and encouragement throughout my Ph.D. study. Some of them have completed their Ph.D. degrees and commenced work, and I wish them every success in their careers. Some of them are still completing their Ph.D. studies, and I wish them all the best with their research.

I wish to deeply thank my parents and my sister, for their constant love and support. Thank you for your understanding, encouragement and for always being there for me. Your support has meant more to me than you could ever imagine.

Last but not least, I would like to thank my husband, Junfu (Jeffrey) Li, for being so supportive during my candidature. Thank you for your company, timely encouragement, understanding and love, which helped me get through the hard times in the most positive way during my candidature. It is a great pleasure to share my life with you.

Chapter 1.

Introduction

1.1 Introduction

Rolling dynamic compaction (RDC) is a ground improvement technique, which is capable of increasing strength and stiffness of the soil and reducing the soil's settlements and permeability by mechanically applied energy (Ranjan and Rao, 2007). It involves the use of heavy, non-circular modules (typically 6–15 tonnes and 3-, 4- and 5-sided) behind a towing unit. The modules rotate about their corners and fall repeatedly to compact the ground as they are towed forward. During the compaction process, the compactive energy delivered to the ground by RDC consists of three aspects namely, the potential energy from the self-weight of the modules; the additional potential energy from the modules being lifted about their corners, and the kinetic energy derived from the towing unit. Due to the relatively large module weight and the greater amount of compactive energy on to the ground, when compared with the conventional smooth drum rollers, which influence soil depths of less than 0.5 m, RDC improves the ground to a greater depth (1–3 m) (Clifford, 1976, 1978; Avalle and Carter, 2005; Jaksa et al., 2019). In addition, RDC traverses the ground at speeds of 9–12 km/h, which is faster than traditional compaction methods, for example, the traditional drum roller, which travels at a speed of 4 km/h (Pinard, 1999). Due to the deeper compactive depth and the greater operating speed, RDC has been successfully applied to several earthworks construction projects, such as, in situ densification of existing fills, large reclamation projects, reconstruction of rural roads and mining and agricultural related applications (Avalle and Carter, 2005; Avalle and McKenzie, 2005; Bouazza and Avalle, 2006).

To date, the effectiveness of the 4-sided impact roller has been assessed by several researchers by means of field tests (Avalle and Carter, 2005; Jaksa et al., 2012; Scott and Jaksa, 2014; Scott and Jaksa, 2015; Bradley et al., 2019; Scott et al., 2019a, 2019b, 2020), experimental scale model tests (Rajarathnam et al., 2016; Chung et al., 2017), numerical

simulations (Kim, 2011; Kuo et al., 2013) and machine learning (Ranasinghe et al., 2017a; Ranasinghe et al., 2017b, 2019). The depth of influence, ground settlements, the energy delivered to the ground and the effects of operating speed and the number of passes have been investigated and reported in these studies. Previous studies are valuable for understanding the behaviour of the 4-sided impact roller, however, there are still significant gaps and limitations in the previous research, which are discussed below.

Firstly, there is currently limited published information regarding the internal soil deformation within the soil body under RDC. Quantifying internal soil displacements could reflect the dynamic effects of the roller compacting the ground in real-time, therefore, soil internal displacement is considered as a direct indicator of the efficacy of RDC. However, as natural soil is opaque, it is difficult to measure internal soil displacements in field and conventional experimental scale model tests, which results in the limited understanding of internal soil response beneath the ground. Accelerometers and earth pressure cells (EPCs) are two currently available techniques that can be used in field and experimental scale model tests to help understand the soil response beneath the ground during the RDC process. The use of accelerometers and EPCs, is considered as an intrusive technique since they need to be buried within the soil body at different depths of interest to measure accelerations and pressures induced by RDC. In addition, both accelerometers and EPCs are constructed using small metal plates, which have different material properties to the surrounding soil, that may affect the soil response. Therefore, there is a need to develop a new approach to observe and quantify the internal soil response under RDC.

Secondly, as conducting field and experimental scale model tests requires a great amount of time and effort to prepare and carry out the tests, numerical simulations have been

adopted by several researchers, such as Kim (2011) and Kuo et al. (2013), to investigate ground response induced by the roller. In their models, the soil and the roller were simulated using the finite element method (FEM). The limitation of Kim's study was that the obtained numerical results were not validated against field data. The Kuo et al. (2013) numerical model was validated against field results and it was reported that, the model was capable of simulating soil displacements, pressures delivered by the roller and the depth of influence of RDC. Although, the FEM model has demonstrated capabilities to simulate ground improvement induced by the roller, the motion of individual soil particles and the porosity changes within the soil body are still elusive, given the limitations of the nature of continuum based methods, for example, FEM. This thesis introduces a new method, which combines the FEM and discrete element method (DEM) in a single numerical model to simulate the response of granular soil particles under RDC.

Thirdly, there is a need to investigate factors that affect the performance of RDC and then provide practical recommendations for applications of RDC. In order to quantify the effects of a single factor on ground improvement results, homogeneous soil conditions are required in field and experimental scale model tests to ensure the accuracy of test results, which significantly increases the difficulties and costs in test preparation. Therefore, this research quantifies the effects of module mass, operating speed and varying ground conditions on the effectiveness of the 4-sided roller using the developed numerical model.

1.2 Aim and objectives of thesis

This research aims to quantify the behaviour of soil with respect to the motion of the 4-sided impact roller and to investigate the relationships between soil response and the effectiveness of RDC. It initially focuses on the measurement of internal soil

displacements within the soil body induced by RDC through experimental scale model tests. It then focuses on the development of a numerical model in simulating the soil response beneath the roller. This provides a greater understanding of the ground response subjected to RDC and improves the efficiency and confidence in the practical applications of RDC. To help achieve these aims, the following research objectives are identified:

1. To develop a physical scale model using transparent soils, high speed photography and the particle image velocimetry technique. This model will capture internal soil displacements during the RDC process to provide greater insight into RDC-influenced ground improvement.
2. To determine the effects of operating speed and module mass on soil internal displacements induced by the 4-sided roller using the results obtained from [1].
3. To explore the use of the combined FEM-DEM approach in simulating the movements of soil particles and porosity variations during the RDC process. The numerical model will help to investigate the relationships between porosity variations, soil displacements and the motion of the roller.
4. To upscale the results of the numerical scale model, and then validate them against a field study that was conducted using the full-size RDC. The numerical results will be analysed and compared against each other to obtain an efficient indicator, which can be used to estimate ground improvement induced by RDC and to quantify the optimum number of passes of RDC.
5. To evaluate the effects of a range of parameters on ground improvement by RDC and then provide practical recommendations for RDC applications. In the numerical model, parameters that affect the ground response can be varied and controlled with relative ease and the effectiveness of RDC is able to be quantified

from some aspects that are difficult to be measured in field and experimental scale model tests.

1.3 Layout of thesis

This thesis consists of six chapters, which detail the research undertaken to investigate the performance of RDC by means of experimental scale model tests and numerical simulations. The current chapter, **Chapter 1**, provides the general background of RDC and introduces the research gaps, aims and objectives, and the thesis layout. **Chapters 2–5** include three published journal papers and one submitted journal paper, which address the five identified research gaps stated above.

Chapter 2 includes the first published journal paper entitled "Experimental Analysis of Rolling Dynamic Compaction Using Transparent Soils and Particle Image Velocimetry". This paper presents the development of the novel, physical scale model, which includes the selection of experimental materials, sample preparation, the experimental setup and the calibration tests. The real-time soil internal displacements relative to the motion of the roller are measured and analysed using high speed photography and the particle image velocimetry technique. The evolution of soil deformation and the influence of operating speed and module mass on ground improvement are then investigated and discussed. This paper provides the dynamic response of the soil beneath the ground during the RDC process and offers the potential for applying transparent soils to the investigation of ground improvement techniques. Details of this publication are as follows:

Chen, Y., Jaksa, M., Kuo, Y., Airey, D. 2021. Experimental Analysis of Rolling Dynamic Compaction Using Transparent Soils and Particle Image Velocimetry. *Canadian Geotechnical Journal*, Available from http://dx.doi.org/10.1139/cgj-2020-0573.

Chapter 3 includes the second published paper entitled "Investigating the Effectiveness of Rolling Dynamic Compaction (RDC) Using Discrete Element Method (DEM)". This paper proposes a three-dimensional finite element method (FEM)-discrete element method (DEM) model, which simulates the movement of soil particles and porosity variations beneath the roller. The numerical model is developed according to the physical scale model tests that were conducted in Chapter 2, and the numerical results are in good agreement with the experimental results. The performance of the 4-sided roller is then assessed based on the soil porosity variations and soil velocity vectors obtained from the numerical model. The details of this publication are as follows:

Chen, Y., Jaksa, M.B., Kuo, Y.L., Airey, D.W. 2021. Investigating the Effectiveness of Rolling Dynamic Compaction (RDC) Using Discrete Element Method (DEM). *Granular Matter*, Available from https://doi.org/10.1007/s10035-021-01164-9.

Chapter 4 includes the third published paper entitled "Discrete element modelling of the 4-sided impact roller". In this paper, the developed numerical scale model is upscaled to the full-size RDC scale and then validated against a field study that was conducted using the corresponding full-size RDC. The ground settlement, soil displacements at different depths of interest, pressures measured at each roller pass and the depth of improvement obtained from the numerical model are analysed and evaluated to obtain an efficient indicator to estimate ground improvement due to RDC and to determine the optimum number of passes. The details of this publication are as follows:

Chen, Y., Jaksa, M., Kuo, Y., Scott, B. 2021. Discrete element modelling of the 4-sided impact roller. *Computers and Geotechnics*, Available from https://doi.org/10.1016/j.compgeo.2021.104250.

Chapter 5 includes a submitted paper entitled "A parametric study of the 4-sided impact roller". This paper builds on the work undertaken in Chapter 4 and further investigates the effects of a range of parameters on ground improvement by RDC, such as the operation of RDC, the characteristics of RDC and the ground conditions. A series of simulations are performed using the developed FEM-DEM model to study the behaviour of RDC with increasing operating speeds, two different module masses and various ground conditions. This paper also proposes practical recommendations for applications of RDC. The details of this publication are as follows:

Chen, Y., Jaksa, M., Scott, B., Kuo, Y. 2021. A parametric study of the 4-sided impact roller. *Acta Geotechnica*, https://doi.org/x.

Finally, **Chapter 6** summarises the conclusions and findings obtained as a result of the research undertaken for this thesis, along with presenting recommendations for future work.

1.4 References

Avalle, D., Carter, J. 2005. Evaluating the improvement from impact rolling on sand. Proc. 6th Int. Conf. on Ground Improvement Techniques, Coimbra, Portugal, pp. 8.

Avalle, D. L., Mckenzie, R. W. 2005. Ground improvement of landfill site using the square impact roller. Australian Geomechanics, 40, 15-21.

Bouazza, A., Avalle, D. L. 2006. Effectiveness of rolling dynamic compaction on an old waste tip. ISSMGE 5th International Congress on Environmental Geotechnics, Cardiff, pp. 1-7.

Bradley, A. C., Jaksa, M. B., Kuo, Y.-L. 2019. Examining the kinematics and energy of the four-sided impact roller. Proceedings of the Institution of Civil Engineers - Ground Improvement, 172, 297-304.

Chung, O., Scott, B., Jaksa, M., Kuo, Y., Airey, D. 2017. Physical modeling of rolling dynamic compaction. Proceedings of the 19th Int. Conf. on Soil Mechanics and Geotechnical Engineering, Seoul, Korea, Sept. 18–22, 905–908.

Clifford, J. 1976. Impact rolling and construction techniques. Australian Road Research Board Conference Proc.

Clifford, J. 1978. The impact roller-problems solved. Civil Engineering= Siviele Ingenieurswese, 20, pp. 321-324.

Jaksa, M. B., Airey, D. W., Scott, B. T., Kuo, Y. L., Ranasinghe, R. A. T. M., Bradley, A. C., Chung, O. Y., Li, Y., Chen, Y. 2019. Quantifying the Effect of Rolling Dynamic Compaction. *In* Proceedings of the 4th World Congress on Civil, Structural, and Environmental Engineering. Rome, Italy. doi: 10.11159/icgre19.1.

Jaksa, M. B., Scott, B. T., Mentha, N., Symons, A., Pointon, S., Wrightson, P., Syamsuddin, E. 2012. Quantifying the zone of influence of the impact roller. *In* Proceedings of ISSMGE-TC 211 International Symposium on Ground Improvement, Brussels, Belgium, 30 May – 1 June, Vol. 2, pp. 41–52.

Kim, K. 2011. Numerical simulation of impact rollers for estimating the influence depth of soil compaction. Dissertation in partial fulfilment of the requirements for the degree of Master of Science, Texas A & M University.

Kuo, Y., Jaksa, M., Scott, B., Bradley, A., Power, C., Crisp, A., Jiang, J. 2013. Assessing the effectiveness of rolling dynamic compaction. *In* Proceedings of the 18th International Conference on Soil Mechanics and Geotechnical Engineering, Paris., vol. 2, pp. 1309–1312.

Pinard, M. 1999. Innovative developments in compaction technology using high energy impact compactors. Proceedings 8th Australia New Zealand Conference on Geomechanics: Consolidating Knowledge. Australian Geomechanics Society, pp. 775-781.

Rajarathnam, P., Masoudian, M. S., Airey, D. W., Jaksa, M. B. 2016. Model tests of rolling dynamic compaction. Proc. 19th Southeast Asian Geotechnical Conf. and 2nd AGSSEA Conf. Kuala Lumpur, May 31 – June 3. pp. 505–510.

Ranasinghe, R., Jaksa, M., Kuo, Y., Nejad, F. P. 2017a. Application of artificial neural networks for predicting the impact of rolling dynamic compaction using dynamic cone penetrometer test results. Journal of Rock Mechanics and Geotechnical Engineering, 9, pp. 340-349.

Ranasinghe, R., Jaksa, M., Nejad, F. P., Kuo, Y. 2019. Prediction of the effectiveness of rolling dynamic compaction using artificial neural networks and cone penetration test data. Chinese Journal of Rock Mechanics and Engineering, 38, pp. 153-170.

Ranasinghe, R. A. T. M., Jaksa, M. B., Pooya Nejad, F., Kuo, Y. L. 2017b. Predicting the effectiveness of rolling dynamic compaction using genetic programming. Proceedings of the Institution of Civil Engineers-Ground Improvement, 170, pp. 193-207.

Ranjan, G., Rao, A. 2007. Basic and applied soil mechanics, New Age International.

Scott, B., Jaksa, M. 2014. Evaluating rolling dynamic compaction of fill using CPT. *In* Proceedings of the 3rd International Symposium on Cone Penetration Testing, pp. 941-948.

Scott, B., Jaksa, M., Mitchell, P. 2019a. Depth of influence of rolling dynamic compaction. Proceedings of the Institution of Civil Engineers-Ground Improvement, pp. 1-10.

Scott, B., Jaksa, M., Mitchell, P. 2019b. Ground response to rolling dynamic compaction. Géotechnique Letters, 9, pp. 99-105.

Scott, B. T., Jaksa, M. B. 2015. A field based study of the effec tiveness of rolling dynamic compaction. Ground Improvement Case Histories: Compaction, Grouting and Geosynthetics, Ed. I ndraratna, Chu & Rujikiatkamjorn, pp. 429-452.

Scott, B. T., Jaksa, M. B., Mitchell, P. W. 2020. Influence of towing speed on effectiveness of rolling dynamic compaction. Journal of Rock Mechanics and Geotechnical Engineering, 12, pp. 126-134.

Chapter 2.

Experimental Analysis of Rolling Dynamic Compaction Using Transparent Soils and Particle Image Velocimetry

Statement of Authorship

Title of Paper	Experimental Analysis of Rolling Dynamic Compaction Using Transparent Soils and Particle Image Velocimetry
Publication Status	☑ Published ☐ Accepted for Publication ☐ Submitted for Publication ☐ Unpublished and Unsubmitted w ork w ritten in manuscript style
Publication Details	Chen, Y., Jaksa, M., Kuo, Y., Airey, D. 2021. Experimental Analysis of Rolling Dynamic Compaction Using Transparent Soils and Particle Image Velocimetry. Canadian Geotechnical Journal, Available from http://dx.doi.org/10.1139/cgj-2020-0573.

Principal Author

Name of Principal Author (Candidate)	Yue Chen		
Contribution to the Paper	Performed experimental work, analysis and interpretation of experimental data, wrote manuscript.		
Overall percentage (%)	80%		
Certification:	This paper reports on original research I conducted during the period of my Higher Degree by Research candidature and is not subject to any obligations or contractual agreements with a third party that would constrain its inclusion in this thesis. I am the primary author of this paper.		
Signature		Date	08 October 2021

Co-Author Contributions

By signing the Statement of Authorship, each author certifies that:

i. the candidate's stated contribution to the publication is accurate (as detailed above);
ii. permission is granted for the candidate in include the publication in the thesis; and
iii. the sum of all co-author contributions is equal to 100% less the candidate's stated contribution.

Name of Co-Author	Mark Jaksa		
Contribution to the Paper	Provided primary supervision, initial concept, contributed to the methodology, helped evaluate and edit the manuscript.		
Signature		Date	15/10/21

Name of Co-Author	Yien Lik Kuo		
Contribution to the Paper	Provided secondary supervision, assisted with research direction, helped edit the manuscript.		
Signature		Date	08 Oct 2021

Please cut and paste additional co-author panels here as required.

Name of Co-Author	David Airey		
Contribution to the Paper	Assisted with research direction, helped edit the manuscript.		
Signature		Date	15/10/2021

Please cut and paste additional co-author panels here as required.

Experimental Analysis of Rolling Dynamic Compaction Using Transparent Soils and Particle Image Velocimetry (Paper 1)

Abstract

Rolling Dynamic Compaction (RDC) is a soil compaction technique, which is capable of improving thick layers of soil at a relatively fast operating speed. The paper presents the results of laboratory experiments conducted on 1:13 scale models of the 4-sided, 8- and 12-tonne, Broons BH-1300 and BH-1300 HD impact rollers to study the performance of the scale model at four different operating speeds. A series of laboratory tests are undertaken using transparent soils and the particle image velocimetry (PIV) technique to investigate the effectiveness of the models. The transparent soil employed in this study consists of fused quartz and a pore fluid which matched the refractive index of the fused quartz. A one-particle thick layer of coloured fused quartz is embedded in the centre plane of the transparent soil to visualise soil internal displacements and a digital camera is used to capture the speckled pattern during the scale model testing process. The results show that the heavier module induces greater soil displacements at each operating speed. The optimal operating speed is approximately 299 mm/s for both module weights. The most significant soil displacements occur within the first 20 passes and, no obvious ground improvement is observed after 35 passes. The results of this study demonstrate the unique capability of transparent soil to study soil displacements induced by the ground improvement scale models.

2.1 Introduction

The stability and serviceability of foundations are highly dependent on the bearing capacity and settlement of the underlying soil. With the global increase in population and the consequent growing demand for land for housing and development, construction on soft, weak, compressible and filled ground is becoming increasingly prevalent. Hence,

ground improvement has become an important and common component of civil engineering construction. Compaction is commonly employed as it is the most cost-effective ground improvement approach. The density of soil is improved by applying mechanical energy to reduce the volume of the voids. Based on the type of compactive effort, compaction is divided into static and dynamic methods. Static compaction involves the densification of the ground by gradually applying the self-weight of heavy machinery. In contrast, dynamic compaction involves, in addition to self-weight, the application of repeated high energy impact forces.

Rolling dynamic compaction (RDC) is a form of dynamic compaction. It involves towing a heavy, non-circular module (typically 6-12 tonnes and 3-, 4- or 5-sided) behind a tractor, such that the module rotates about its corners and falls repeatedly to impact the ground. It improves the sub-surface profile to a greater depth (1–3 m) when compared with conventional static and vibratory compaction. RDC is particularly efficient in large, open sites as it can be operated at a greater speed (10–12 km/h) when compared with the 4 km/h of traditional compaction equipment (Pinard 1999). The deeper compactive depth and greater operating speed result in the extensive use of RDC in earthworks construction, such as, in situ densification of existing fills, large reclamation projects, reconstruction of rural roads and mining and agricultural related applications (Avalle and Carter 2005; Avalle and McKenzie 2005; Bouazza and Avalle 2006). Because of the greater induced energy, ground vibrations are generated during the compaction process which may cause potential hazards to nearby structures, particularly those vulnerable to vibrations, such as older heritage structures. Therefore, a buffer zone of approximately 2–5 m is recommended for industrial buildings, and a 7–20 m zone is suggested for residential buildings when adopting the 4-sided, 8-tonne module (Avalle 2007). In addition, Avalle (2006) reported that, the ground surface becomes undulating and the upper ground surface

is loosened after RDC compaction due to the geometry of the module. Therefore, a grader and a conventional circular roller are generally used to level and compact the soil near the ground surface after the application of RDC.

Field tests have been undertaken to examine the energy transfer, the zone of influence and the surface settlement of RDC (Jaksa et al. 2012; Scott and Jaksa 2014). As conducting field tests is costly and time-consuming, physical scale models have been utilised in controlled laboratory environments to quantify the performance of RDC with respect to different soil types, roller speeds and masses (Rajarathnam et al. 2016; Chung et al. 2017; Li et al. 2020). These studies have shown that physical scale models can produce similar ground response to that of the full-size modules. Previous studies are valuable for understanding the behaviour of RDC, however, it is difficult to assess the soil response, such as the internal soil displacement, depth of improvement and ground settlement.

The internal deformation of soil within a mass under RDC has long been a topic of interest, since soil displacements are considered as a direct indicator of the effectiveness of RDC. However, as natural soil is opaque, the displacement of soil within the soil body is difficult to observe and quantify. Accelerometers and earth pressure cells have been used in field (Scott et al. 2019) and scale model (Chung et al. 2017; Jaksa et al. 2019) testing in an effort to measure ground improvement. Soil displacements were calculated by double integrating the obtained acceleration with respect to time. The use of accelerometers is, however, an intrusive technology as they need to be embedded into the soil body at different depths to measure ground accelerations. Accelerometers are constructed using small metal plates that might affect the displacement response of the surrounding soil due to different material properties of the sensors with respect to the soil.

Other technologies like radiography, computerised axial tomography (CAT) and magnetic resonance imaging (MRI) have been employed by several researchers to examine various geotechnical problems (e.g. Bransby and Milligan 1975; Mandava et al. 1990; Posadas et al. 1996), but these are limited in their ability to investigate rapid loading events. In addition, the cost of these tests is high and their experimental setup is challenging (Iskander 2010). With the advent of digital optical equipment and imaging science, transparent materials have been recently used to replace opaque soil particles in experimental tests. With the help of the particle image velocimetry (PIV) technique, transparent soil has been employed to study: soil displacements under strip footings (Liu 2009; Liu and Iskander 2010); ground response due to tunnelling (Ahmed and Iskander 2012); and measure soil movements around pile foundations (Liu et al. 2010). Previous research has shown that transparent soil and PIV are able to investigate soil displacement problems in geotechnical engineering.

In this paper, transparent soil, made of fused quartz and a matched refractive index pore fluid, was used to help study the performance of 1:13 scale modules of the 4-sided, 8- and 12-tonne, Broons BH-1300 and BH-1300 HD impact rollers. The behaviour of the roller module is evaluated from four aspects: (i) the soil movement relative to the module motion; (ii) optimal operating speed; (iii) optimum number of rolling passes; and (iv) settlement of the ground surface. To assist in visualising the internal displacement of the transparent soil, a small proportion of the fused quartz particles were painted black to form a one-particle thick layer of black particles in the transparent soil mass. This one-particle thick layer of coloured fused quartz was located along the centreline of the roller traverse lane, and with the transparent particles, formed a speckled pattern. The displacement of the pattern subjected to impact roller was captured by a conventional charge-coupled device (CCD) camera. Images were then analysed by the PIV technique

to investigate the displacement fields. Results obtained from the PIV technique were used to understand the mechanics and effectiveness of the roller module.

2.2 Experimental Setup

This section presents the experimental setup and discusses the materials used, sample preparation, the PIV system, the experimental procedure and the calibration tests.

2.2.1 Materials

Transparent soil is a two-phase medium, which contains solid transparent surrogates and a matched refractive index pore fluid. In this study, fused quartz (Figure 2.1a) was chosen as the transparent surrogate. This material is stable, hard and exhibits high transparency. The fused quartz particles were sieved before and after the scale model testing and the reduction in particle size was found to be insignificant in this study. A wide range of grain sizes is available commercially and high purity fused quartz particles are essential to obtain better visibility of the transparent soil. Considering the transparency of the particles and the size of the chamber, in this study, the fused quartz size range is selected to be between 3 and 5 mm, with D_{50} equals to 3.84 mm. (This is treated in greater detail in the following section.) The particle size distribution curve of the fused quartz particles is shown in Figure 2.1b. Based on the Unified Soil Classification System, fused quartz is classified as a poorly-graded fine gravel (GP). The refractive index (RI) of fused quartz is 1.458. The matching pore fluid used in this paper was sodium-thiosulfate treated sodium-iodide (STSI) solution, which was introduced by Carvalho et al. (2015). At 22°C, the RI of sodium iodide and water are 1.77 and 1.33, respectively. The mixed solution, with the proportion of 105 g of sodium iodide per 100 ml water, has an RI value of 1.458 at 22°C. The maximum and minimum void ratios of the fused quartz are 0.947 and 0.574, respectively. Figure 2.2 demonstrates the clarity of text printed on a sheet of white paper

viewed behind a 60 mm thickness of fused quartz (Figure 2.2a) and STSI saturated fused quartz (Figure 2.2b). It can be seen that after the addition of STSI solution, the transparency of the fused quartz increases dramatically.

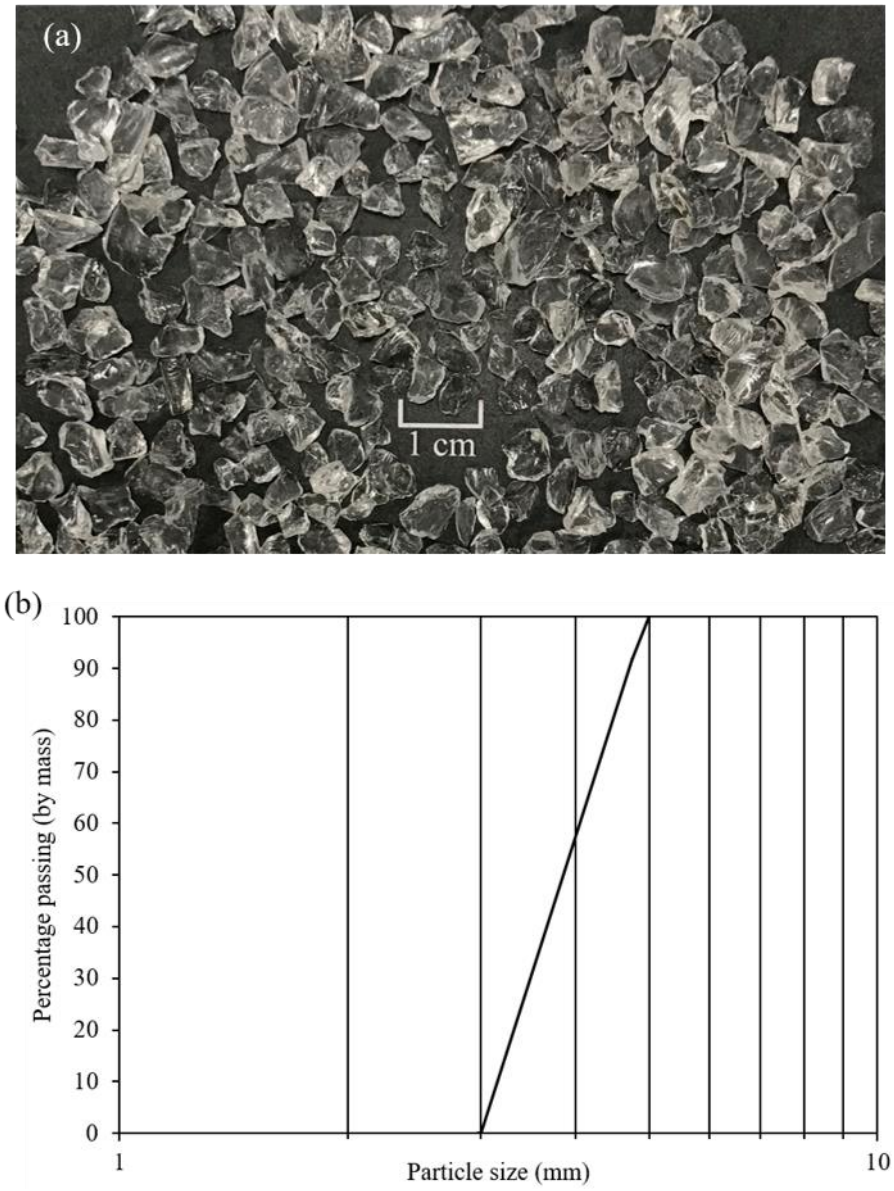

Figure 2.1: (a) Fused quartz samples, (b) particle size distribution curve.

Figure 2.2: Transparent soil with text viewed from behind a 60 mm thickness of fused quartz with: (a) no pore fluid, (b) STSI pore fluid.

2.2.2 Sample preparation

Fused quartz was washed using distilled water to remove any impurities and subsequently dried in the oven. As the RI of the pore fluid varies with temperature, the STSI solution was prepared in the laboratory such that the temperature was maintained at approximately 22°C. The RI of STSI pore fluid was measured after preparation by using a handheld refractometer. A small proportion of fused quartz particles were painted matte black to prevent light transmission. The dyed particles were randomly and manually scattered between two thick layers of transparent soil to form a speckled pattern with unique texture.

Particle displacements resulted in the changes of speckled pattern during the roller module travels. The movement of speckled pattern was captured by a CCD camera and then images were analysed by the PIV technique.

The transparent soil sample was prepared in an acrylic rectangular chamber, with dimensions of 300 × 280 × 250 mm (length × width × height). The chamber was constructed from 12 mm thick acrylic sheets with two detachable panels at its front and top sides to facilitate the placement of a thin layer of black-dyed fused quartz particles in the centre of the transparent soil sample (Figure 2.3a). The front panel was removed and the transparent particles were carefully placed in the chamber, first by tipping the chamber on its side (Figure 2.3b). The STSI solution was poured into the box, prior to pluviating the particles to minimise the formation of air bubbles. In order to achieve consistent density, the fused quartz particles were pluviated in successive layers from the same approximate height of 50 mm, until half of the chamber was filled (i.e. 140 mm). The surface of the transparent soil sample was then carefully levelled. Black-dyed particles were subsequently placed to generate a distributed speckled pattern. The remaining half of the chamber was then filled with fused quartz particles in the same manner as described above. The front panel was then replaced and the chamber was tipped back into its normal orientation (from Figure 2.3b to Figure 2.3a). The top panel was removed in readiness for testing. Prior to testing, the transparent soil surface was carefully levelled. The initial void ratio of the fused quartz was 0.728, which yielded a relative density of 58.7%.

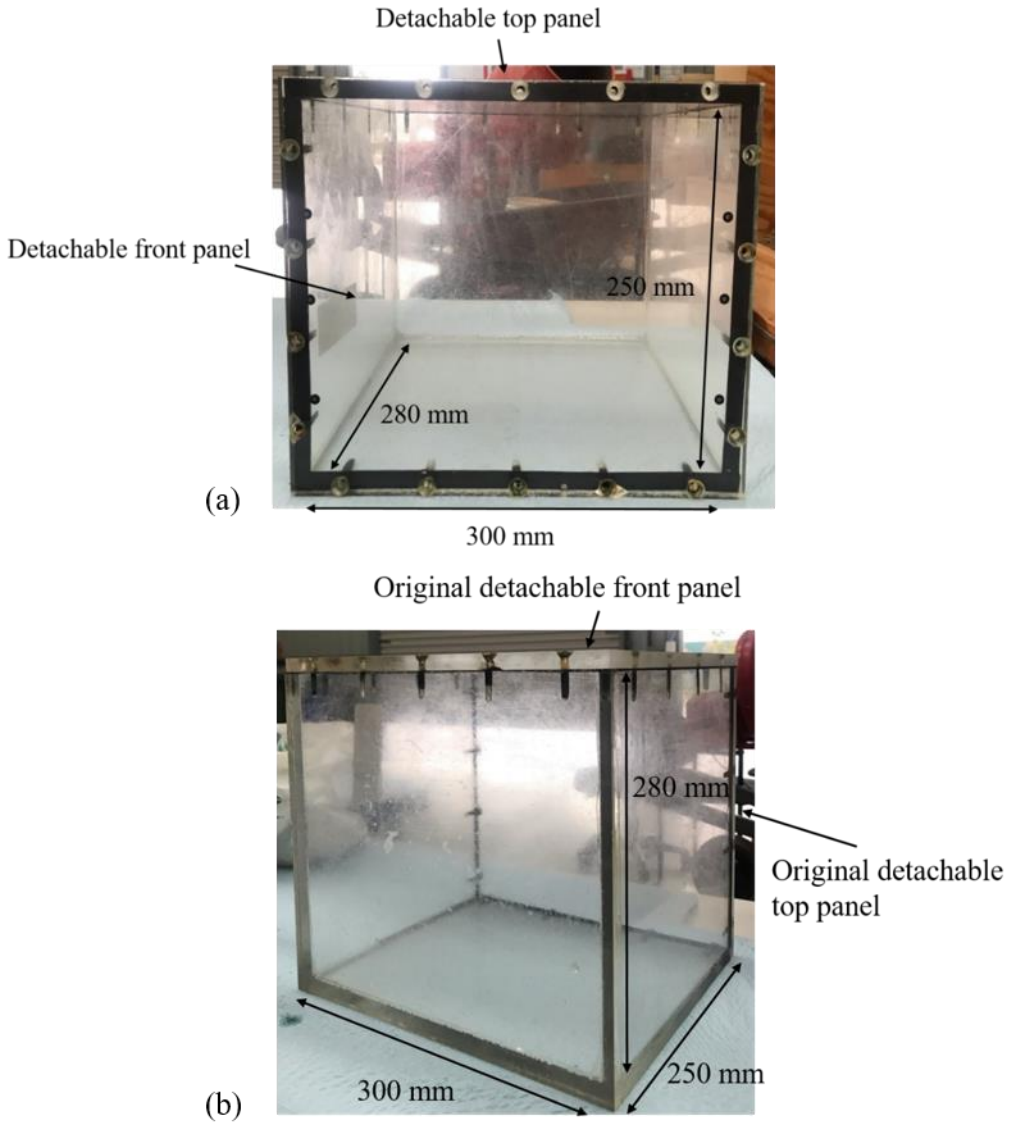

Figure 2.3: Acrylic chamber placed: (a) in its testing orientation, and (b) on its side to facilitate the placement of the transparent surrogates.

In practice, dynamic compaction, as well as RDC, is best performed on soils with moisture contents at or below the optimum moisture content (Scott et al. 2012). However, in the present study, since the fused quartz is required to be fully saturated in order to achieve sample transparency, optimum moisture content is irrelevant. The application of dynamic compaction on saturated soils is presently as a controversial topic. Some researchers, such as Pak et al. (2005) and Bo et al. (2009), have commented that the compactive effort induced by dynamic compaction resulted in an increase in porewater pressure. The high porewater pressure either reduced the effectiveness of dynamic

compaction in the impervious saturated soils (e.g. clayey soils with a plasticity index larger than 8) or caused liquefaction in sandy soils. However, Pak et al. (2005) stated that dynamic compaction is effective on saturated soils if the soil is free draining, since the porewater has low compressibility when compared with the soil skeleton. In the present study, drainage occurs at the top surface to facilitate soil compaction. More importantly however, and whilst not entirely ideal, in the present study the soil is saturated in order to facilitate soil transparency. As the paper demonstrates, the transparent nature of the soil provides great insight into RDC-induced ground improvement.

2.2.3 The PIV system

When the roller module traverses and compacts the simulated ground surface, the particles displace and, given the transparent nature of soil, along with the central plane of speckled particles, displacements can be observed and measured using the PIV technique. Images before and throughout the roller module process were captured using a conventional CCD camera. In this paper, a 2.3 Megapixel, monochrome Point Grey CCD camera was used. It is able to capture up to 163 frames per second at 1 920 × 1 200 pixel resolution. As the centreline of the traverse of the module is coincident with the centreline of the chamber, and hence the speckle-patterned plane, the displacement of the black-dyed particles is assumed to be a plane-strain problem, and therefore only a single camera was needed and used. The lens adopted in this study was a Schneider – Kreuznach Xenoplan f/1.4 with a 17 mm focal length. The camera was placed in front of the chamber and the distance between the lens and the chamber was maintained at 800 mm for all tests. *VicSnap* is a commercial computer program, which connects the camera to the computer for image acquisition purposes. This software also provides a preview of the captured images for users and it allows users to adjust the imaging parameters remotely, such as

the area of interest, resolution, exposure times and frame rate. In this study, all images were captured with full resolution (1 920 × 1 200 pixels) at 120 frames per second.

PIV is an image-based technique which was first applied in fluid mechanics by Adrian (1991) to obtain velocity changes. The texture of an image is tracked by the PIV technique through a series of images to obtain displacement fields. In this study, PIV analysis was conducted using a free *MATLAB* module *GeoPIV_RG* developed by Stanier et al. (2015). *GeoPIV_RG* adopts the first-order subset shape function to gather sub-pixel resolution displacements, which increases precision and reduces random walk errors (Stanier et al. 2015).

2.2.4 Experimental procedure

A bespoke test facility was developed to facilitate the RDC-related research program. The testing equipment incorporates a stadium-shaped track (Figure 2.4a). A variable-speed electric motor, pulls a 1:13 scale model of the 4-sided impact roller (Figure 2.4b) around the track and across the transparent soil filled chamber that is housed within a timber frame (Figure 2.4c). The 1:13 scale ratio was selected as an optimal compromise between the overall dimensions and weights of the test rig, operation accuracy, employed soil particle size and fabrication costs. Several tests were performed by Chung et al. (2017) using this test facility with a Sandy Gravel soil with maximum particle sizes of 10 mm. The results from the 1:13 scale model were in good agreement with field test measurements obtained by Scott et al. (2016) using the full-size impact roller over the same soil and no particle size effects were detected, which suggests the 1:13 scale model is a reliable surrogate for the full-size RDC module.

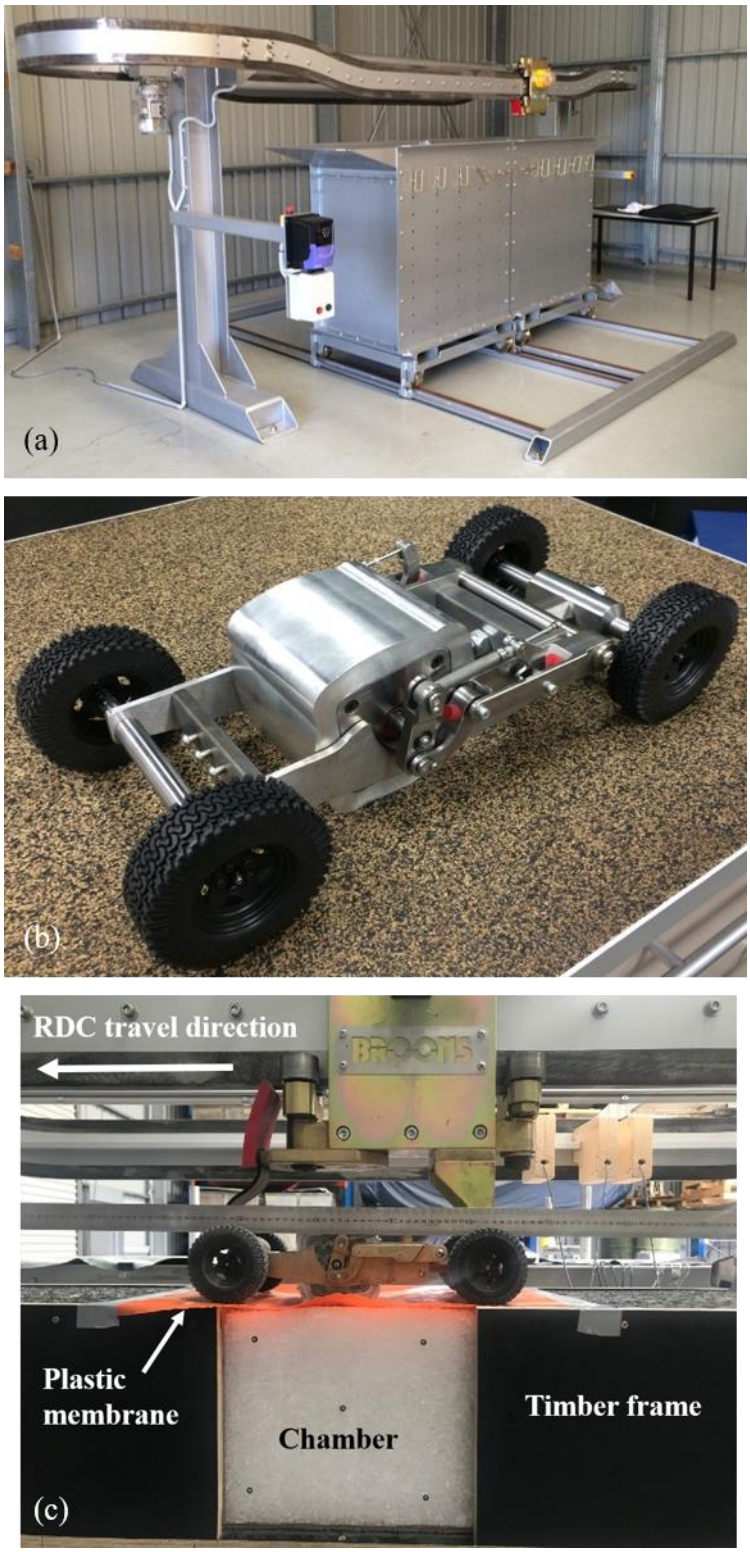

Figure 2.4: RDC experimental facility: (a) test rig, (b) 1:13 scale model of 4-sided impact roller, and (c) transparent soil setup.

The scale model was designed and fabricated so that its density is identical to the full-size model. The scaling laws developed by Altaee and Fellenius (1994) [Equations (2.1)–(2.6)], for scale model testing under a normal gravity (1*g*) situation, were used to correlate

the properties of the scale model with those of the full-size model. In this study, the geometric scale ratio (n) is 1/13.

$$\frac{L_m}{L_p} = n \tag{2.1}$$

$$\frac{V_m}{V_p} = n^3 \tag{2.2}$$

$$\frac{M_m}{M_p} = n^3 \tag{2.3}$$

$$\frac{D_m}{D_p} = n \tag{2.4}$$

$$\frac{T_m}{T_p} = 1 \tag{2.5}$$

$$\frac{S_m}{S_p} = n \tag{2.6}$$

where L represents the dimensions of the module, V and M are the volume and mass, respectively, of the roller module, D is the displacement of the module, T is the operating time and S is the operating speed, n is the geometric scale ratio, and the subscripts m and p denote the scale model and prototype (i.e. the full-size module), respectively.

Therefore, according to Equations (2.1)–(2.3), a series of tests were developed using two different weights of modules (3.64 and 5.46 kg), with identical dimensions of 115 × 115 × 100 mm (height × length × width). These two models are 1:13 scaled replicas of the 4-sided, 8- and 12-tonne impact rollers (Broons BH-1300 and BH-1300 HD), respectively (Jaksa et al. 2019). In practice, an approximately 200 mm thick, crushed rock working base is typically placed at the ground surface of relatively loose, dry sandy soils to ensure the effective rotation and energy transfer of the roller, and to prevent it from bogging (Avalle and Carter 2005). In this study, a 0.2 mm thick, polyethylene membrane was placed on the upper surface of the transparent soil to simulate the working base used in field to facilitate appropriate rotation of the module (Figure 2.4c). This membrane is

selected from various materials since it is thin enough to effectively transfer the energy from the module to the soil without compromising the accuracy of the tests. The membrane was loosely placed to allow pore water dissipation and compaction at the ground surface after several module passes.

As mentioned above, two 1:13 scale models of the 8- and 12-tonne impact rollers were examined to study the relationship between the weight of the module and soil displacements. In addition, the number of rolling passes and the operating speed of both modules were varied to assess their effects on soil displacements. Operating speeds between 10 and 12 km/h are the most commonly adopted speeds in practical applications. However, the efficacy of RDC travels above 12 km/h has not been tested extensively in the field and, hence, the optimum speed for this type of roller is yet to be determined. Since scale models are used in this study, prototype operating speeds were converted to scale model speeds, based on Equations (2.4) to (2.6). Four different operating speeds are examined: 214, 256, 299 and 342 mm/s, corresponding to the prototype speeds of 10, 12, 14 and 16 km/h, respectively. Therefore, in total, eight tests were conducted for the 3.64 and 5.46 kg scale models at four different speeds, with each test being carried out up to 40 passes.

2.2.5 Calibration tests

The quality of the PIV results depends significantly on the development of a satisfactory speckled pattern. Too many black-dyed particles can cause poor illumination and, hence, results in dark images. On the other hand, if too few black-dyed particles are used, the displacement information provided by the PIV results will be inadequate. Several calibration tests were performed to examine the optimum density (which is defined as the mass of coloured fused quartz particles divided by the area of the plane of interest) of the

black-dyed fused quartz particles to form a speckled pattern within the plane of interest. The mean correlation coefficient obtained from the *GeoPIV_RG* software was used to quantify the optimum density of dyed particles as it reveals the correlation between images. As a result, a density of 1.5×10^{-3} g/mm^2 of black particles was found to be optimal as it yielded the highest correlation coefficient value. Figure 2.5 shows the speckled pattern formed by the optimal density of black particles viewed behind a 140 mm thickness of transparent soil. In the scale model test, the cross-sectional area of the plane of interest is 300 × 250 mm. Therefore, 112.5 g of dyed particles were used to form the speckled pattern in the tests. In addition, the optimum subset size was also investigated by repeating multiple PIV analyses with different subset sizes for each dyed particle density. Based on the highest mean correlation coefficient value, subsets of $6.52D_{50}$ (~ 25 mm) were selected to be used in the following PIV analyses. Each subset has a centroid spacing of 12.5 mm to preserve the accuracy of the PIV results. The scale model tests were conducted in a relatively dark room, and the walls of the timber frame were painted black with a matte finish to minimise light reflection. To assess the efficacy of the apparatus and PIV system, the speckled pattern was captured over a time period where the test rig was non-operational, and no movement was obtained from the PIV results, which provided confidence in the setup and indicated that light reflection did not affect the test results.

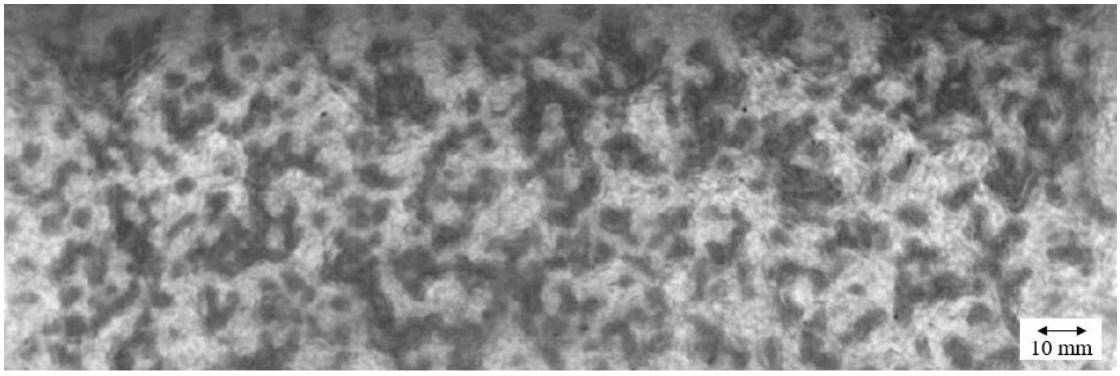

Figure 2.5: An example of the speckled pattern viewed behind a 140 mm thickness of transparent soil.

2.3 Results and Discussion

2.3.1 Soil displacement relative to module motion

Figure 2.6 presents the PIV results of successive images obtained from the first pass with the 3.64 kg module. A red marker is placed at one corner of the module to facilitate the analysis of the motion of the module. The operating speed of the 3.64 kg module is 256 mm/s which, at the 1:13 scale, corresponds to a velocity of 12 km/h of the 8-tonne prototype. Since the time interval in Figure 2.6 is 0.23 s, the horizontal displacement of the module is approximately 59 mm in 0.23 s. The angular velocity is approximately 3.7 rad/s, therefore, the module rotates around its centre by 48.8° during the 0.23 s time period. The vectors in Figure 2.6 have been scaled up by a factor of eight to enhance the visualisation of the soil displacements. In general, it can be seen that, as the module travels from right to left, the soil body displaces from right to left and from top to bottom, as one would expect. Figure 2.6a exhibits the displacement vectors prior to the module traversing the soil. Figure 2.6b shows the position of the module, illustrated at the correct scale with respect to the chamber, after it leaves the timber frame and contacts the transparent soil. The module subsequently traverses the upper surface of the soil (Figure 2.6c, d, e and f), which causes the particles beneath the module to displace downwards and to the left, i.e. in the same direction as the module's motion. The displacement vectors in Figure 2.6c indicate that the soil particles are pushed in the direction of the module. The lower corner of the module in Figure 2.6d penetrates into soil, which causes the soil particles immediately beneath the ground surface to settle. In Figure 2.6e, the soil behind the module displaces downwards and to the right, and the soil particles in front of the module are pushed to the left. In Figure 2.6f, again, the soil in front of the module is pushed and displaces in the lateral direction of the module's motion. Figure 2.6g shows the cumulative displacement vectors after the first pass of the 3.64 kg module.

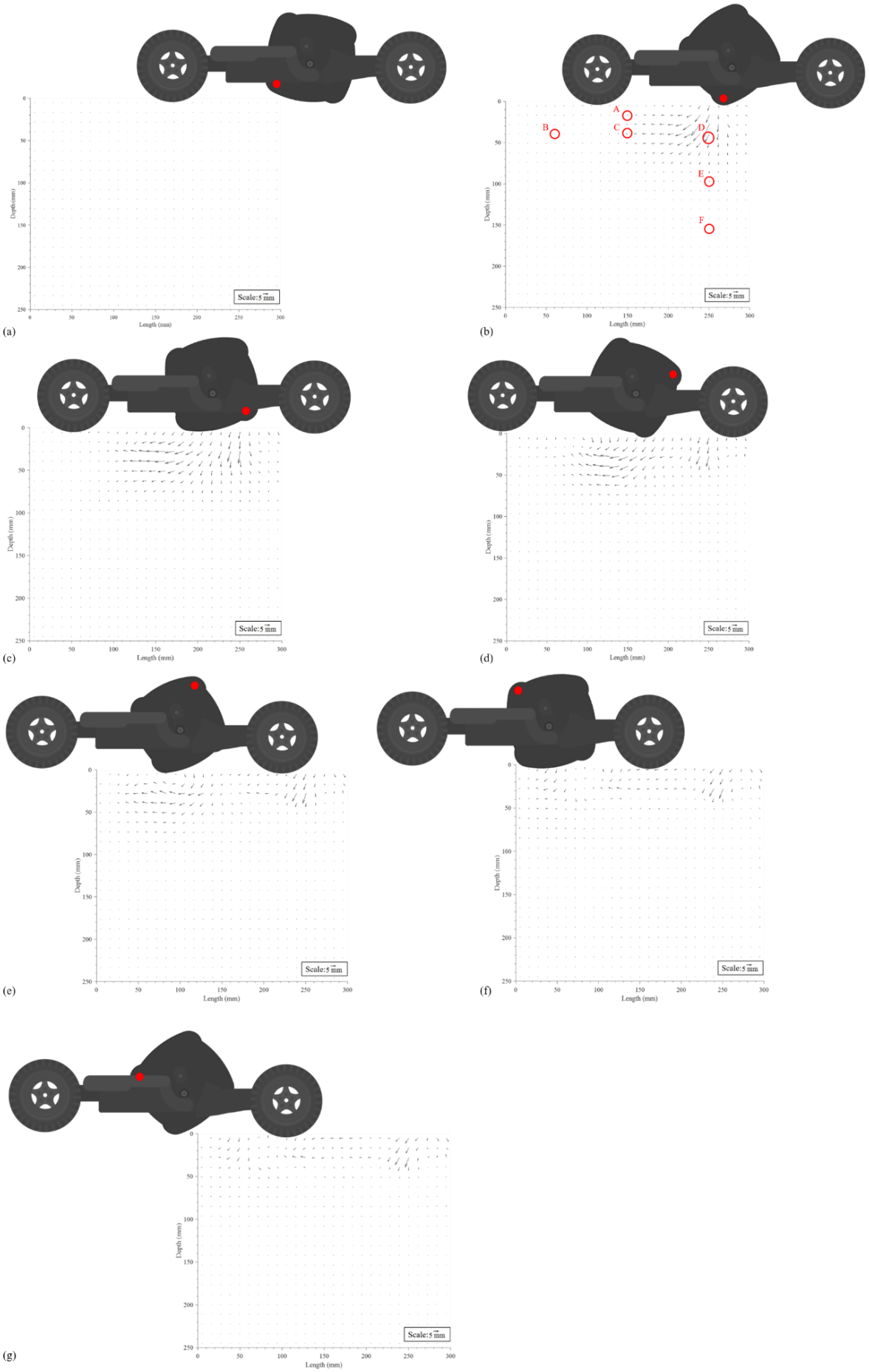

Figure 2.6: Successive images of the module motion: (a) t=0 s, (b) t=0.23 s, (c) t=0.46 s, (d) t=0.69 s, (e) t=0.92 s, (f) t=1.15 s, (g) t=1.38 s.

Figure 2.7 presents the cumulative horizontal and vertical displacements of Regions A, B, C, D, E and F (as shown in Figure 2.6b) with respect to the time and motion of the 3.64 kg module in Figure 2.6 for the first pass. In order to maintain consistency with the direction of motion shown in Figure 2.6, the origin of the horizontal (time) axis in Figure 2.7 is located on the right-hand-side of the plot. Positive horizontal displacements imply that the soil moves towards the right and positive vertical displacements refer to soil particles that displace downwards. Regions B, C and D are at the same depth (i.e. 40 mm below the surface) but are respectively located on the left-hand-side, centre and right-hand-side of the chamber. Region A is located at the chamber's centreline, but at a depth of 17 mm, whereas Regions E and F are located at the right-hand side of the chamber at depths of 100 and 160 mm, respectively. In general and as expected, soil located in these regions undergoes compaction, as indicated by the significant displacements downwards and to the left when the roller impacts these areas. When the applied compactive force is removed, i.e. the module travels away from these two regions, the soil is slightly pushed upwards, which is consistent with behaviour observed in the field tests from Scott et al. (2019). They investigated the soil response during a single module impact and reported that the soil displaces downwards and may achieve its maximum vertical displacement due to loading. Then, the vertical displacement may decrease upon unloading.

In terms of the module's influence, as it moves from right to left, we first examine Region D. Between 0 and 0.23 s, it can be seen clearly that, when the module first impacts the soil near the right-hand boundary, the soil at Region D is pushed to the left and downwards. Between 0.23 to 0.92 s, as the module continues to travel to the left, the soil slightly displaces upwards and to the right. After 0.92 s, there is no obvious displacement observed at Region D, when the module has travelled further away from this location. At Region C, from 0 to 0.46 s, the soil is mainly pushed horizontally in the direction of the

module's motion. The soil shows its greatest downward displacements between 0.46 and 0.69 s as the module traverses close to Region C, and then the soil moves upwards and to the right after 0.69 s since the module impacts the soil to the left of Region C. As one would expect, the soil displacements at Region A are similar to those occur at C, since they are both located at the centreline of the chamber. However, the soil at Region A has greater vertical displacements when compared with those at C, given that A is closer to the ground surface. Before 0.46 s, the particles at B displace slightly because of the motion of the module to the right of B, whereas between 0.46 and 0.92 s, the soil displaces upwards and to the left as the module approaches B. After 0.92 s, the soil gradually displaces to the right and downwards as the module continues to travel to the left-hand side of the chamber and then off the transparent soil and onto the timber frame. The values of cumulative displacements at 1.38 s show that, after the first pass of the module, the soil particles at Regions B and C have permanently displaced downwards and to the right, and the soil located at A and D displaced downwards and to the left.

Figure 2.7b shows the cumulative displacements of Regions E and F. It can be seen that the soil displacements at E are similar to those at D, but to a lesser extent, as they are located at the right-hand side of the chamber, with E being at a greater depth. As can be seen, the soil particles at Region F experience no observable displacement during the first pass of the module given their depths below the ground surface.

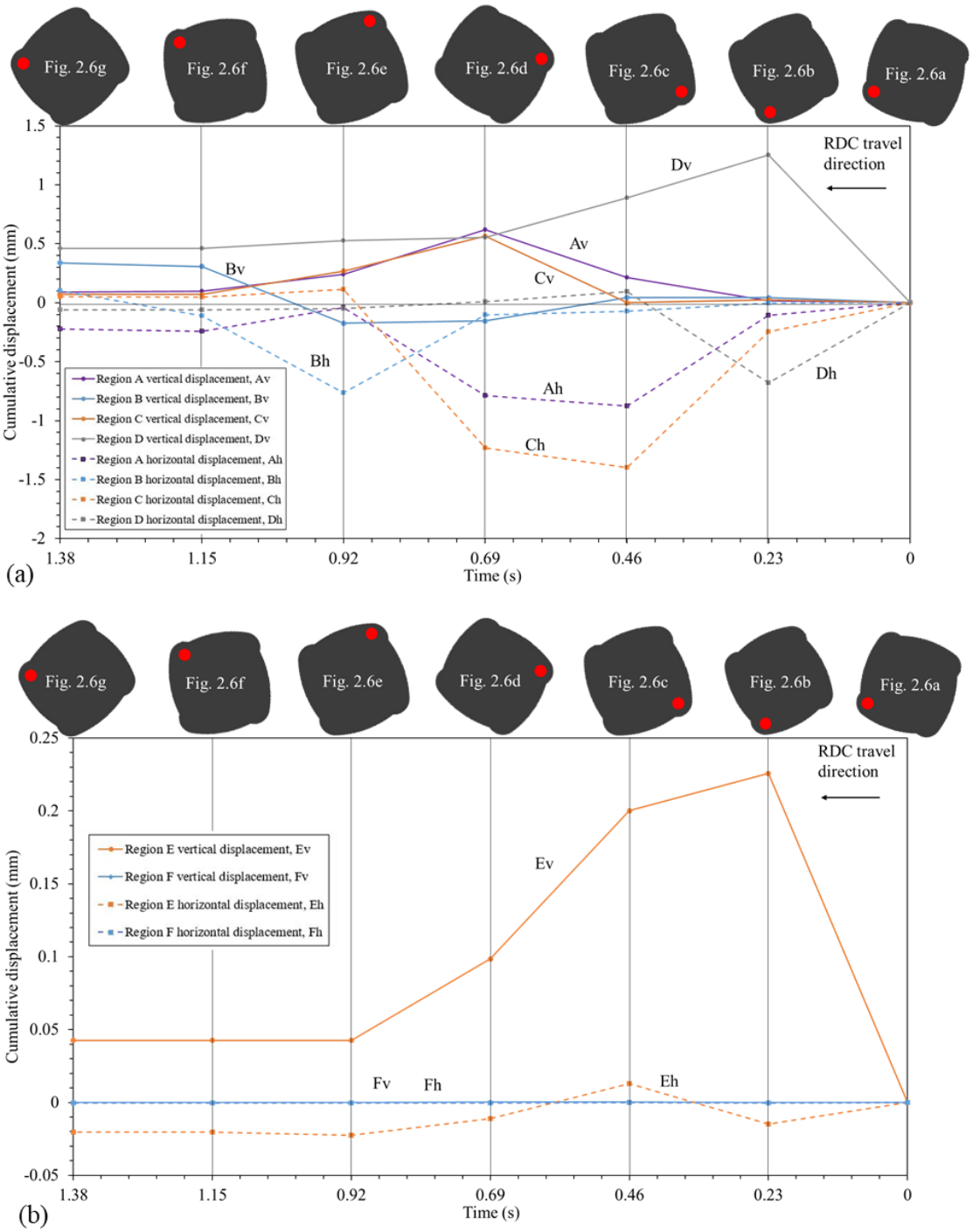

Figure 2.7: Cumulative vertical and horizontal displacements of 6 regions versus time: (a) Regions A, B, C and D, (b) Regions E and F, for the first pass.

To understand better the displacement patterns of the soil as a result of the module, the displacements of these regions are traced by plotting their x and y coordinates with respect to the time and motion of the module in Figure 2.6 during the first pass, which are also known as Eulerian trajectories (Omidvar et al. 2014). Similar to Figure 2.6, the

incremental displacements in Figure 2.8 have been scaled up by a factor of eight to reveal the movement of each region. Figures 2.8a-e show the displacements of Regions A, B, C, D and E (refer to Figure 2.6b), respectively. Note, in order to observe clearly the particle trajectories, the scales of both axes in each of these figures are different. Since Figure 2.7b shows that Region F has no obvious vertical or horizontal displacement during the first pass of the module, the trajectories of Region F are not included in Figure 2.8. The red arrows point from the initial position towards the final position of the region (plastic displacements) and the black arrows indicate the movement of the region at different times (elastic displacements). The relative motion of the module is indicated in Figures 2.6 and 2.7.

It can be seen clearly that all these five regions displace significantly during the first pass of the module. When the module travels close to these regions, the soil in these regions moves to the left and downwards. As the module traverses away from these regions, the particles are pushed to the right and move upwards. If the soil is located near the ground surface (Region A) or is directly impacted by the roller (Regions D and E), the soil will exhibit greater horizontal displacements to the left than to the right. Therefore, the plastic displacements within these regions (shown by the red arrows) indicate that the soil in these regions displaces to the left after the first pass. The soil particles at B and C exhibit slightly greater displacements to the right than to the left during the first module pass.

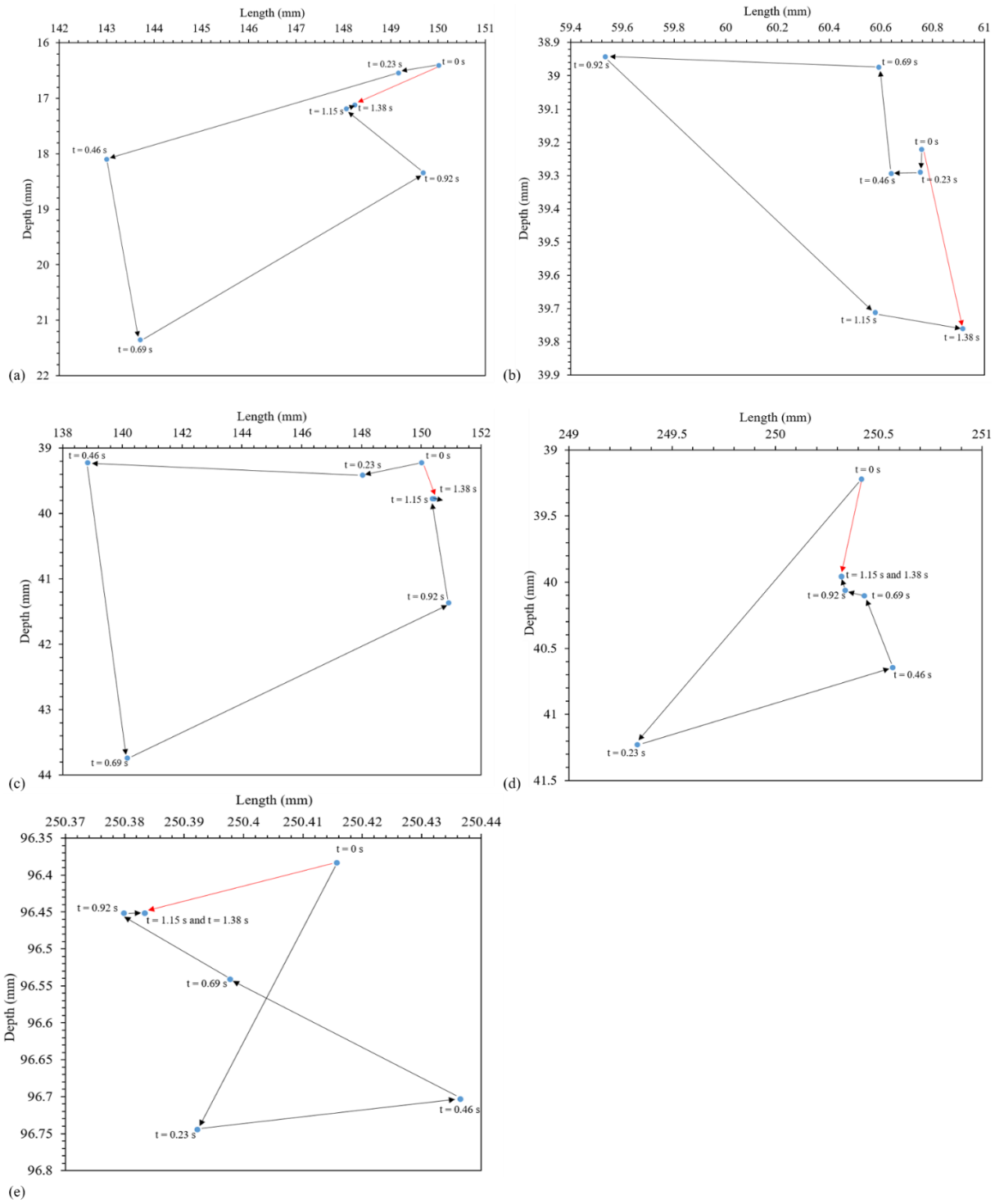

Figure 2.8: Trajectories of five regions during the first pass of the 3.64 kg module travelling at a speed of 256 mm/s: (a) Region A, (b) Region B, (c) Region C, (d) Region D, (e) Region E.

2.3.2 Module speed

The performance of the 3.64 and 5.46 kg modules, travelling at speeds of 214, 256, 299 and 342 mm/s, is examined using the displacements obtained from *GeoPIV_RG*. It can be seen clearly from Figure 2.6c that the face of the module has rotated about its corner

and compacted the soil, which is defined as the impact of the module. As the scale model impacts the transparent soil in the chamber, three or four times each pass, the front face of the chamber is divided into three zones, as shown in Figure 2.9. It is worth mentioning that the roller may impact the soil in the same or a different location as the previous pass, since the roller is free to move along the track. However, in all tests, the first impact always occurs in Zone C (e.g. Figure 2.6b), and the second and third impacts occur in Zones B and A (e.g. Figures 2.6c and 2.6e), respectively. The fourth impact occurs near the left edge of Zone A (e.g. Figure 2.6f) or on the right edge of timber frame, depending on the speed of the module. Displacements induced by the module at Zones A, B and C are compared for both the 3.64 and 5.46 kg modules travelling at four different speeds to observe the repeatability or variation in the displacement patterns. Since the soil movements in Zones A and C are constrained by the edges of the chamber, the soil displacements from Zone B are examined more extensively to investigate the behaviour of the module.

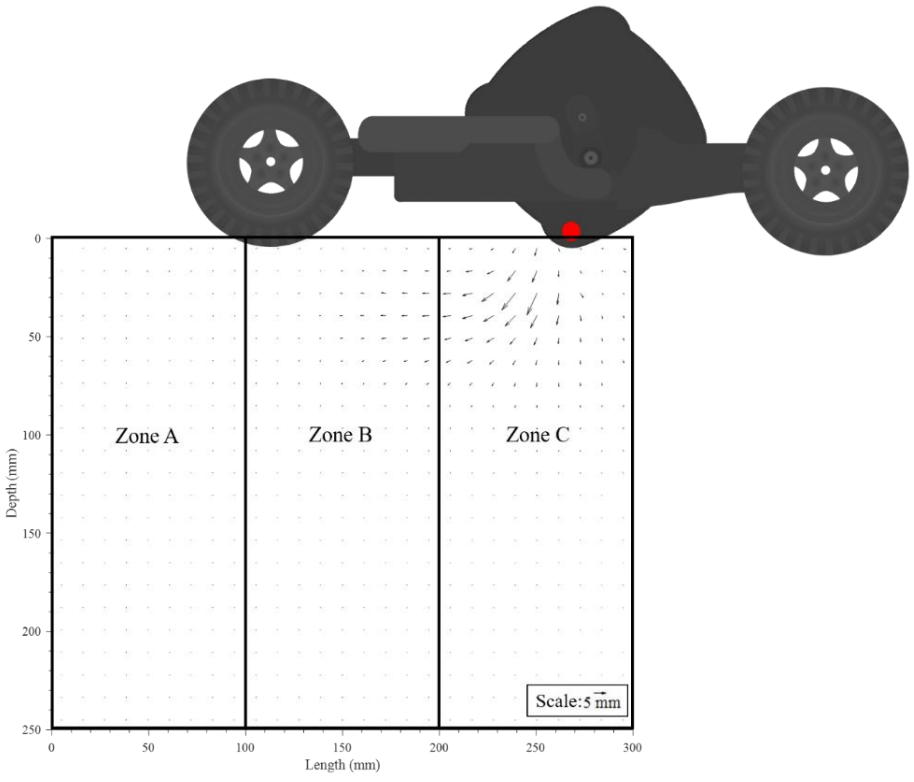

Figure 2.9: Three subdivided zones of the displacement field.

Cumulative displacement vectors and vertical displacement contours of soil subjected to the 3.64 and 5.46 kg modules, travelling at four different speeds after 40 passes, are shown respectively in Figures 2.10 and 2.11. In the vertical displacement contour plots, a positive value again suggests that the soil displaces downwards. Because of the use of the polyethylene membrane, the brightness of the images is compromised in some circumstances. This is demonstrated in Figure 2.10d by the loss of vectors near the ground surface. The PIV results illustrate the variable nature of soil displacements near the ground surface. This is because the soil near the ground surface is disturbed and becomes undulating due to the geometry of the module. In general, it can be seen clearly that the displacement vectors and contours are significantly influenced by the operating speed of the module. As the operating speed increases, greater horizontal and vertical displacements are manifested. It is noted that the soil located above a depth of approximately 40 mm displaces downwards and to the left, whereas the soil below this depth displaces downwards and to the right. This phenomenon is similar to the cumulative displacement vectors obtained after the first pass of the 3.64 kg module (Figure 2.6g), for the same reasons as explained above, and is more pronounced after 40 passes. In addition, it can be seen from the displacement contour plots that the vertical displacements induced by the module decrease with depth as the compactive energy dissipates with depth. As mentioned above, a medium-dense fused quartz sample, with larger particles (D_{50} = 3.84 mm), is used in this study, which results in the soil particles being less able to displace, therefore, the compactive effects are limited to relatively shallow soil depths.

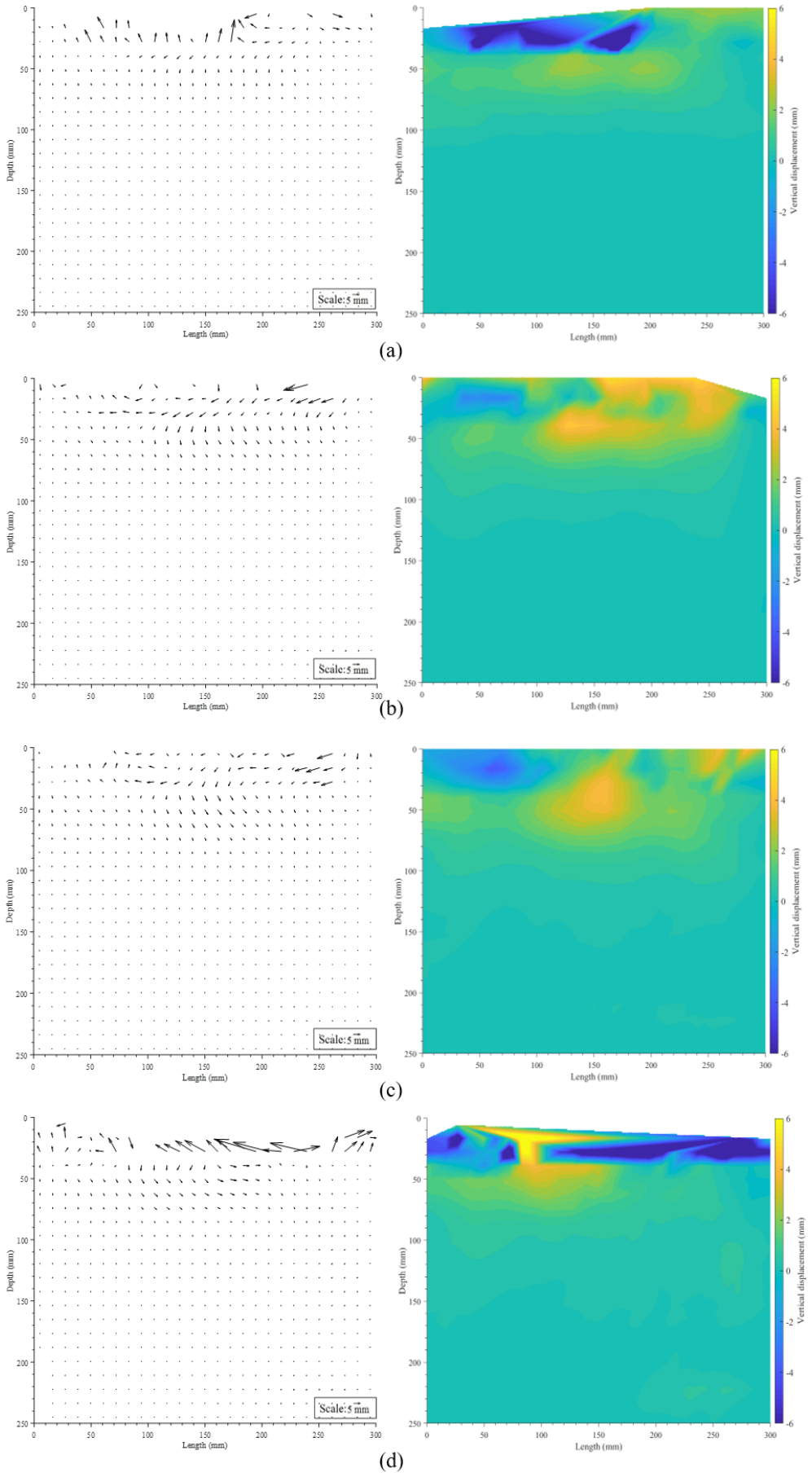

Figure 2.10: Cumulative displacement vectors (left) and vertical displacement contours (right) of 3.64 kg module after 40 passes at speeds of: (a) 214 mm/s, (b) 256 mm/s, (c) 299 mm/s, and (d) 342 mm/s.

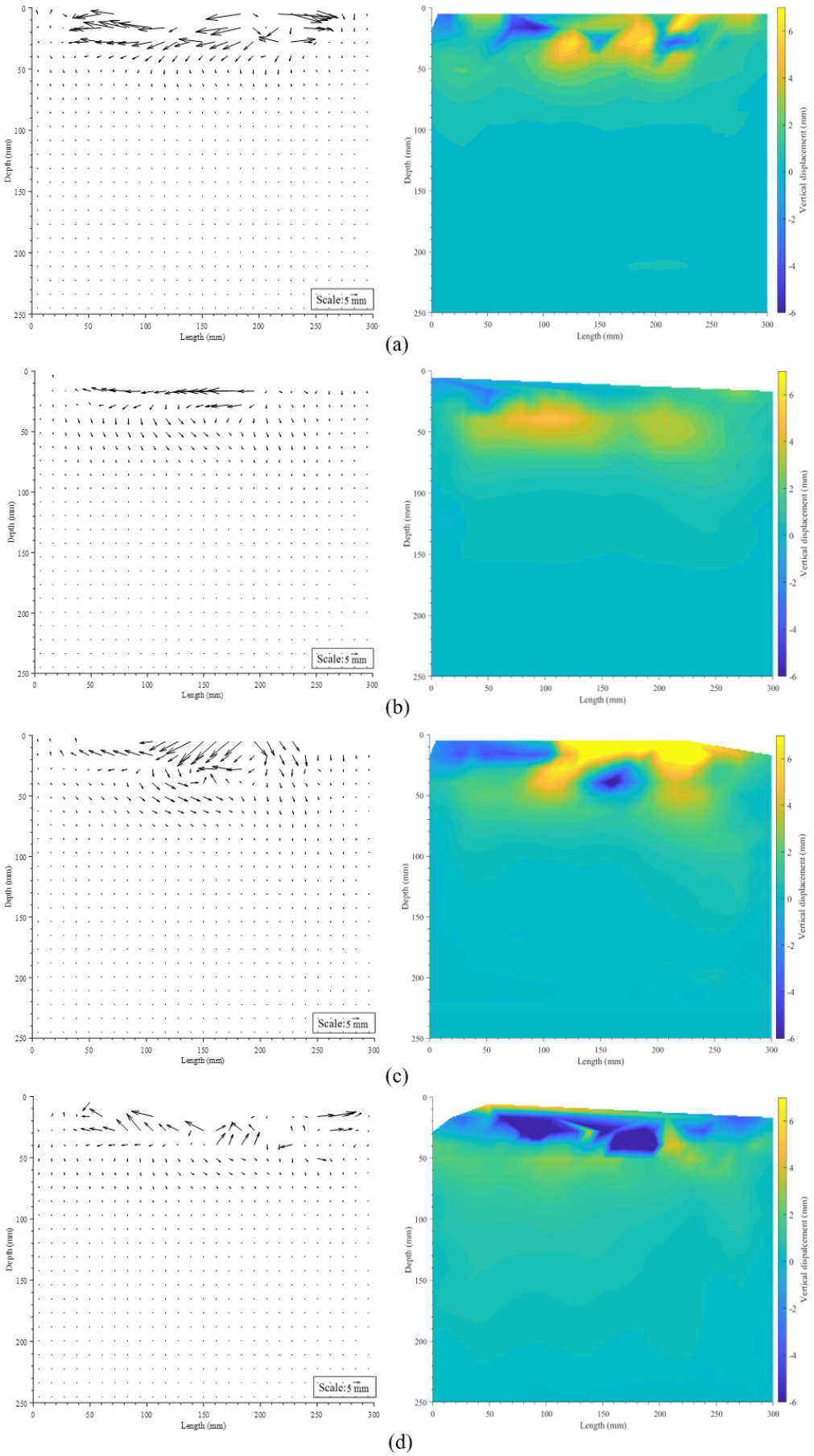

Figure 2.11: Cumulative displacement vectors (left) and vertical displacement contours (right) of 5.46 kg module after 40 passes at speeds of: (a) 214 mm/s, (b) 256 mm/s, (c) 299 mm/s, and (d) 342 mm/s.

In order to assess the behaviour of RDC, as well as other compaction methods, researchers and practitioners often refer to the improvement depth (Kuo et al. 2013; Jafarzadeh 2006; Feng et al. 2015). Improvement depth is defined as the depth over which the soil's density and shear strength are improved by the applied compaction forces (Kuo et al. 2013; Jafarzadeh 2006). In this study, since the PIV technique is adopted, the improvement depth is quantified by the depth at which the soil undergoes vertical displacements less than 0.1 mm due to the module. It is worth noting that the improvement depth is used merely as a surrogate to quantify the optimum speed for both the 3.64 and 5.46 kg modules. A plastic vertical displacement of 0.1 mm is adopted to represent the minimum quantifiable soil displacement considering the precision constraints of the adopted *GeoPIV_RG* algorithm (Stanier et al. 2015). From Table 2.1, it can be seen that, for the 3.64 kg scale model, as the operating speed increases, the improvement depth also increases. When the operating speed of the 3.64 kg module rises to 342 mm/s, the improvement depth shows no further increase. In addition, as shown by the displacement vectors plots (Figure 2.10), when the 3.64 kg module travels at a speed of 214 mm/s, soil particles near the ground surface displace upwards and to the left due to sliding of the module. This phenomenon is consistent with observations reported by Avalle et al. (2009). They stated that the low operating speed may result in insufficient momentum to maintain module rotation without sliding. As the speed of module increases, the soil particles beneath the ground surface are compacted and move downwards. The soil displacements increase as the operating speed rises. When the module travels at an operating speed of 342 mm/s, the soil near the ground surface is pushed upwards and to the left significantly due to the corners of the module. As reported by Clifford (1980), Avalle et al. (2009) and Scott et al. (2020), the module tends to bounce along the ground from corner to corner at higher operating speeds, which results in the soil near the ground surface being ploughed by the corner of the module. In addition, soil displacements at greater depths decrease

when compared with the displacements induced by the module travelling at 299 mm/s. Soil displacements in Zones A, B and C both increase when the operating speed grows from 214 to 299 mm/s. When the module travels at 342 mm/s, soil displacements in Zones A, B and C reduce slightly.

Table 2.1: Improvement depths of 3.64 and 5.46 kg modules at speeds of 214, 256, 299 and 342 mm/s.

Module weight (kg)	Operating speed (mm/s)	Improvement depth (mm)
3.64	214	130
	256	165
	299	230
	342	230
5.46	214	210
	256	220
	299	240
	342	230

As mentioned above, the soil in Zone B has minimal influence from boundary effects, the average vertical displacements at different depths below the ground from this zone after 40 passes are plotted in Figure 2.12 to assess the effects of operating speeds. The displacements of soil above 50 mm depth are not included in Figure 2.12 since the soil above this depth is disturbed by the module, and results in somewhat random soil particle displacements. The dashed lines in Figure 2.12 represent 0.1 mm soil displacement and assist in identifying the improvement depth shown in Table 2.1. In Figure 2.12a, it can be seen that the average vertical displacements at different depths increase as the operating speed rises from 214 to 299 mm/s. When the 3.64 kg module is operated at 342 mm/s, the vertical displacements reduce significantly and the displacement at around 50 mm depth is even less than that which was measured at 214 mm/s. This is consistent with the findings from Rajarathnam et al. (2016). They stated that soil displacements increase as the operating speed rises until the module reaches its optimal velocity. Once the operating

speed is greater than the optimal speed, soil displacements decrease. As a consequence, it can be concluded that, for the 3.64 kg module, an operating speed of approximately 299 mm/s is suggested as the optimal speed, from a compaction perspective.

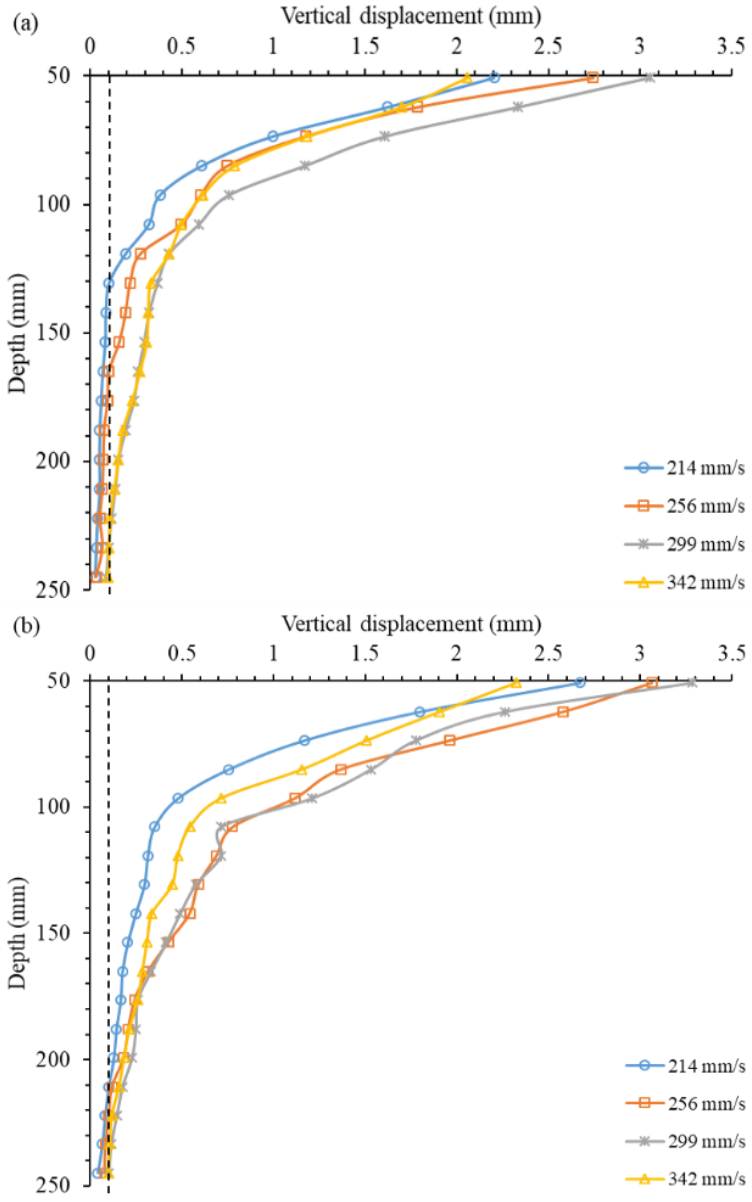

Figure 2.12: Average vertical displacements at different depths within Zone B after 40 passes: (a) 3.64 kg scale module, (b) 5.46 kg scale module.

Similar conclusions are obtained from the 5.46 kg module tests. As shown in Table 2.1, when the 5.46 kg scale model travels at a speed of 214 mm/s, the improvement depth is around 210 mm. The improvement depth increases as the operating speed grows. The results obtained from the 342 mm/s test show a decreased improvement depth. As seen

in Figure 2.11, with a 214 mm/s operating speed, the soil particles located above 50 mm depth move upwards and they are pushed in the direction of travel of the impact roller. When the roller operates at a 342 mm/s operating speed, the soil particles near the ground surface displace upwards significantly. As shown by the displacement vectors and vertical displacement contour plots, at a 299 mm/s speed, the module significantly compacts the soil located above 70 mm depth, as indicated by the downward displacements. When the module operates at 256 mm/s, the soil near the ground surface is ploughed in the direction of the impact roller, with no obvious vertical movement. The changes of soil displacements in Zones A, B and C for the 5.46 kg module travelling at four different speeds are similar to those observed for the 3.64 kg module. Displacements in Zones A, B and C increase when the speed of the roller rises from 214 to 299 mm/s, and the displacements in these zones decrease as the operating speed increases to 342 mm/s. In Figure 2.12b, the vertical displacements in Zone B increase as the operating speed rises from 214 to 256 mm/s. The 299 mm/s operating speed exhibits similar displacements as at 256 mm/s, but with a greater displacement at around 50 mm depth. The vertical displacements decrease when the operating speed rises to 342 mm/s. This is again consistent with the findings of Rajarathnam et al. (2016). Soil displacements increase as the operating speed rises to the optimal operating speed. After that, the soil displacements decrease. There are several reasons for this. Firstly, the module skips along the ground about its corners at higher operating speeds, and the compactive energy is delivered by the corners rather than the faces of the module, which result in the soil not being compacted effectively (Clifford 1980; Avalle et al. 2009; Scott et al. 2020). Secondly, the soil particles have insufficient time to rearrange at higher operating speeds, therefore, the soil has diminished plastic displacements (Rajarathnam et al. 2016). As with the 3.64 kg module, the test results indicate that 299 mm/s is the optimal speed for the 5.46 kg module, from a compaction standpoint.

Comparing the displacement fields caused by the 3.64 and 5.46 kg scale modules, the soil near the ground surface is pushed more dramatically in the direction of travel of the roller with respect to the 5.46 kg module. As the operating speed and material properties are identical for both the 3.64 and 5.46 kg modules, the heavier module produces a larger normal force and, hence, a greater friction force. Therefore, the 5.46 kg module causes the soil moves towards the left. In addition, according to the plots of the displacement vectors, the 5.46 kg module induces greater horizontal and vertical soil displacements for each operating speed, as one might expect. This conclusion is further supported by the average vertical displacement results in Figure 2.12. The 5.46 kg module, operated at 214 mm/s, has similar vertical displacements to the 3.64 kg module operating at 256 mm/s, and the soil displacements measured with the 3.64 kg module travelling at 299 mm/s, are smaller than those associated with the 5.46 kg module travelling at 256 mm/s. In general, 5.46 kg module reaches better efficacy as it induces the greater improvement depth and larger soil displacements for each speed.

2.3.3 Optimum number of rolling passes

The optimum number of passes is determined by assessing the averaged vertical incremental displacements at 50 mm depth in Zone B, since the soil at around 50 mm depth experiences the largest displacements, as shown by the vertical displacement contour plots for all eight tests (Figures 2.10 and 2.11). Incremental particle displacements are obtained using the cumulative particle displacement data gathered from Pass n minus those collected from Pass $n-1$. If the average vertical incremental displacement is less than 0.1 mm, it is assumed that no further quantifiable particle displacement occurs, acknowledging the limitations and resolution of the adopted *GeoPIV_RG* algorithm (Stanier et al. 2015).

As shown in Figure 2.13, the most significant soil displacement generally occurs within the first 20 passes for both the 3.64 and 5.46 kg modules. With subsequent passes, the incremental soil displacement gradually decreases. In general, the incremental soil displacement is less than 0.1 mm after 35 passes. There is no obvious ground improvement after 35 passes. Therefore, for both the 3.64 and 5.46 kg modules, the optimum number of passes is around 35 passes, for the circumstances examined in the present paper.

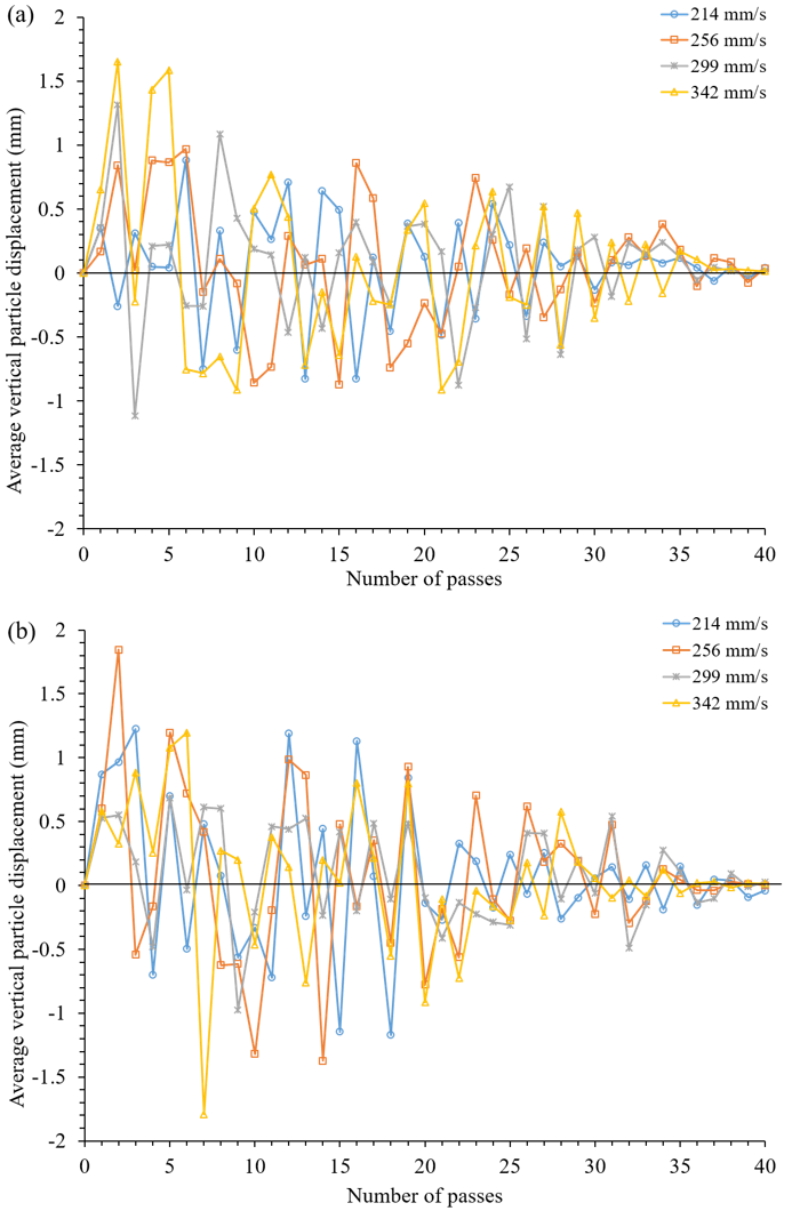

Figure 2.13: Average vertical incremental displacements at 50 mm depth within Zone B: (a) 3.64 kg scale module, (b) 5.46 kg scale module.

2.3.4 Ground surface settlement

Three-dimensional ground surface scanning is applied as an advanced instrumentation technology to provide additional data to help understand the performance of the scale model. Since the module produces non-uniform, undulating ground surface settlements, it is difficult to measure ground settlement efficiently and accurately by manual methods. A high-precision 3D surface scanner (EinScan Pro +) was adopted to provide measurements of the ground surface in high-resolution (distances between points are 0.2 to 3 mm in the point cloud). This technology employs non-laser, white light as the light source to generate a highly accurate ($\pm$0.05 to 0.3 mm) 'point cloud' from the surface of an object in a very efficient manner (550 000 points per second) (Shining 3D 2019). In order to provide reference points for alignment, the process involves the use of adhesive reflective markers which are affixed on the timber frames and the ground surface of the transparent soil. To facilitate accurate measurement of the ground surface by the 3D scanner, some of the pore fluid was removed using a syringe, otherwise, the ground surface was too transparent. After each scan, the pore fluid was carefully reinstated with the syringe. Examples of point clouds generated by the 3D surface scanner over the transparent surrogates are shown in Figures 2.14a and b. The complete acrylic rectangular chamber adopted in the experiments is shown in Figure 2.14. The yellow point cloud (Figure 2.14a) is obtained prior to compaction by the 3.64 kg module and the blue point cloud (Figure 2.14b) is the ground surface scanned after 40 passes of the 3.64 kg module at a speed of 256 mm/s. Figure 2.14c presents the superposition of both the yellow and blue point clouds in order to visualise more effectively the ground settlement induced by the module. In the regions where the yellow obscures the blue, this suggests that the soil in these areas have displaced vertically below the initial ground surface. On the other hand, in the regions where the blue obscures the yellow, this implies that the soil has displaced vertically above the initial ground surface. It can be seen that the yellow (initial)

point cloud is above the blue (after 40 passes) point cloud in the middle and in the right-hand side of the figure, which suggests that the soil in these regions have experienced vertical settlements after 40 passes, especially the soil at the right-hand side of the chamber which shows significant settlements. The reason for this is that the roller module, in travelling from right to left, exits the timber frame and impacts the soil at the right of the chamber. As the roller traverses on the soil, the particles adjacent to the surface are pushed in the direction of the module's travel. Therefore, the soil accumulates to the left of the chamber, and the ground level here, after 40 passes, is higher than that prior to the module. Figure 2.15 shows a photograph of the ground surface of the transparent soil after 40 passes of compaction by the 3.64 kg module travelling at 256 mm/s. It can be seen that the soil at the right-hand side of the chamber has settled (as indicated by the pool of pore fluid at the surface) and the soil particles have accumulated at the left-hand side of the chamber, both of which are consistent with the 3D scanner results. In addition to comparing the ground surface induced by the module visually, the 3D scanner also quantifies the extent of displacement of individual particles within the point cloud subsequent to the module. The displacement of each captured particle is summed and then averaged to obtain the average ground settlement with respect to the number of passes. Figure 2.16 shows the average ground settlement of Zone B after every 10 passes. In general, as one would expect, the 5.46 kg scale model produces larger ground settlements when compared with the 3.64 kg module for each operating speed. The most significant settlements occur within the first 20 passes, for both the 3.64 and 5.46 kg modules travelling at the four different speeds. The soil settlement increases modestly with subsequent passes. After 35 passes, the soil settlement at the ground surface shows minor improvement. This conclusion is in accord with that mentioned in the previous section. It can be observed that the higher operating speeds result in larger ground settlements due to greater kinetic and rotational kinetic energy induced by the module.

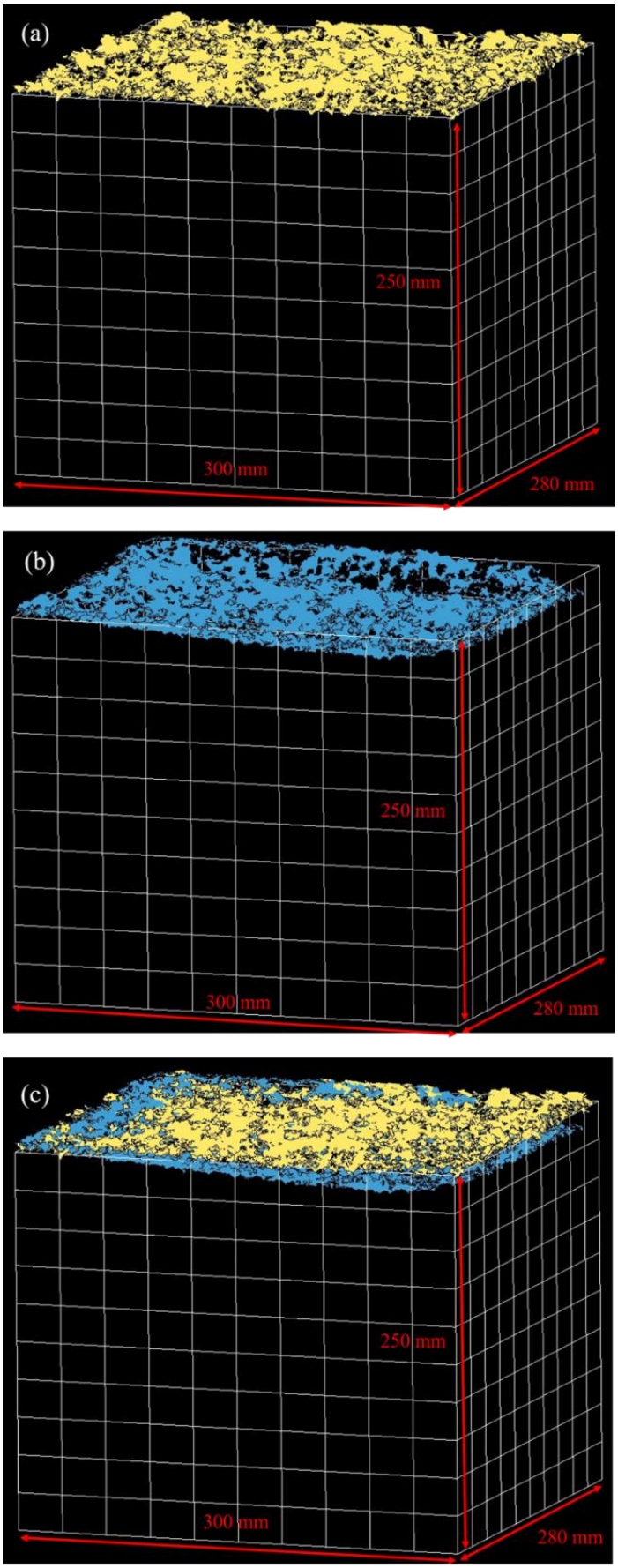

Figure 2.14: Point clouds obtained from the 3D scanner:
(a) initial ground surface, (b) after 40 passes, (c) both superimposed.

Figure 2.15: Particle surface after 40 passes of the 3.64 kg module travelling at 256 mm/s.

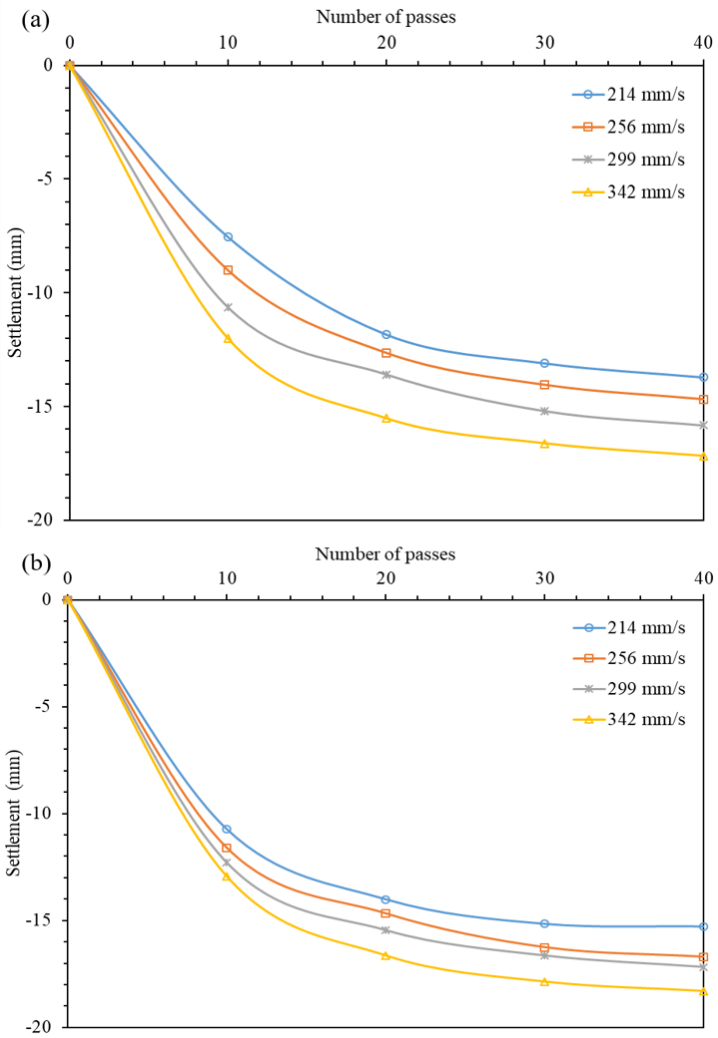

Figure 2.16: Average ground settlement results: (a) 3.64 kg scale module, (b) 5.46 kg scale module.

2.4 Summary and Conclusions

This paper has presented a unique and novel physical modelling method, using transparent soil, a CCD camera and the PIV technique, to study the mechanics and characteristics of rolling dynamic compaction (RDC). Two, 1:13 scale model replicas of the 8- and 12-tonne, 4-sided impact rollers have been examined. The 5.46 kg module induces greater soil displacements when compared against the 3.64 kg module tested at four different speeds. For both the 3.64 and 5.46 kg modules, the optimal speed for ground improvement is found to be approximately 299 mm/s. The most pronounced soil displacements occur within the first 20 passes and, subsequently, the soil displaces modestly. No obvious soil displacement is observed after 35 passes. A high-fidelity 3D scanner was employed to measure the ground settlement induced by the module. The value of the ground settlement exhibits an increasing trend with respect to rising operating speeds. Whilst the results of the present study are limited to a single initial density and particle size distribution, the conclusions presented are nevertheless valuable in providing greater insight into RDC-influenced ground improvement and many of the factors which affect it.

2.5 Acknowledgements

The authors are grateful to Mr. Stuart Bowes and the staff at Broons Hire (SA) Pty. Ltd. for their assistance in the provision of the testing facility and for the assistance in the experiments at Gillman. The authors also wish to acknowledge the technical staff from the School of Civil, Environmental and Mining Engineering at the University of Adelaide, especially Gary Bowman and Simon Golding, for their valuable assistance in the experimental work presented in this paper.

2.6 References

Adrian, R.J. 1991. Particle-imaging techniques for experimental fluid mechanics. Annual review of fluid mechanics, **23**(1): 261-304.

Ahmed, M., and Iskander, M. 2012. Evaluation of tunnel face stability by transparent soil models. Tunnelling and Underground Space Technology, **27**(1): 101-110.

Altaee A., and Fellenius, B.H. 1994. Physical modeling in sand. Canadian Geotechnical Journal, **31**(3): 420-431.

Avalle, D.L. 2006. Reducing haul road maintenance costs and improving tyre wear through the use of impact rollers. *In* Proceedings of the Mining for Tyres Conference, Perth, Australia, pp. 1-5.

Avalle, D.L. 2007. Ground vibrations during impact rolling. *In* Proceedings of the 10th Australia - New Zealand Conference (ANZ) on Geomechanics, Brisbane, Australia, pp. 1-6.

Avalle, D.L., and Carter, J.P. 2005. Evaluating the improvement from impact rolling on sand. *In* Proc. 6th Int. Conf. on Ground Improvement Techniques, Coimbra, Portugal, pp. 8.

Avalle, D.L., and Mckenzie, R.W. 2005. Ground improvement of landfill site using the square impact roller. Australian Geomechanics, **40**(4): 15-21.

Avalle, D.L., Scott, B.T., and Jaksa, M.B. 2009. Ground energy and impact of rolling dynamic compaction e results from research test site. *In* Proceedings of the 17th International Conference on Soil Mechanics and Geotechnical Engineering, Vol. 3, Alexandria, Egypt, pp. 2228-2231.

Bo, M.W., Na, Y.M., Arulrajah, A., and Chang, M.F. 2009. Densification of granular soil by dynamic compaction. Proceedings of the Institution of Civil Engineers-Ground Improvement, **162**(3): pp. 121-132.

Bouazza, A., and Avalle, D.L. 2006. Effectiveness of rolling dynamic compaction on an old waste tip. *In* ISSMGE 5th International Congress on Environmental Geotechnics, Cardiff, pp. 1-7.

Bransby, P., and Milligan, G. 1975. Soil deformations near cantilever sheet pile walls. Geotechnique, **25**(2): 175-195.

Carvalho, T., Suescun-florez, E., Omidvar, M., and Iskander, M. 2015. A nonviscous water-based pore fluid for modeling with transparent soils. Geotechnical Testing Journal, **38**(5): 805-811.

Clifford, J.M. 1980. The development and use of impact rollers in the construction of earthworks in southern Africa. CSIR Report 373, National Institute for Transport and Road Research, Pretoria, South Africa.

Chung, O.Y., Scott, B.T., Jaksa, M.B., Kuo, Y.L., and Airey, D. 2017. Physical modeling of rolling dynamic compaction. *In* Proceedings of the 19th Int. Conf. on Soil Mechanics and Geotechnical Engineering, Seoul, Korea., 18–22 September 2017, pp. 905–908.

Feng, S.J., Du, F.L., Shi, Z.M., Shui, W.H., and Tan, K. 2015. Field study on the reinforcement of collapsible loess using dynamic compaction. Engineering geology, 185: 105-115.

Iskander, M. 2010. Modelling with transparent soils: Visualizing soil structure interaction and multi phase flow, non-intrusively. Springer. ISBN-13: 978–3642025006.

Jafarzadeh, F. 2006. Dynamic compaction method in physical model tests. Scientia Iranica, **13**(2): 187-192.

Jaksa, M.B., Scott, B.T., Mentha, N.L., Symons, A.T., Pointon, S.M., Wrightson, P.T., and Syamsuddin, E. 2012. Quantifying the zone of influence of the impact roller. *In* Proceedings of ISSMGE-TC 211 International Symposium on Ground Improvement, Brussels, Belgium, 30 May – 1 June, Vol. 2, pp. 41–52.

Jaksa, M.B., Airey, D.W., Scott, B.T., Kuo, Y.L., Ranasinghe, R.A.T.M., Bradley, A.C., Chung, O.Y., Li, Y., and Chen, Y. 2019. Quantifying the Effect of Rolling Dynamic Compaction. *In* Proceedings of the 4th World Congress on Civil, Structural, and Environmental Engineering. Rome, Italy. doi: 10.11159/icgre19.1.

Kuo, Y.L., Jaksa, M.B., Scott, B.T., Bradley, A.C., Power, C.N., Crisp, A.C., and Jiang, J.H. 2013. Assessing the effectiveness of rolling dynamic compaction. *In* Proceedings of the 18th International Conference on Soil Mechanics and Geotechnical Engineering, Paris., vol. 2, pp. 1309–1312.

Li, Y., Airey, D., and Jaksa, M. 2020. Evaluating the effective depth of rolling dynamic compaction with a three-sided compactor. International Journal of Physical Modelling in Geotechnics, pp. 1-15. Available from https://doi.org/10.1680/jphmg.20.00079 [accessed 2 February 2021].

Liu, J. 2009. Visualizing 3-D internal soil deformation using laser speckle and transparent soil techniques. Geotechnical Special Publication, 189: 123-128.

Liu, J., and Iskander, M.G. 2010. Modelling capacity of transparent soil. Canadian Geotechnical Journal, **47**(4): 451-460.

Liu, J., Liu, M., and Gao, H. 2010. Influence of pile geometry on internal sand displacement around a laterally loaded pile using transparent soil. *In* Proceedings of Sessions of Geo Shanghai, Shanghai, China., June. ASCE, pp. 104-110.

Mandava, S.S., Watson, A.T., and Edwards, C.M. 1990. NMR imaging of saturation during immiscible displacements. AIChE journal, **36**(11): 1680-1686.

Omidvar, M., Chen, Z., and Iskander, M. 2014. Image based lagrangian analysis of granular kinematics. Journal of Computing in Civil Engineering, **29**(6): 04014101. DOI: 10.1061/(ASCE)CP. 1943-5487.000043.

Pak, A., Shahir, H., and Ghassemi, A. 2005. Behavior of dry and saturated soils under impact load during dynamic compaction. *In* Proceedings of 16th International

Conference on Soil Mechanics and Geotechnical Engineering, Osaka, Japan., pp. 1245-1248.

Pinard, M. 1999. Innovative developments in compaction technology using high energy impact compactors. *In* Proceedings 8th Australia New Zealand Conference on Geomechanics: Consolidating Knowledge. Australian Geomechanics Society, pp. 775-781.

Posadas, D., Tannus, A., Panepucci, H., and Crestana, S. 1996. Magnetic resonance imaging as a non-invasive technique for investigating 3-D preferential flow occurring within stratified soil samples. Computers and Electronics in Agriculture, **14**(4): 255-267.

Rajarathnam, P., Airey, D.W., Masoudian, M.S., and Jaksa, M.B. 2016. Model Tests of Rolling Dynamic Compaction. *In* Proc. 19th Southeast Asian Geotechnical Conf. and 2nd AGSSEA Conf., Kuala Lumpur, May 31 – June 3. pp. 505–510.

Scott, B., and Jaksa, M. 2014. Evaluating rolling dynamic compaction of fill using CPT. *In* Proceedings of the 3rd International Symposium on Cone Penetration Testing, pp. 941-948.

Scott, B., Jaksa, M., and Kuo, Y. 2012. Use of proctor compaction testing for deep fill construction using impact rollers. *In* Proc. Int. Conf on Ground Improvement and Ground Control, Wollongong, Australia., pp. 1107-1112. doi: 10.3850/978-981-07-3560-9_04-0412.

Scott, B., Jaksa, M., and Syamsuddin, E. 2016. Verification of an impact rolling compaction trial using various in situ testing methods. *In* Proc. of 5th Int. Conf. on Geotechnical and Geophysical Site Characterisation, Gold Coast, Australia., pp. 735-740.

Scott, B.T., Jaksa, M.B., and Mitchell, P.W. 2019. Ground response to rolling dynamic compaction. Géotechnique Letters, **9**(2): 99–105.

Scott, B.T., Jaksa, M.B., and Mitchell, P.W. 2020. Influence of towing speed on effectiveness of rolling dynamic compaction. Journal of Rock Mechanics and Geotechnical Engineering, **12**(1): 126-134.

Shining 3D. 2019. EinScan-Pro series user manual version 3.3.0.0. Available from https://it3d.com/wp-content/uploads/download-files/manual/en/EXScan-Pro-User-Manual-V3.3.0.2.pdf. [accessed 12 October 2019].

Stanier, S.A., Blaber, J., Take, W.A., and White, D. 2015. Improved image-based deformation measurement for geotechnical applications. Canadian Geotechnical Journal, **53**(5): 727-739.

Chapter 3.

Investigating the effectiveness of Rolling Dynamic Compaction (RDC) using Discrete Element Method (DEM)

Statement of Authorship

Title of Paper	Investigating the Effectiveness of Rolling Dynamic Compaction (RDC) Using Discrete Element Method (DEM).
Publication Status	☑ Published ☐ Accepted for Publication ☐ Submitted for Publication ☐ Unpublished and Unsubmitted w ork w ritten in manuscript style
Publication Details	Chen, Y., Jaksa, M.B., Kuo, Y.L., Airey, D.W. 2021. Investigating the Effectiveness of Rolling Dynamic Compaction (RDC) Using Discrete Element Method (DEM). Granular Matter, Available from https://doi.org/10.1007/s10035-021-01164-9.

Principal Author

Name of Principal Author (Candidate)	Yue Chen		
Contribution to the Paper	Developed the numerical model, contributed to methodology, analysis and interpretation of the data, wrote manuscript.		
Overall percentage (%)	80%		
Certification:	This paper reports on original research I conducted during the period of my Higher Degree by Research candidature and is not subject to any obligations or contractual agreements with a third party that would constrain its inclusion in this thesis. I am the primary author of this paper.		
Signature		Date	08 October 2021

Co-Author Contributions

By signing the Statement of Authorship, each author certifies that:

i. the candidate's stated contribution to the publication is accurate (as detailed above);
ii. permission is granted for the candidate in include the publication in the thesis; and
iii. the sum of all co-author contributions is equal to 100% less the candidate's stated contribution.

Name of Co-Author	Mark Jaksa		
Contribution to the Paper	Provided primary supervision, initial concept, contributed to the methodology, helped evaluate and edit the manuscript.		
Signature		Date	15/10/21

Name of Co-Author	Yien Lik Kuo		
Contribution to the Paper	Provided secondary supervision, assisted with research direction, helped edit the manuscript.		
Signature		Date	08 Oct 2021

Please cut and paste additional co-author panels here as required.

Name of Co-Author	David Airey		
Contribution to the Paper	Assisted with research direction, helped edit the manuscript.		
Signature		Date	15/10/2021

Please cut and paste additional co-author panels here as required.

Investigating the effectiveness of Rolling Dynamic Compaction (RDC) using Discrete Element Method (DEM) (Paper 2)

Abstract

Rolling dynamic compaction is a soil compaction technique which involves compacting the ground with a heavy, non-circular module. Compared with traditional compaction methods, it is, in most cases, more efficient, as it improves the soil to a greater depth and it facilitates more rapid ground improvement due to its higher travel speeds. However, to date, there is a limited understanding of the nature of the subsurface improvement as a result of RDC. This paper presents a three-dimensional finite element method (FEM)-discrete element method (DEM) model which simulates the movement of soil particles, and the porosity, and hence density, variations during the RDC process. The FEM-DEM model is developed using experimental tests, and the numerical results are in good agreement with the laboratory test results. The effectiveness of 1:13 scale models of the 4-sided, 8- and 12-tonne, Broons BH-1300 and BH-1300 HD impact rollers are analysed based on the soil porosity variations. The relationships between porosity, soil displacements and the motion of the roller module are also investigated. The results of this study demonstrate the capability of the FEM-DEM model to simulate reliably the ground improvement induced by RDC.

3.1 Introduction

Soil compaction is a common approach to improve the ground for engineering purposes. After compaction, the density and bearing capacity of the soil increase, which means that the ground has improved strength and stiffness resulting in reduced settlements and enhanced performance. Compaction of the ground facilitates the construction of structures on sites which would otherwise be considered less than ideal for such purposes. In the field, soil compaction is often achieved through the use of mechanical equipment,

such as heavy tamping, drum and sheepsfoot rollers, and vibrating plates. The variety of soil compaction methods are generally divided into two sub-categories, static and dynamic, based on the type of applied compactive effort. Static compaction compresses the soil by the self-weight of the equipment, whereas dynamic compaction makes use of high energy impact forces in addition to the self-weight of the equipment. Rolling dynamic compaction (RDC) is a relatively new dynamic compaction method which has become increasingly popular in recent years. It involves towing a heavy (6–12 tonnes), non-circular (3-, 4- and 5-sided) module behind a tractor to achieve soil compaction. The module rotates about its corner and falls to impact the ground. Mechanical energy induced by the roller increases the soil density by rearranging the soil particles and reducing the voids within the soil. Compared with conventional static and vibratory compaction techniques, RDC improves the ground to a greater depth, typically between 1-3 m, depending on soil type and ground conditions (Avalle and Carter, 2005). In addition, RDC is effective when it is applied to large and open sites, since it can travel at a speed of 10-12 km/h, whilst traditional drum rollers travel at 4 km/h (Pinard, 1999). Field tests have been undertaken by previous researchers (Avalle and Carter, 2005; Jaksa et al., 2012; Scott and Jaksa, 2014; Scott et al., 2016) to assess the efficacy of RDC. Several in situ tests were conducted to measure the energy transfer, the zone of influence and the ground settlement induced by RDC. Since undertaking field tests is expensive and time consuming, Rajarathnam et al. (2016) studied the effectiveness of RDC using a 1:20 physical scale model of a 3-sided module and Chung et al. (2017) and Chen et al. (2021) employed a 1:13, 4-sided scale model. The use of small scale models allows RDC to be assessed in a controlled laboratory environment and avoids conducting expensive field tests. According to Chung et al. (2017), the 1:13 physical scale model produces similar ground responses to the full-size prototype based on the scaling law developed by Altaee and Fellenius (1994). Chen et al. (2021) evaluated the effectiveness of the physical scale

model from four aspects, namely ground settlement, improvement depth, the optimum number of rolling passes, and the optimal operating speed. Although conducting small-scale tests is more efficient than carrying out field trials, small-scale tests still require time and effort to prepare and undertake the tests, and the relationship between the laboratory and field measurements is a topic for ongoing research. With the development of high performance computers, numerical simulations have been adopted by many researchers to study ground responses induced by RDC. The finite element method (FEM) was adopted by Kuo et al. (2013) and Bradley et al. (2019) to simulate the behaviour of a full-size, 4-sided RDC module using the LS-DYNA (LSTC, 2018) computer program. Soil settlements and influence stresses obtained from the FEM model were validated using field test results for both static and dynamic loadings. The FEM model was shown to be capable of predicting soil displacements and soil stresses under the impact roller. In addition, the FEM model was used to estimate the energy imparted to the soil by RDC (Bradley et al., 2019). Although, the FEM model has shown encouraging results in terms of simulating the ground response induced by RDC, the motion of soil particles and porosity (and hence density) changes within soil mass remain elusive, given the limitations of constitutive models and continuum based methods, such as FEM, more generally.

The discrete element method (DEM) was introduced by Cundall and Strack (1979) to simulate the behaviour of granular materials. Given that soils are particulate materials, DEM provides a better understanding of the micromechanical behaviour of soil at the particle scale. Soil particles are modelled in DEM as undeformable spheres with deformable contacts (Gabrieli et al., 2009). One of the advantages of DEM is that it can track the movement of every individual particle to provide detailed information about the

deformation of the entire soil body, which offers opportunities to simulate soil particles under large deformations.

Since the traditional FEM is used routinely in geotechnical engineering to simulate the deformation of a soil mass, but it is unable to model the micromechanical behaviour of particles, and DEM is able to model particle movements and interactions, there is a need to combine the advantages of these two methods into a single numerical model in order to increase the efficacy of the numerical simulation. A FEM-DEM combined approach has been applied to simulate the dynamic packing and quasi-static interactions of granular particles (Farsi et al., 2015) and to assess wear of a tipper using LS-DYNA (Forsström and Jonsén, 2016). These studies demonstrated the capabilities and accuracy of the combined FEM-DEM approach when simulating geomechanical problems.

This paper develops a three-dimensional FEM-DEM model to simulate granular particles and the results of this model are then used to analyse the behaviour of 1:13 scale models of the 4-sided, 8- and 12- tonne, Broons BH-1300 and BH-1300 HD impact rollers, respectively. In the numerical simulation, soil particles are modelled using the DEM and the 4-sided scaled module is simulated by the FEM, which is similar to the numerical, full-size RDC model developed by Kuo et al. (2013) and Bradley et al. (2019), but with scaled properties. The numerical model is validated against experimental results obtained by Chen et al. (2021), as discussed below.

3.2 DEM Modelling

3.2.1 Basic features

The commercial software LS-DYNA is used to perform the FEM-DEM simulation in this study. Since particle movements and interactions are the main focuses of this study, a

three-dimensional numerical simulation is applied to model better the behaviour of soil particles. In DEM, granular materials are simplified as rigid spheres with soft contacts, which means particles are permitted to overlap at contact points. The macroscopic behaviour of granular materials is captured by interactions between particles. In general, DEM consists of two main stages. The first stage is using a contact model to describe the forces acting on the particles. Subsequently, Newton's second law of motion is adopted to calculate particle displacements at each time step based on any unbalanced forces. There are a number of contact models to simulate interactions between particles, that vary from linear to the highly non-linear. The linear contact model is the most popular and widely used since it is simple and efficient. It has fewer parameters that need to be calibrated when compared with other contact models. Complex highly non-linear contact models require more computational time to run the model and to calibrate the microscopic parameters. Previous research has shown that the linear contact model is able to appropriately replicate the properties of granular materials and it can be used reliably to study geotechnical problems (Gabrieli et al., 2009; Jiang et al., 2014; Chen et al., 2018; Huang et al., 2019). As a result, the linear contact model is adopted in this study. In this model, the contact forces between two overlapped particles are represented by a linear spring and a dashpot in the normal direction, a linear spring and a dashpot in the shear direction, and a frictional slip is permitted in the shear direction with a coefficient of friction. Therefore, in total, five microscopic parameters are needed as inputs, namely the normal and shear stiffnesses (k_n and k_s, respectively), normal and shear damping ratios (β_n and β_s, respectively), and the coefficient of friction (μ). These input parameters can be determined through a calibration approach, which is often achieved using standard geotechnical tests, such as the direct shear, biaxial/triaxial or uniaxial compression tests (Coetzee, 2017). Similar to the interaction between finite elements, the contact between discrete particles and finite elements is defined using a penalty-based contact algorithm,

if penetration of the discrete particles, through the contact surface of the finite elements, is identified (LSTC, 2018). The contact force is proportional to the penetration depth, which is treated by placing springs between the contact elements. The stiffnesses of these springs define the magnitude of the contact forces, which are calculated using Equation (3.1). If the stiffnesses of the contact elements are different, LS-DYNA adopts the minimum stiffness. The contact frictional force is calculated based on Coulomb's law of friction, if there is sliding between the contacts.

$$k_i = \frac{f_s \cdot A_i \cdot K_i}{V_i} \tag{3.1}$$

where k_i is the stiffness of the spring (i) placed between particles and the contact finite elements; f_s is the penalty scale factor (the default value of unity is used in the simulations); and A_i, V_i and K_i are the contact area, the volume and the stiffness of the contacted elements, respectively.

As mentioned above, experimental 1:13 scale model tests were conducted by Chen et al. (2021), and the results of these tests are used to validate the FEM-DEM model in this study. The experimental scale model tests involved using a 1:13 scale 4-sided RDC module to traverse an acrylic chamber (300 mm long × 280 mm wide × 250 mm high) which was filled with fused quartz. Internal displacements of the soil particles along the centreline of the module traverse lane were captured using a conventional charge-coupled device (CCD) camera, and the soil displacement fields were obtained using the *GeoPIV_RG* MATLAB module, which is an implementation of the particle image velocimetry (PIV) technique. In this study, LS-DYNA is used to simulate the experimental process adopted by Chen et al. (2021). The behaviour of the fused quartz is simulated by the DEM. Since fused quartz particles are angular in shape, in order to mimic the irregular shape of fused quartz without introducing any new microscopic parameters

that need to be calibrated, the rotation of the spheres in the DEM model is restricted. This method is efficient as it increases the macroscopic shear strength of the numerical models without changing the shape of particles or introducing additional input parameters. According to Calvetti et al. (2003); Calvetti et al. (2004) and Gabrieli et al. (2009), the rotation of particles was prohibited to constrain the effects of the spherical shape, since spheres perform rotational movements relatively easily. They reported that the capability of numerical models to replicate the behaviour of granular materials was unaffected by prohibiting the rotation of spheres, if the microscopic friction coefficient was calibrated accordingly.

According to Wang and Leung (2008), quartzose material has a bulk modulus to shear modulus ratio close to 1. Therefore, in the numerical simulations that follow, the ratio between the normal and shear stiffnesses is chosen to be 1. As shown in Equation (3.2), the damping ratio (β) of the dashpots between the DEM particles relates to the coefficient of restitution (COR) (Antypov and Elliott, 2011), which is defined as the ratio of the velocities after and before impact between the particles. The COR for contact between quartzose material is approximately 0.8 from drop test results (Imre et al., 2008), which then yields the damping ratio of approximately 0.07. In addition, a small numerical damping ratio (β = 0.1) was suggested by Gabrieli et al. (2009) to better simulate the triggering of failure. Therefore, small numerical normal and shear damping ratios (β_n = β_s = 0.1) are selected in all simulations, considering the value of the COR and the simulation of the triggering of failure.

$$\beta = -\frac{\ln e}{\sqrt{(\ln e)^2+\pi^2}} \tag{3.2}$$

where β is the damping ratio of viscous dashpots; and e is the coefficient of restitution.

3.2.2 DEM input parameters calibration

DEM input parameters were calibrated against consolidated drained (CD) triaxial tests performed by the authors on dry fused quartz with the same grading as used in the physical model experiments (Chen et al., 2021). Figure 3.1 presents the experimental and numerical particle size distribution curves. The size of the experimental fused quartz is between 3 to 5 mm, with D_{50} = 3.84 mm (black solid line). The particle sizes adopted in the numerical simulations of the triaxial tests (black dashed line) were very similar to the experimental tests. In the numerical model, spherical particles were generated according to a Gaussian distribution by specifying the maximum and minimum diameters, and a mean of 4 mm.

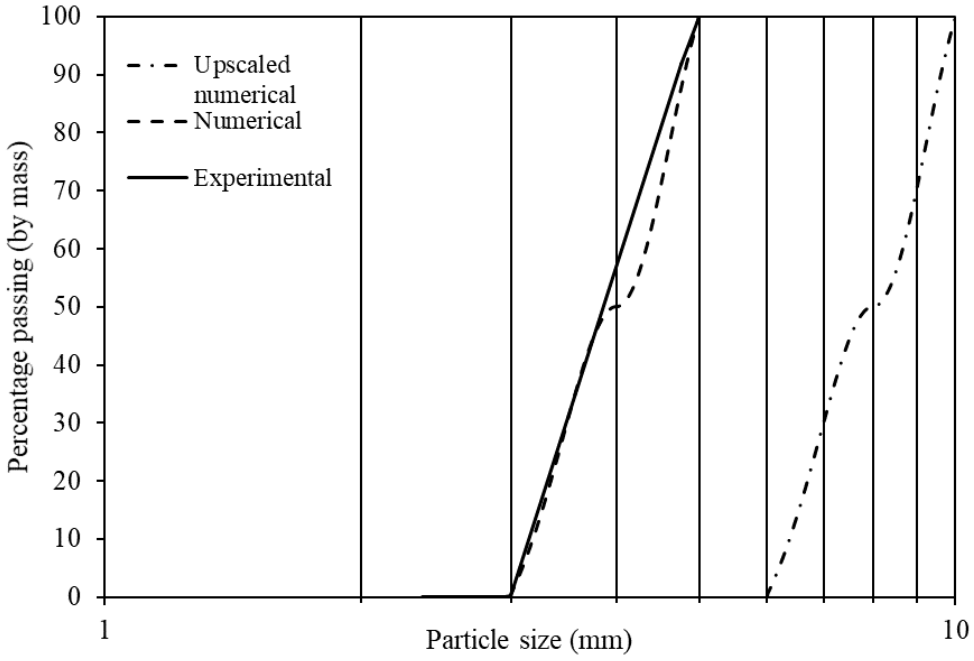

Figure 3.1: Numerical and experimental particle size distribution curves.

Conventional triaxial tests were performed on samples, which were 50 mm in diameter and 100 mm high. Numerical simulations of these tests were performed using the configuration shown in Figure 3.2. The finite elements were used to model the flexible membrane and two loading caps, while the DEM was employed to simulate soil particles.

The friction coefficient between the DEM particles and the finite elements were obtained from a numerical inclined plane test, which has been used by several researchers (Chou et al., 2012; González-Montellano et al., 2012). In the laboratory, fused quartz triaxial samples were prepared by dry pluviation into a mould. In the numerical simulations, spheres were generated randomly to fill an enclosed cylinder and then pluviated into the membrane under gravity at a relatively constant height. Particles were slightly filled above the level of the membrane to permit modest compaction. The top loading cap was then moved up and down by 20 mm at 200 mm/s for 2 seconds to compact the particles and to match the experimental porosity. A total of approximately 3,500 particles were used in the triaxial test simulations. When the particles reached an equilibrium state, the confining pressures were applied to the sample equally in all directions and were maintained during the tests. Three confining pressures were simulated in this study, 25, 50 and 100 kPa. During the shearing stage, axial strain was applied by displacing the top plate vertically at a constant velocity, which was slow enough to ensure a quasi-static condition, until the axial strain reached 20%. Axial strain was calculated from the displacement of the top loading cap, while stresses were determined from the contact forces between the top loading cap and the particles in contact with the top cap. In the physical triaxial tests, the loading rate was set at 1 mm/min. However, due to the computational and time constraints, the numerical samples were sheared at a higher loading rate. The effects of different loading rates on the numerical triaxial tests results were investigated, and a loading rate of 10 mm/s was chosen in all triaxial test simulations, as it is the fastest loading rate which provided a computationally efficient and reliable model. A similar procedure for selecting an appropriate loading rate for numerical triaxial tests was reported by Mahabadi et al. (2010), Kozicki et al. (2014) and Gu et al. (2017). In addition, as suggested by Da Cruz et al. (2005), Xu et al. (2020), Zhang et al. (2020) and Wu et al. (2021), the inertial number should smaller than 10^{-3} to maintain a quasi-

static condition in the numerical model. Based on Equation (3.3), the maximum inertial number was approximately $1.07\times10^{-4}<10^{-3}$, which indicated the numerical triaxial tests were conducted in a quasi-static condition during the shearing stage. The minimum pressure along the top and bottom loading caps was approximately 902 kPa when the top loading cap was moved up and down to compact the particles; therefore, the maximum inertial number was 3.57×10^{-4}, which implied the numerical particle assembly was in a quasi-static condition during sample preparation.

$$I = \dot{\varepsilon}\sqrt{\frac{m}{pd}} \tag{3.3}$$

where I is the inertia number; $\dot{\varepsilon}$ is the shear strain rate; m and d are the mass and diameter of particles, respectively; and p is the confining pressure.

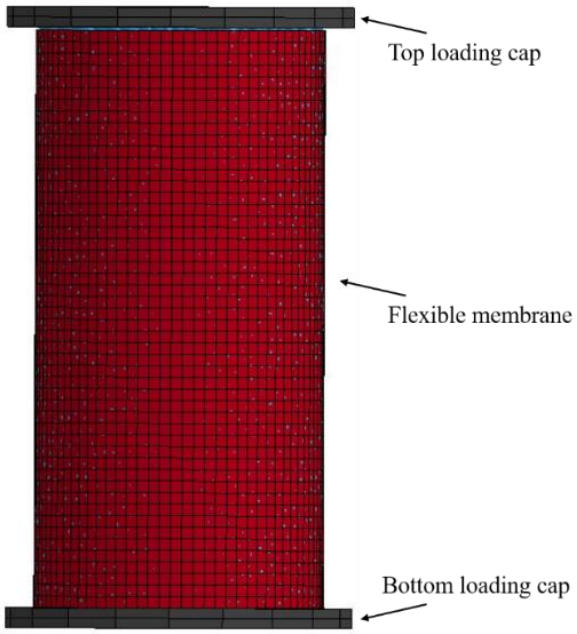

Figure 3.2: Numerical triaxial test sample.

The calibration process involved an iterative, trial-and-error approach, where the five numerical inputs were varied in-turn, until the numerical results conformed to the experimental measurements. The final calibrated result is shown in Figure 3.3. As can be seen, in general, the experimental triaxial tests results are well predicted by the numerical

model; although the peak deviatoric stresses are somewhat overestimated, and volumetric strains are slightly underestimated by the numerical model. As can also be observed, the numerical stress-strain results show a degree of fluctuation, and this is because the contact stiffness between particles is relatively high, which causes the numerical model to be less stable. The same phenomenon was reported by Sadek and Chen (2014) and Nandanwar (2015). As the contact stiffness increases, greater fluctuation is shown in stress-strain curves, or in other words, a higher stiffness leads to a less stable model. Overall, the numerical stress-strain curves are in good agreement with the experimental results.

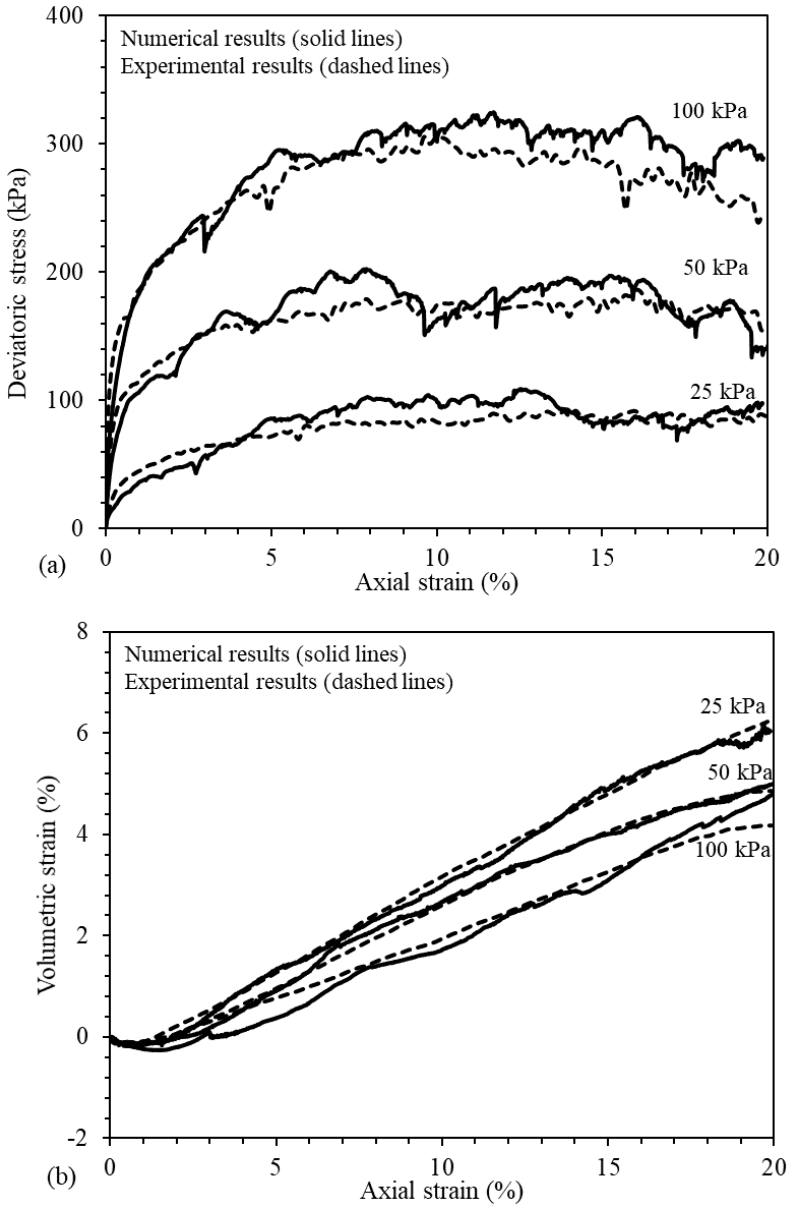

Figure 3.3: Experimental and numerical triaxial test results at confining pressures of 25, 50 and 100 kPa: (a) stress-strain curves, (b) volumetric curves.

The obtained, calibrated DEM input parameters are shown in Table 3.1. Since the size of the numerical particles was randomly generated according to a Gaussian distribution, in order to assess the effects of the randomly generated particles on the simulation results, all numerical triaxial tests were performed three times for each confining pressure, and the numerical particles were generated randomly each time. The numerical stress-strain curves presented in Figure 3.3 are the average of the three results obtained for each confining pressure.

Table 3.1: Microscopic parameters used in DEM simulations.

Parameter	Value
Specific gravity	2.20
Particle diameter (mm)	3–5
Coefficient of friction	0.306
Normal and shear stiffnesses (k_n and k_s) (N/m)	9.3×10^5
Normal and shear damping ratios (β_n and β_s)	0.1

3.3 Simulation of RDC

3.3.1 RDC model setup

In order to validate the behaviour of spherical particles using the calibrated DEM input parameters, the RDC simulation was conducted in the same manner as that of experimental tests (Figure 3.4). Therefore, a numerical model was developed which consisted of a simplified impact roller module, a chamber filled with DEM particles and two timber frames, as shown. Similar to Figure 3.4a, the roller travels from right to left and it compacts particles within the chamber in Figure 3.4b. The chamber was set to the same dimensions as that used in the experimental tests, namely 300 mm length × 280 mm

width × 250 mm height. The chamber and the two timber frames were modelled using the FEM, as rigid bodies with no deformation or displacement permitted.

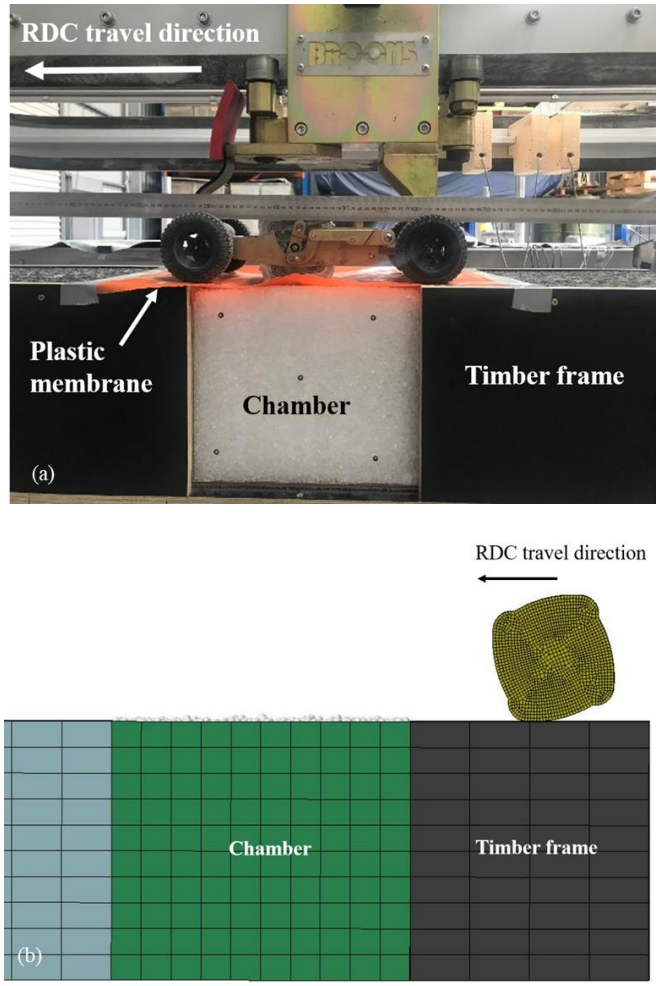

Figure 3.4: Setup of RDC tests: (a) experimental setup, (b) numerical setup.

In the numerical RDC simulations, the DEM particles were generated in a process similar to that adopted in the numerical triaxial tests. Particles were generated randomly to fill an enclosed box and then pluviated in successive layers into the chamber under gravity from the same approximate height of 280 mm. After the particles reached equilibrium, a rigid plate was placed on top of the particles, and moved up and down by 15 mm at 150 mm/s for 1 s to compact each of the soil layers. The minimum pressure along the rigid plate and the bottom of the chamber was approximately 1,109 kPa when the rigid plate compacted the soil. According to Equation (3.3), the maximum inertial number was 9.67×10^{-4}, which

indicated that the RDC model was in a quasi-static condition during the sample preparation stage. The assemblage porosity adopted in the numerical RDC simulations was 0.426, which accords with that used in the experiments (0.421). The numerical roller module used in this study was similar in shape to the full-size model used by Kuo et al. (2013) and Bradley et al. (2019), but to be consistent with the experiments a 1:13 scaled model was replicated, which is also shown in Figure 3.4a. As described by Kuo et al. (2013) and Bradley et al. (2019), the roller is effectively rigid relative to the stiffness of the soil and hence, the deformation of the roller during compaction is negligible. Therefore, in the numerical model, the roller was simulated using finite elements and defined as a rigid material. The adoption of the FEM is necessary to simulate the boundaries and the roller. The timber frames, at each end of the chamber, were modelled using the FEM to facilitate the compaction process. In addition, it is important to accurately simulate the complex characteristics of the roller module, since these significantly affect the ground improvement results (Bian et al., 2002). The FEM is able to simulate the roller module accurately and efficiently. The numerical roller module was developed based on a computer aided drawing (CAD) that was provided by Broons, which is an accurate representation of the Broons' impact roller. The Young's modulus of elasticity and Poisson's ratio of the roller were 210 GPa and 0.28, respectively. The properties (such as, dimensions, weights and operating speeds) of the 1:13 impact roller modules were converted from the full-size prototypes using the scaling laws [Equations (3.4) to (3.6)] suggested by Altaee and Fellenius (1994). In this study, the geometric scale ratio (n) is 1/13. Two different weights of modules (3.64 and 5.46 kg) were studied, with identical dimensions of 115 × 115 × 100 mm (height × length × width), which correspond to the 8- and 12-tonne impact rollers (Broons BH-1300 and BH-1300 HD), respectively.

$$\frac{V_m}{V_p} = n \tag{3.4}$$

$$\frac{L_m}{L_p} = n \tag{3.5}$$

$$\frac{M_m}{M_p} = n^3 \tag{3.6}$$

where V represents the operating speed; L is the characteristic length; M is the mass; n is the geometric scale ratio; and the subscripts m and p denote the scale model and prototype, respectively.

Particle sizes used in the numerical calibration tests were the same as the fused quartz sizes used in the experiments. Since the dimensions of triaxial tests samples were relatively small this resulted in a manageable number of numerical particles. However, in order to compare the numerical simulation results with the measurements from the experimental tests, the dimensions of the chamber used in the simulations needs to be the same. If actual particle sizes are used in the numerical simulation, a large number of particles (approximately 400,000) will be required, which is computationally intensive and time-consuming. Therefore, to obtain an appropriate balance between the computational time and the numerical accuracy, the particles were all scaled up to be two times larger than the actual particle sizes. Diameters of the scaled particles were 6–10 mm, which consequently reduced the number of particles to approximately 42,000. The scaled particle size distribution is included in Figure 3.1, shown previously. Since all the particles were scaled up, the shape of the particle size distribution curve remained the same and, as shown by Yang et al. (2006), the porosity of the samples is independent of the particle scaling factor. The porosity of the particles near the boundaries of the chamber may be altered. However, similar to Chen et al. (2021), to minimise boundary effects, ground improvement is investigated solely in the central region of the module traverse lane. In addition, as reported by Chen et al. (2021), the most significant ground

improvement occurred within the upper 150 mm depth and displacements of soil particles near the bottom of the chamber are negligible after 40 module passes. Therefore, ground improvement near the bottom of the chamber is insignificant. The upper limit of particle scaling is related to the dimensions of the model. In this study, the dimensions of the roller module is relevant, which affects the loaded surface that is directly in contact with the particles. Since the width (100 mm) is smaller than the length (115 mm) of the module, the width is the most relevant dimension and it determines the upper limit of particle scaling. The D_{50} of the scaled particles (8 mm) is one order of magnitude less than the width of the module (100 mm), which ensures an adequate number of particles remain in the model. This is consistent with Ciantia et al. (2015), who reported that the dimension of model was always one order of magnitude above the scaled average particle diameter, to ensure that the macroscopic responses of the particles were maintained after scaling. This same issue was addressed by Tatsuoka et al. (1997) who stated that the dimensions of the model needed to be at least ten times more than the average scaled particle sizes to avoid size effects.

Since the particles have been scaled up, the calibrated DEM input parameters also need to be scaled to ensure that the geometrical properties of the particles remain constant (Gabrieli et al., 2009). A mass scaling (particle density remains constant before and after scaling) is applied in this study. This scaling law has been adopted in many studies, such as Gabrieli et al. (2009), Evans and Valdes (2011), Ciantia et al. (2016), Zhou et al. (2016) and Wang et al. (2018). According to the mass scaling law, Young's modulus, the ratio between the shear and normal stiffnesses, the friction coefficient and damping ratios are scale invariant. The normal stiffness depends on the particle scaling factor and has a linear relationship with respect to particle diameter (Gabrieli et al., 2009; Feng and Owen, 2014). Hence, the value of normal stiffness is scaled up by a factor of 2 to equal 1.86×10^6 N/m.

Table 3.2 presents the scaled DEM input parameters that are used in the RDC simulations that follow.

Table 3.2: Scaled DEM input parameters.

Parameter	Value
Specific gravity	2.20
Particle diameter (mm)	6–10
Coefficient of friction	0.306
Normal and shear stiffnesses (k_n and k_s) (N/m)	1.86×10^6
Normal and shear damping ratios (β_n and β_s)	0.1

In LS-DYNA, the equations of motion are solved using the explicit central difference scheme. Therefore, the stability of the numerical model is conditioned to the employed time step. For a FEM-DEM model, the critical time step (Δt) is determined based on Equations (3.7)–(3.10) (LSTC, 2018). In this study, Δt is governed by Δt_{DEM}, which is 6.53×10^{-6} s.

$$\Delta t \leq min\{\Delta t_{DEM}, \Delta t_{FEM}\} \tag{3.7}$$

$$\Delta t_{DEM} = TSSFAC \cdot 0.2 \cdot \pi \cdot \sqrt{\frac{m}{k_n}} \tag{3.8}$$

$$\Delta t_{FEM} = \frac{l_{min}}{c} \tag{3.9}$$

$$c = \sqrt{\frac{E(1-\nu)}{(1+\nu)(1-2\nu)\rho}} \tag{3.10}$$

where Δt_{DEM} and Δt_{FEM} are the critical time steps for the discrete and finite elements, respectively; $TSSFAC$ is a time step scale factor in LS-DYNA, and the default value of $TSSFAC$ = 0.9 is used in this study; m and k_n are the mass and normal stiffness of the DEM particles, respectively; l_{min} is the minimum effective length of the finite elements;

c is the velocity of the elastic wave; and E, ν and ρ are the Young's modulus, Poisson's ratio and the mass density of the finite elements, respectively.

Similar to the experimental tests, both the 3.64 and 5.46 kg scale modules were examined in the simulations to investigate the effect of the module's weight on ground improvement. In this study, the modules were operated at a speed of 299 mm/s, which correspond to a prototype speed of 14 km/h. All simulations were conducted on the University of Adelaide's high-performance computer (2 × Intel Xeon Gold 6248 Processor @ 2.4 GHz) with each taking approximately 25 days to complete.

3.3.2 Arrangement of measurement spheres

In the numerical simulation, porosities and stresses within a granular body can be quantified by means of measurement spheres. By placing measurement spheres in the region of interest, changes in porosities and stresses can be monitored consistently within the sphere of interest. The size of the measurement spheres can affect the obtained porosity and stress results. Measurement spheres that are too small result in statistical errors and those that are too large result in a loss of resolution (Jiang et al., 2014). According to Chen et al. (2018) and Li et al. (2019), measurement spheres should incorporate at least 50 particles. Measurement spheres were created to facilitate the examination of porosity changes with respect to RDC, as shown in Figure 3.5. These measurement spheres are fixed at their respective locations throughout the simulation. In total, 60 measurement spheres (M1 to M60) were generated and porosity results were then used to assess the effectiveness of RDC. These measurement spheres were aggregated into 12 groups based on the horizontal distances from the left corner of the chamber and were numbered G1 to G12, as shown in Figure 3.5. It is important to note that, as mentioned earlier and in order to minimise boundary effects, ground improvement

is assessed only in the central section of the chamber, which concerns the region incorporating the G3, G4, G9 and G10 aggregated measurement spheres shown in Figure 3.5.

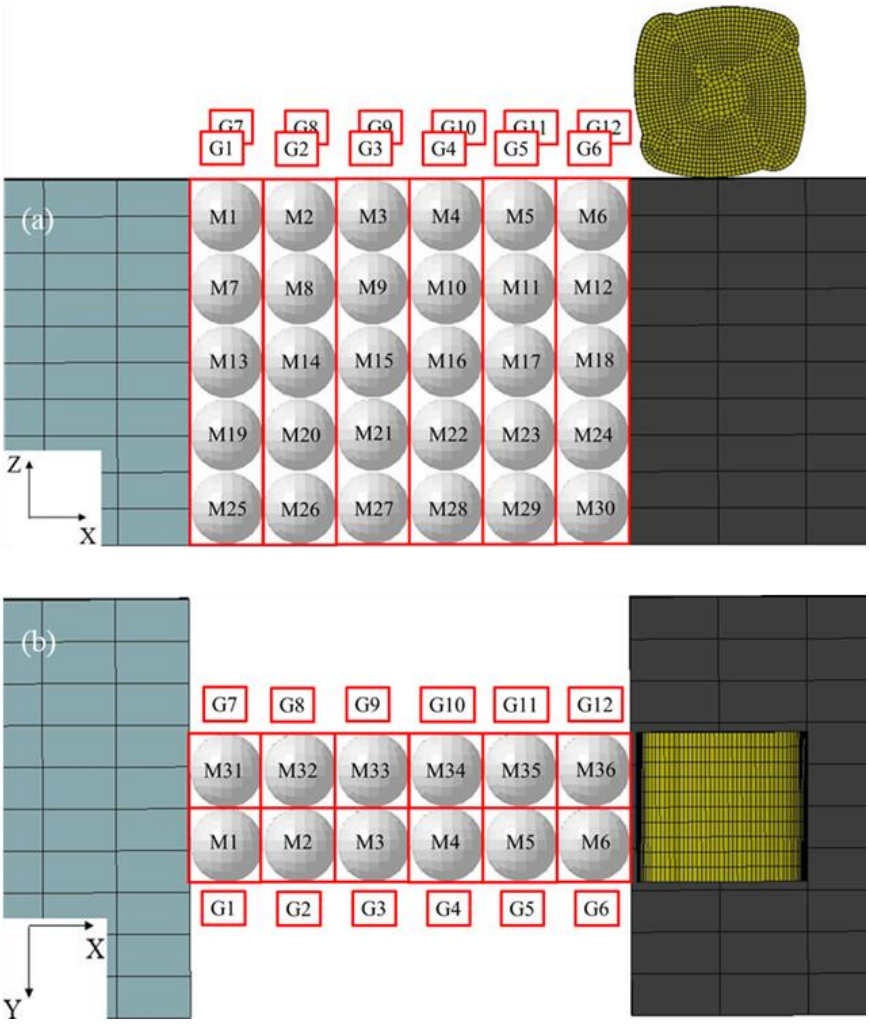

Figure 3.5: Arrangement of the measurement spheres in the module traverse lane: (a) side view, (b) plan view.

3.4 Results and Discussion

3.4.1 Verification of the DEM model

The ability of the numerical model in predicting ground settlements with respect to the number of passes is examined against the experimental test results. Consistent with Chen et al. (2021), in the numerical simulations, the front face of the chamber is divided into

three regions and, only soil improvement that occur in the central region is used to assess the effectiveness of RDC, as this region is less affected by the chamber's boundaries. Experimental ground settlements were obtained using a high-precision 3D surface scanner (EinScan Pro+) (Chen et al., 2021). The module traverse lane was scanned after every 10 module passes and the displacement of each captured particle within the central region of the chamber was summed and then averaged to calculate the average ground settlement with respect to the number of passes. Consistent with Chen et al. (2021), coordinates of an approximately one-particle thick layer of numerical particles, which is located at the ground surface of the module traverse lane, within the central region of the chamber, were recorded and averaged after every 10 module passes to obtain the numerical ground settlements. As shown in Figure 3.6, the numerical model performs well. As indicated, the heavier module (5.46 kg module) produces larger ground settlements, as one would expect.

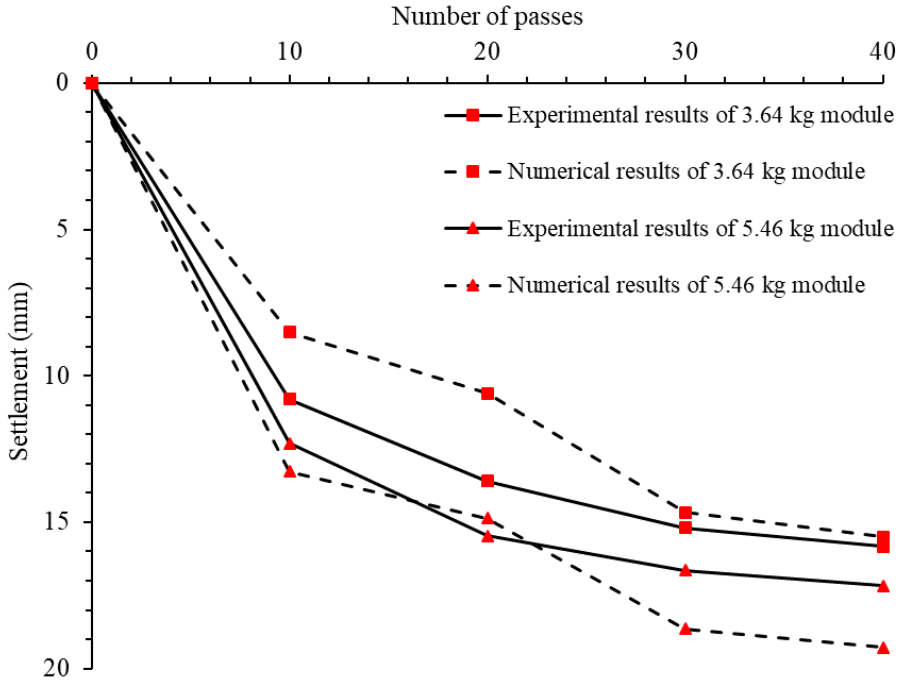

Figure 3.6: Ground settlements obtained from both the 3.64 and 5.46 kg modules.

In general, the ground settlements predicted by the numerical model are slightly different from those measured experimentally. There are a number of likely reasons for this. Firstly, the nature of the RDC physical scale model is more complex than the simplified numerical model, as the physical scale model involves, not only a 4-sided module, but also a spring-linkage system installed on both sides of the model (Figure 3.4a), which is a feature of the full-scale module. This system stores some of the potential energy by compressing the springs when the model is towed forward. The springs subsequently release the stored energy at the time the module just begins to rotate about its corner and impact the ground. As a result, this spring-linkage system facilitates and augments the rotation of the module. Secondly, four wheels are incorporated in the physical scale model to assist in its smooth operation, in contrast to the prototype's two. Finally, the DEM model incorporates spherical particles, whereas the experimental tests involved angular fused quartz.

In addition, numerical average vertical displacements at different depths below the ground are compared with those obtained from the experiments to validate the behaviour of the numerical model. Experimental soil displacements below the ground were measured from the movement of a one-particle thick layer of dyed fused quartz located along the centreline of the module compacted area, using a CCD camera and the PIV system (Chen et al., 2021). In the PIV analysis, subsets with a diameter of approximately 25 mm were adopted. The measured vertical displacements from the central region of the chamber were averaged over the subsets which had centres located at 50, 100, 150 and 200 mm depths below the ground. In order to compare the numerical results with those obtained experimentally, the numerical soil displacements were calculated by averaging coordinate changes of approximately a one-particle thick layer located along with the

centreline of the roller traverse lane at 37.5–62.5, 87.5–112.5, 137.5–162.5 and 187.5–212.5 mm depths below the ground within the central region of the chamber.

As shown in Figure 3.7, the numerical soil displacements are in excellent agreement with experimental results, for both the 3.64 and 5.46 kg scale modules after 40 passes. Displacements at depth of zero in Figure 3.7 represent the ground settlements obtained after 40 passes in Figure 3.6. A summary of the detailed soil displacements for the 3.64 kg module travelling at 299 mm/s is given in Table 3.3. It can be seen that maximum difference between the numerical and experimental results is 0.46 mm, and in terms of percentage difference, 25.5%. It should be noted that the 25.5% relates to a difference of 0.04 mm. It is clear that these differences are modest and, as a result, it can be concluded that the numerical model reasonably predicts the soil displacements observed in the experimental model tests.

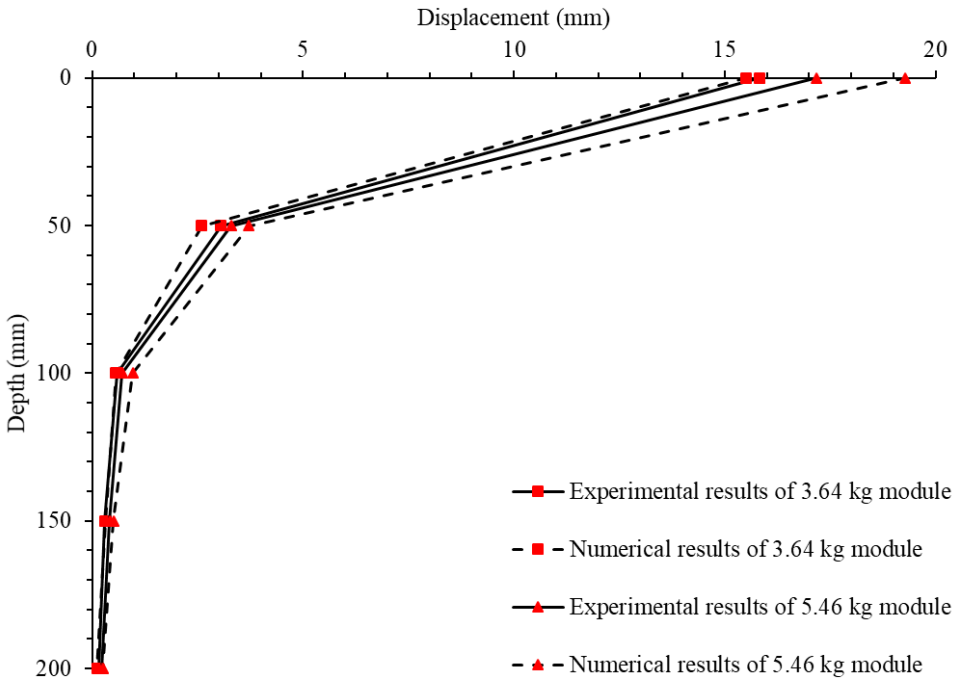

Figure 3.7: Soil displacements after 40 passes for both the 3.64 and 5.46 kg modules.

Table 3.3: Detailed soil displacement results for 3.64 kg module traverses at a speed of 299 mm/s after 40 passes.

Depth (mm)	Displacement (mm)		
	Experimental	Numerical	Difference (%)
0	15.83	15.51	–0.32 (–2%)
50	3.06	2.59	–0.46 (–15.1%)
100	0.59	0.56	–0.03 (–5.9%)
150	0.29	0.32	0.03 (8.8%)
200	0.15	0.11	–0.04 (–25.5%)

3.4.2 Porosity changes relative to the roller's motion

Figure 3.8 shows the motion of the module, the location of the measurement spheres and the velocity vectors of soil particles at different times during the first pass of the 5.46 kg module operating at 299 mm/s. Time, t = 0 s is defined as the moment when the module just leaves the timber frame at the right edge of the chamber (Figure 3.8a). The module then compacts the soil between t = 0.2 to 1.0 s (Figures 3.8b, c, d, e and f). When t = 1.2 s, the module leaves the chamber and travels to the left timber frame (Figure 3.8g). In general, it can be seen from the velocity vectors in Figures 3.8c and 3.8d that, when the module compacts the ground, the predominant motion of the particles is in a forward (to the left) and downward direction. In addition, it can be seen from Figures 3.8b, 3.8e and 3.8f that the particle displacements near the edges of the chamber are constrained, and therefore soil improvement is compromised, as one might expect.

In order to investigate the relationship between soil movements, porosities and the motion of the roller, the porosities measured by measurement spheres (M1 to M12), with respect to the time and motion of the 5.46 kg module travelling at 299 mm/s in Figure 3.8, are presented in Figure 3.9 for the first pass. The porosities are presented within each of the

measurement spheres, and in parentheses, the incremental changes in porosity from the previous time step are also included. It is worth noting that the average particle diameter is 8 mm and each measurement sphere contains approximately 110 particles, which means that the porosity obtained from each measurement sphere is based on 0.27% of the total number of particles. As a result, there will inevitably be some fluctuations due to the necessary but limited size of the measurement spheres. At t = 0.2 s (Figure 3.9b), the module impacts the soil located to the right of measurement sphere M6. It can be observed from the velocity vectors that the soil located to the right of M6 moves to the left and downwards (Figure 3.8b), which results in the number of soil particles within M6 and M12 to increase, and, as a consequence, the porosities to decrease. As the module strikes the soil between M4 and M5 at t = 0.4 s (Figure 3.9c), the soil behind the module displaces upwards and to the right (Figure 3.8c), which results in the number of particles within M5 increases, and hence the porosity decreases. The porosities of M3 and M4 increase significantly since the soil located at M3 and M4 moves to the left. The particles located near M10 are pushed towards M9, therefore, the porosities within M10 and M9 increase and decrease, respectively. When the module impacts the soil located between M3 and M4 (t = 0.6 s, Figure 3.9d), the soil near M3 and M4 is compacted and the porosities of M3 and M4 reduce to 0.53 and 0.54, respectively. The porosities of M1 and M2 increase since the soil located at these areas displaces upwards. Because the module travels away from the areas of M5, M6, M11 and M12, the porosities within these spheres remain constant. Again, the porosity of M1 shows an increasing trend since the soil located in this area moves upwards when the module strikes the soil at M2 (t = 0.8 s, Figure 3.9e). The soil near M2 displaces downwards at t = 0.8 s, which results in the porosity at M2 to decrease. When t = 1.0 s (Figure 3.9f), the soil near M1 is compacted and settles, therefore, the porosity of M1 decreases. A small portion of the soil located near M7 displaces to M8,

which results in the porosities of M7 and M8 to increase and diminish, respectively. Finally, Figure 3.9g shows the porosities after the first pass of the 5.46 kg module.

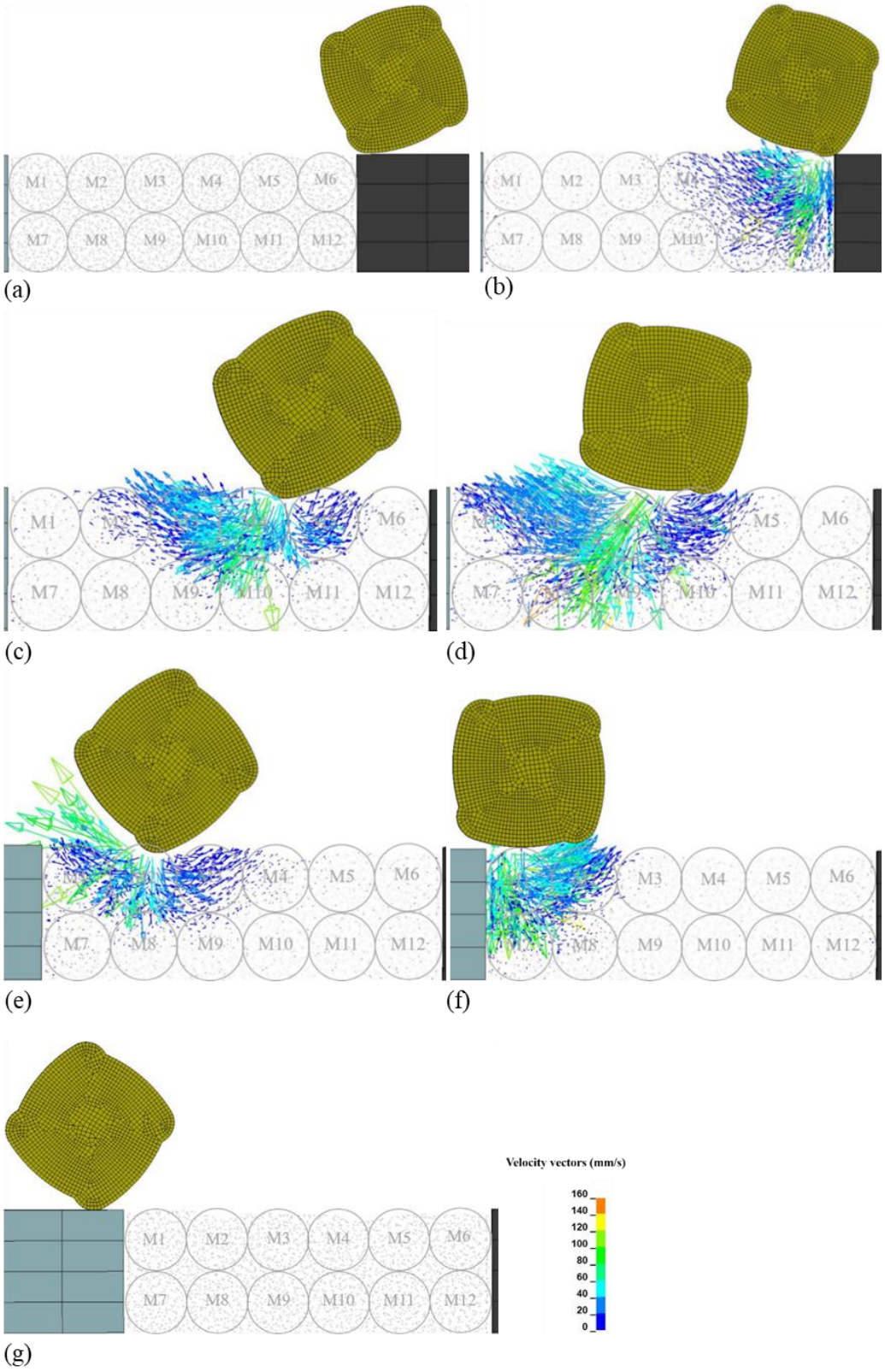

Figure 3.8: Velocity vectors of the soil relative to the motion of the 5.46 kg module at different times: (a) t = 0 s, (b) t = 0.2 s, (c) t = 0.4 s, (d) t = 0.6 s, (e) t = 0.8 s, (f) t = 1.0 s, (g) t = 1.2 s.

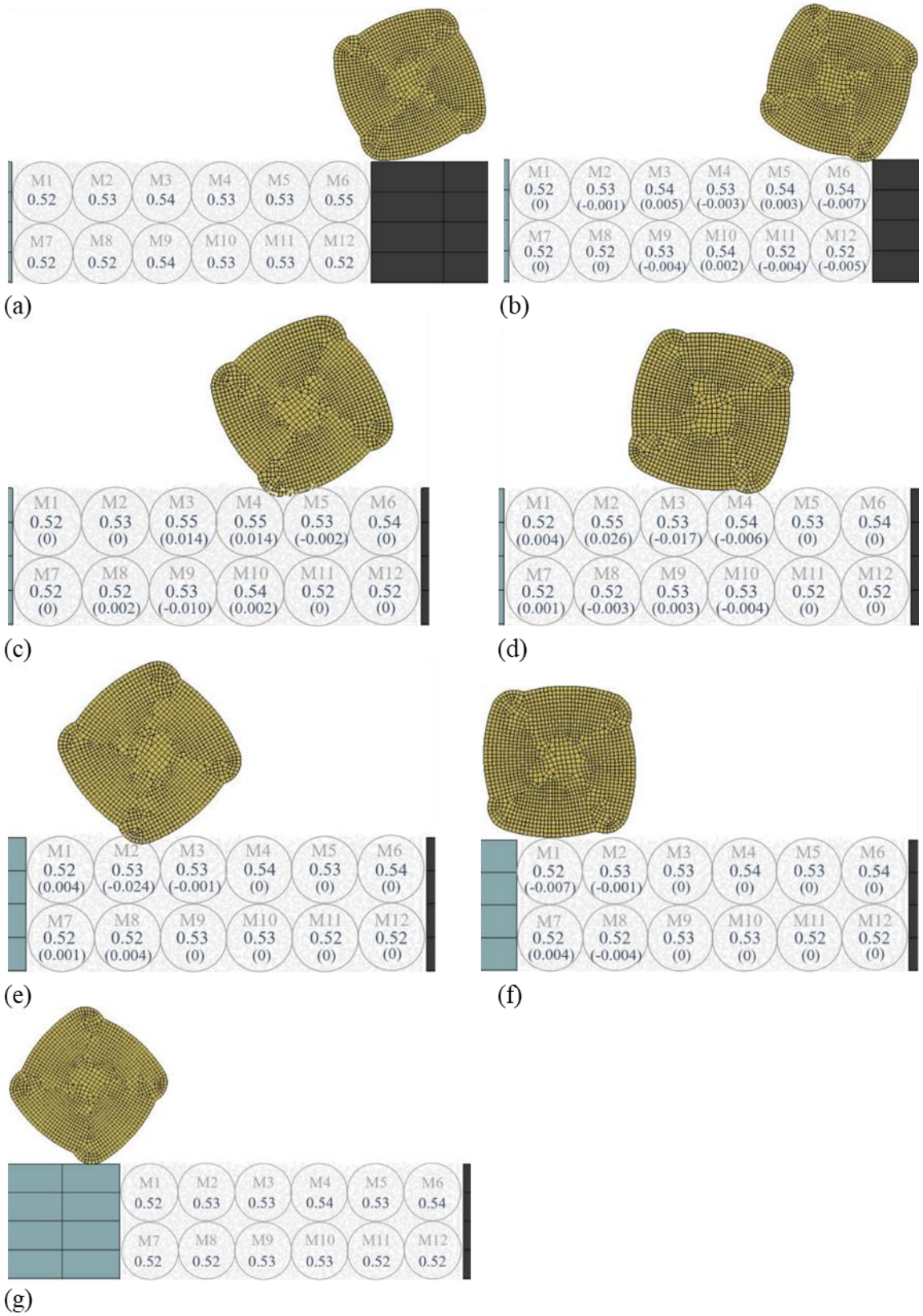

Figure 3.9: Soil porosities relative to the motion of the 5.46 kg module at different times: (a) t = 0 s, (b) t = 0.2 s, (c) t = 0.4 s, (d) t = 0.6 s, (e) t = 0.8 s, (f) t = 1.0 s, (g) t = 1.2 s.
The incremental change in porosity from the previous time step is given in parentheses.

To understand better soil porosity change with respect to the motion of the module, soil porosities recorded by various measurement spheres are plotted against time. Figure 3.10 presents the variation of porosities with respect to the time and motion of the 5.46 kg module travelling at 299 mm/s in Figures 3.8 and 3.9. The origin of the horizontal axis (time) in Figure 3.10 is set at the right-hand-side of the plot to maintain consistency with the module's direction of travel. In general, it can be seen clearly that the measured porosities change significantly with the motion of the roller. When the porosities measured by M1–M6 are compared with those recorded by M7–M12, a greater variation of porosities is observed with the former since the compactive energy imparted by the module dissipates with depth, and hence, soil located at deeper depths is less influenced by the roller. The increase of porosities, such as those measured by M3 and M4 at 0.2–0.4 s, M2 at 0.4–0.6 s and M1 at 0.4–0.8 s, is due mainly to the soil being pushed and displaced along with the motion of the roller. The reduction in porosity is due to the soil located within these areas being compacted by the module. The porosities at t = 1.2 s show that after the first pass of the 5.46 kg module, the porosities at M2 and M6 decrease slightly and the porosities at M1, M3, M4 and M5 increase, since most of the soil particles located at the ground surface are compacted and displace downwards. In addition, the porosities measured by M8–M12 decrease significantly, which also indicate that the soil displaces downwards. As indicated by the velocity vectors and porosity changes, the compaction effects are limited to the soil located at relatively shallow depths, which is consistent with that reported by Chen et al. (2021).

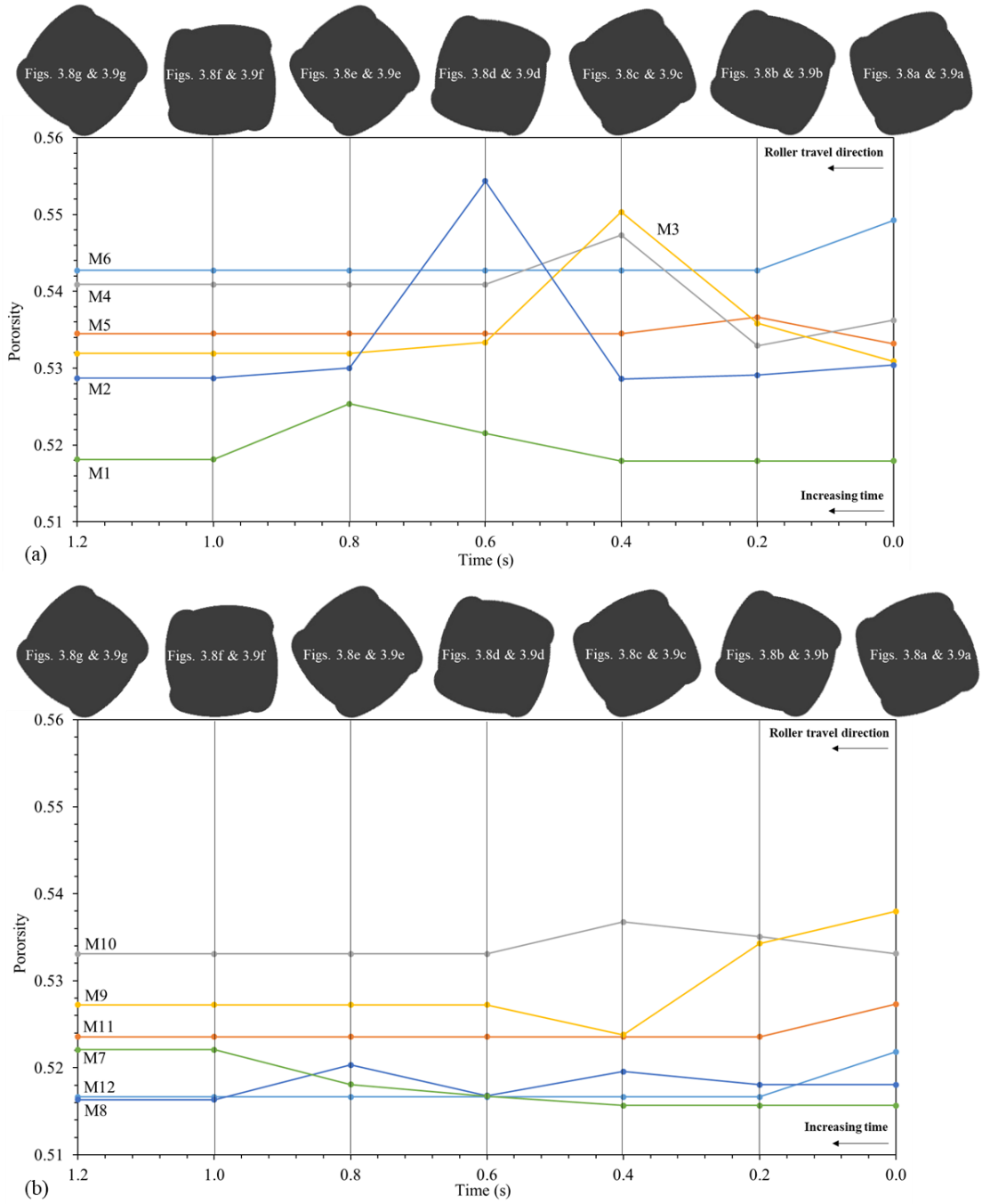

Figure 3.10: Porosities measured by measurement spheres located at: (a) 25 mm depth below the ground, (b) 75 mm depth below the ground.

3.4.3 Optimum number of passes

In their laboratory study, Chen et al. (2021) determined the optimum number of passes by assessing the averaged vertical incremental displacements caused by the module. In this paper, however, the optimum number of passes is examined using the changes in porosity of the soil located within the central region of the chamber beneath the module with respect to the number of passes. Variations of porosity with respect to the number

of passes of the 3.64 and 5.46 kg modules are shown in Figure 3.11. Additional measurement spheres were placed within the module compaction region to obtain higher resolutions of the porosity results. In general, the porosity decreases with increasing numbers of passes below 50 mm depth and the porosity increases with the number of passes above 50 mm depth. It can be seen that, for both the 3.64 and 5.46 kg modules, the most significant porosity changes occur within the first 30 passes, beyond which, the porosity change is modest. It can be observed from Figure 3.11 that, the maximum porosity changes occur above 150 mm depth.

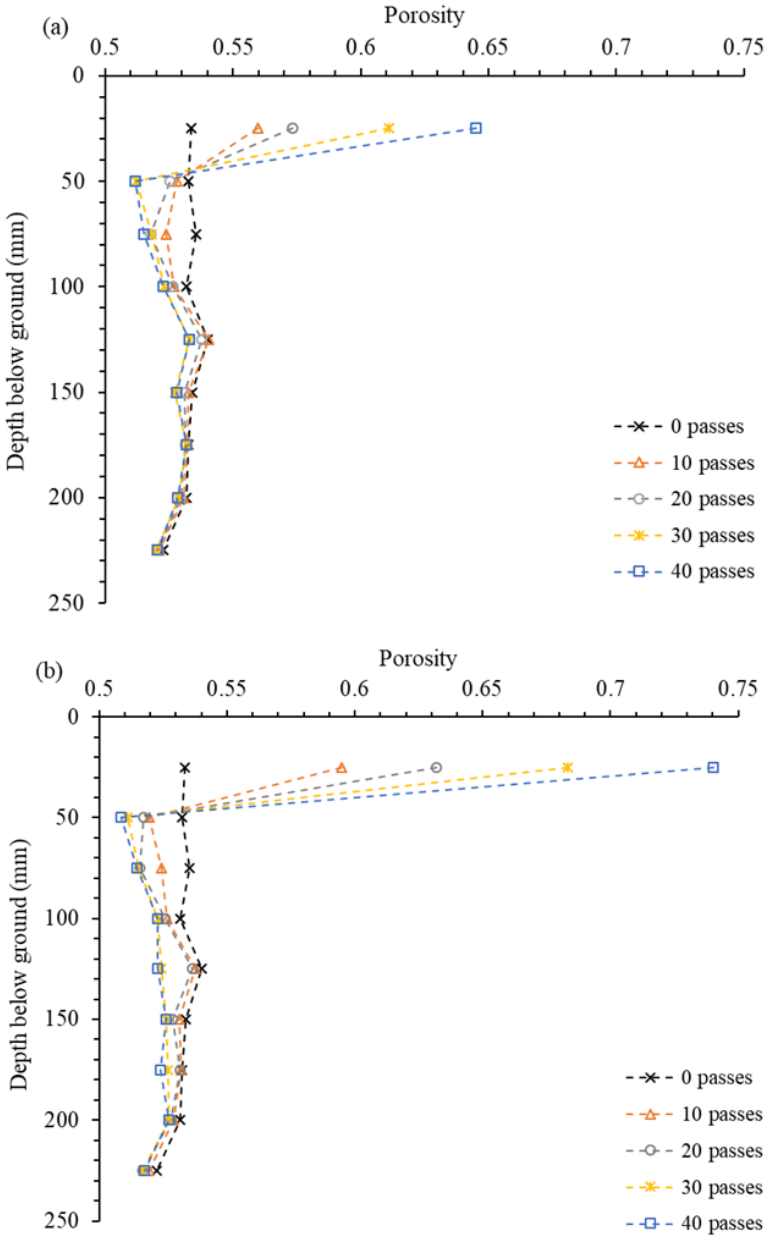

Figure 3.11: Porosity changes with number of passes for: (a) 3.64 kg module, (b) 5.46 kg module.

In Figure 3.12, the average porosities recorded by the measurement spheres located at 50–100 (M9, M10, M39 and M40) and 100–150 (M15, M16, M45 and M46) mm depths are plotted against the number of passes. The average porosity in the depth range of 0–50 mm is not included in Figure 3.12. This is because the top surface undergoes disturbance by the roller module and as expected, the porosity between 0–50 mm increases throughout the 40 passes. It was suggested by Scott et al. (2016) that, subsequent to RDC, the ground surface is always compacted by a conventional circular roller due to this disturbance and the undulating surface left by the impact roller.

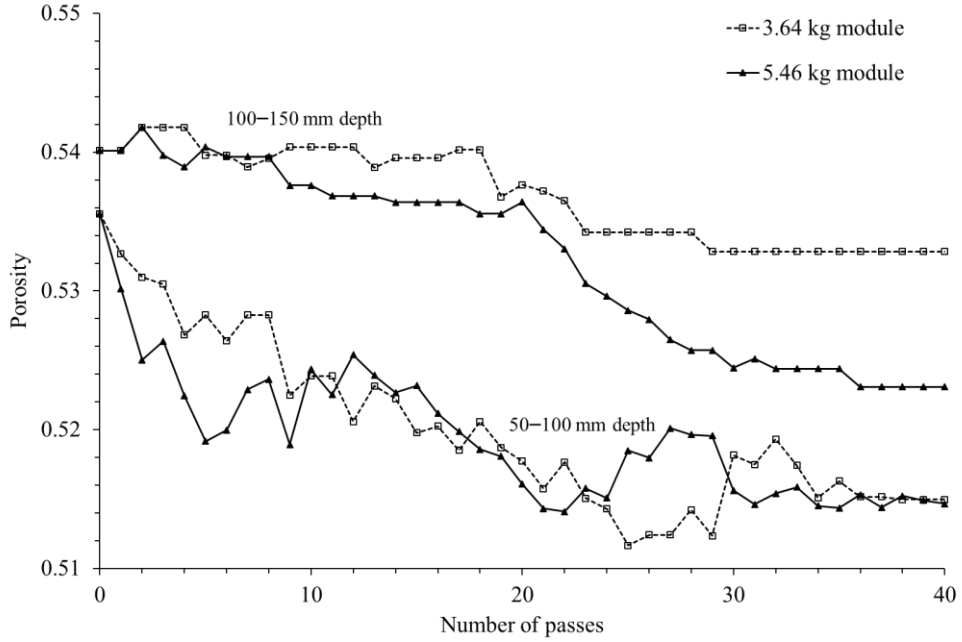

Figure 3.12: Porosity changes at 50–100 and 100–150 mm depths for 3.64 and 5.46 kg modules.

It can be seen from Figure 3.12 that, as expected, the porosity at greater depths (100–150 mm) are less affected by the module, given that the compactive energy dissipates with depth. In general, there is no significant porosity change after 35 passes between 50–100 mm depth and no obvious porosity change after 30 passes below 100 mm depth, for the 3.64 kg module travelling at speed of 299 mm/s. Therefore, the optimum number of passes is around 35 passes for the 3.64 kg module and the soil characteristics examined. For the 5.46 kg module, porosity changes exhibit similar trends to those caused by the

3.64 kg module. Porosity between 50 and 100 mm exhibits no significant change after 35 passes and porosity below 100 mm shows no obvious change after approximately 30 passes. As a consequence, it can be concluded that, for the 5.46 kg module, the optimum number of passes is also around 35 passes for the soil located below 50 mm depth, for the soil type examined.

3.4.4 Effect of module weight

In this study, the effect of the module's weight on ground improvement is examined by quantifying the porosity changes after 40 module passes. Table 3.4 presents the average porosity changes recorded by the measurement spheres located at G3, G4, G9 and G10 after 40 passes of both the 3.64 and 5.46 kg modules, respectively. It is noted that the leftmost column in Table 3.4 represents the locations of the centre points of the measurement spheres. For example, the depth of 75 mm refers to the centre point of the measurement spheres being 75 mm beneath the ground surface and, these spheres measure the soil porosity between 50 and 100 mm below the ground. In general, the 5.46 kg module results in greater porosity changes when compared with 3.64 kg module. Porosities increase near the ground surface and decrease within the soil at greater depth. As is normal with RDC, the soil near the ground surface decreases in density (i.e. increases in porosity) as a result of the characteristics of the motion of the module (Scott et al., 2016). The maximum porosity reduction of the soil occurs at a depth between 50 and 100 mm. At greater depths (e.g. 150–200 mm), the porosity decreases less markedly. The porosity is almost unchanged at the base of the chamber during the test, which indicates that the soil at the base is less affected by the module, as one would expect. This conclusion is consistent with that obtained using the PIV technique as reported by Chen et al. (2021). The results presented in Table 3.4 show that the 5.46 kg (i.e. 12-tonne

prototype) module increases the soil density to a greater extent than the 3.64 kg (i.e. 8-tonne prototype) module.

Table 3.4: The percentage porosity changes after 40 passes of the 3.64 and 5.46 kg modules, respectively.

Depth (mm)	3.64 kg module	5.46 kg module
25	20.91%	38.71%
75	–3.84%	–3.90%
125	–1.35%	–3.15%
175	–0.18%	–1.62%
225	–0.42%	–0.95%

In order to compare the efficiency of the 3.64 and 5.46 kg modules further, the relative densities of the soil, with respect to the number of passes, are plotted for both modules travelling at a speed of 299 mm/s. Rather than porosity, changes in relative density of the soil, before and after compaction, are generally adopted in geotechnical engineering as an effective indicator of the effectiveness of compaction, since relative density is a measure of soil compactness. According to Salot et al. (2009), in the numerical model, the maximum void ratio is obtained by pluviating particles under gravity. The minimum void ratio is obtained by pluviating particles in successive layers from the same approximate height of 350 mm, and a rigid plate is used to compact each layer to facilitate the densest arrangement of particles. The maximum and minimum void ratios of the numerical assembly are 0.853 and 0.632, respectively. Therefore, the relative densities of the soil between 100–150 mm depth are calculated based on the porosity changes, and are plotted in Figure 3.13. This depth range is selected as it provides the greatest difference between these two modules. It can be observed that the post-compaction relative densities are greater than the pre-compaction relative densities for both the 3.64

and 5.46 kg modules, as one would expect. The 5.46 kg module results in greater soil density after the first 8 passes and the maximum relative densities are 72.9 and 60% for the 3.64 and 5.46 kg modules, respectively. As evidenced from the figure, fewer numbers of passes are needed when the heavier module is used. As a result, due to its heavier weight, the 5.46 kg module is more effective, and hence more efficient, than the 3.64 kg module.

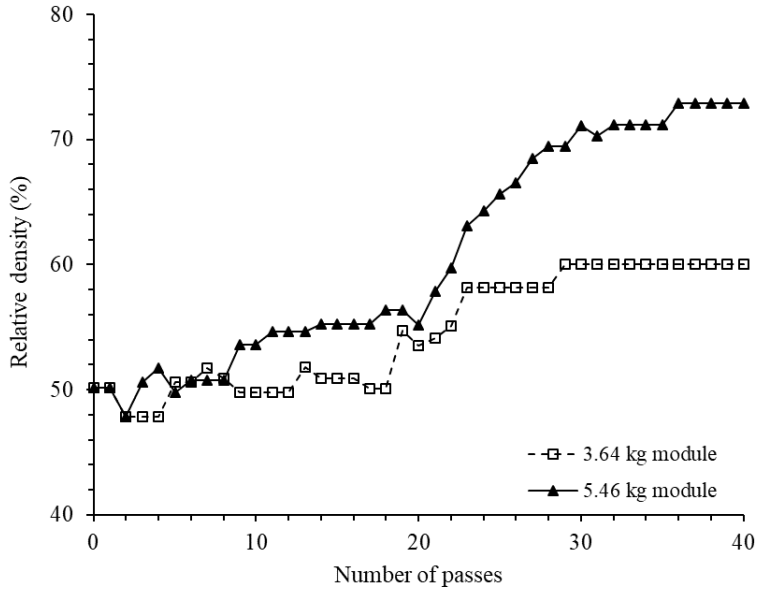

Figure 3.13: Relative densities of soil at 100–150 mm depth with respect to number of passes for 3.64 and 5.46 kg modules operated at a speed of 299 mm/s.

As described by Duncan and Seed (1986), soil compaction is treated as a loading and unloading process, which results in a significant increase of horizontal stress within the soil. The increase in horizontal stress after compaction is important for geotechnical design since it can be directly related to an increase in soil stiffness (Massarsch and Fellenius, 2020). In addition, according to Massarsch and Fellenius (2020), ground settlement is often adopted as the criterion for the specification of soil compaction projects and the input parameters for analytical methods, such as compression modulus and preconsolidation stress, which are used to predict ground settlement after compaction. However, the increase in soil preconsolidation stress is often neglected by the designer

and this can often result in excessive compaction requirements and overestimated costs. As a result, the horizontal stresses recorded by the groups of measurement spheres located at G3, G4, G9 and G10 induced by the 3.64 and 5.46 kg modules are presented in Figure 3.14. As can be seen, the horizontal stress increases significantly with the compaction of both the 3.64 and 5.46 kg modules. The heavier module induces a greater horizontal stress, as one would expect. When the horizontal stresses after 40 passes are compared with those recorded after 20 passes, it can be seen that the rate of increase of horizontal stress diminishes with respect to the number of passes for both module weights. This is consistent with that reported by Duncan and Seed (1986). They stated that the additional compactive energy applied to the compacted soil results in a much smaller increase in soil stress compared when against that applied to the uncompacted material.

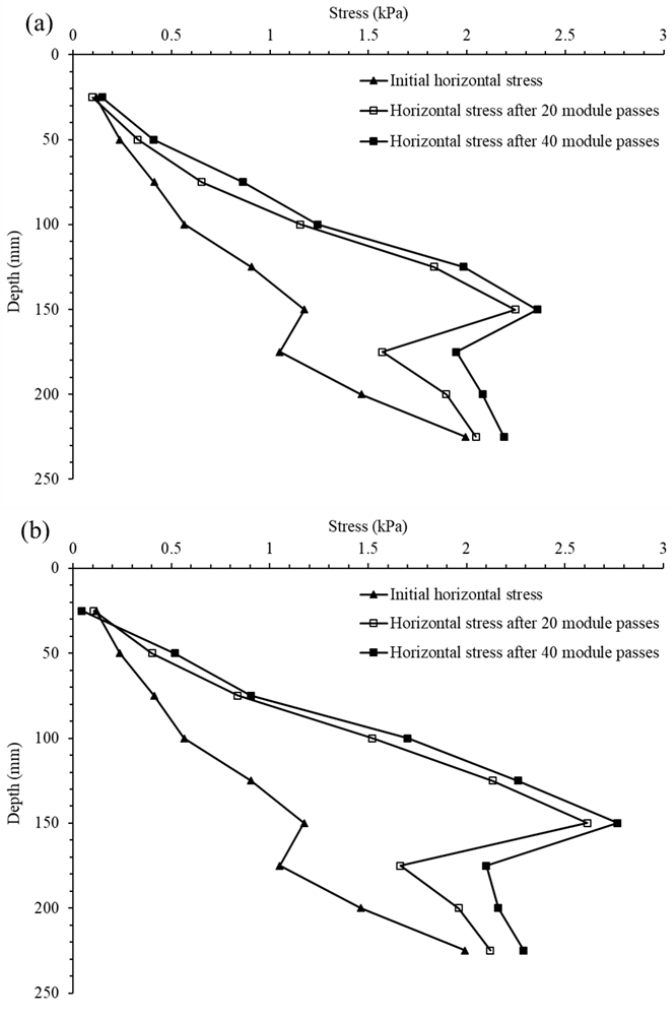

Figure 3.14: Soil horizontal stress distribution for: (a) 3.64 kg module, (b) 5.46 kg module.

3.5 Summary and Conclusions

This paper has presented a series of three-dimensional finite element method (FEM)-discrete element method (DEM) simulations to analyse the behaviour of granular materials subjected to rolling dynamic compaction (RDC) due to a 4-sided impact roller. The FEM was used to simulate the roller module, the chamber and timber frames. The soil particles, on the other hand, were simulated using the DEM. The performance of the numerical model was validated against 1:13 scale, experimental tests based on displacements of the soil particles. The results showed that the numerical model can reasonably predict soil displacements at different depths below the ground. The behaviour of granular particles impacted by the scale module can be reproduced using the FEM and the DEM. The motion of the module and the porosities were plotted at different time intervals to help understand the soil porosity and density changes with respect to the motion of the module. Based on porosity changes obtained from measurement spheres, the effectiveness of two 1:13 scale models, weighing 3.64 and 5.46 kg, which represent the 8- and 12-tonne prototypes, was examined at an operating speed of 299 mm/s, corresponding to a prototype speed of 14 km/h. The heavier module produces greater ground improvement. The most significant porosity changes occur within the first 35 passes for both the 3.64 and 5.46 kg modules. The changes of porosity decrease with depth, and beyond around 200 mm depth below the ground surface, the porosity changes are negligible. Overall, the results of this study help to understand better the behaviour of the module on granular soils. However, inferences obtained in this study are based on the results of a single soil type. Future work needs to be implemented to assess the effectiveness of the scaled module in a variety of soil types and ground conditions.

3.6 Acknowledgements

The authors wish to acknowledge the computational resources provided by the Phoenix HPC service at the University of Adelaide.

3.7 Declarations

3.7.1 Funding

This study was funded by Adelaide Graduate Research Scholarship.

3.8 Compliance with ethical standards

3.8.1 Conflict of interest

The authors declare that they have no conflict of interest.

3.9 References

Altaee, A., Fellenius, B. H. 1994. Physical modeling in sand. Canadian Geotechnical Journal, **31**(3): 420-431.

Antypov, D., Elliott, J. 2011. On an analytical solution for the damped Hertzian spring. EPL (Europhysics Letters), 94, 50004.

Avalle, D., Carter, J. 2005. Evaluating the improvement from impact rolling on sand. Proc. 6th Int. Conf. on Ground Improvement Techniques, Coimbra, Portugal, pp. 8.

Bian, X., Nan, C., Xiao, F., Zhou, Z., Wang, Z. 2002. FEM analysis of impaction effect for non-column wheels of compacting roller. Chinese Journal of Mechanical Engineering, p. 10.

Bradley, A. C., Jaksa, M. B., Kuo, Y.-L. 2019. Examining the kinematics and energy of the four-sided impact roller. Proceedings of the Institution of Civil Engineers - Ground Improvement, 172, pp. 297-304.

Calvetti, F., Di Prisco, C., Nova, R. 2004. Experimental and numerical analysis of soil–pipe interaction. Journal of geotechnical and geoenvironmental engineering, 130, pp. 1292-1299.

Calvetti, F., Viggiani, G., Tamagnini, C. 2003. A numerical investigation of the incremental behavior of granular soils. Rivista italiana di geotecnica, 37, pp. 11-29.

Chen, Y., Deng, A., Wang, A., Sun, H. 2018. Performance of screw–shaft pile in sand: Model test and DEM simulation. Computers and Geotechnics, 104, pp. 118-130.

Chen, Y., Jaksa, M., Kuo, Y., Airey, D. 2021. Experimental Analysis of Rolling Dynamic Compaction Using Transparent Soils and Particle Image Velocimetry. Canadian Geotechnical Journal. Available from http://dx.doi.org/10.1139/cgj-2020-0573.

Chou, H., Lee, C., Chung, Y., Hsiau, S. 2012. Discrete element modelling and experimental validation for the falling process of dry granular steps. Powder technology, 231, pp. 122-134.

Chung, O., Scott, B., Jaksa, M., Kuo, Y., Airey, D. 2017. Physical modeling of rolling dynamic compaction. Proceedings of the 19th Int. Conf. on Soil Mechanics and Geotechnical Engineering, Seoul, Korea, Sept. 18–22, pp. 905–908.

Ciantia, M., Arroyo Alvarez De Toledo, M., Calvetti, F., Gens Solé, A. 2015. An approach to enhance efficiency of DEM modelling of soils with crushable grains. Géotechnique, 65, pp. 91-110.

Ciantia, M. O., Arroyo, M., Butlanska, J., Gens, A. 2016. DEM modelling of cone penetration tests in a double-porosity crushable granular material. Computers and Geotechnics, 73, pp. 109-127.

Coetzee, C. J. 2017. Review: Calibration of the discrete element method. Powder Technology, 310, pp. 104-142.

Cundall, P. A., Strack, O. D. 1979. A discrete numerical model for granular assemblies. geotechnique, 29, pp. 47-65.

Da Cruz, F., Emam, S., Prochnow, M., Roux, J.-N., Chevoir, F. 2005. Rheophysics of dense granular materials: Discrete simulation of plane shear flows. Physical Review E, 72, 021309.

Duncan, J. M., Seed, R. B. 1986. Compaction-induced earth pressures under K 0-conditions. Journal of Geotechnical Engineering, 112, pp. 1-22.

Evans, T. M., Valdes, J. R. 2011. The microstructure of particulate mixtures in one-dimensional compression: numerical studies. Granular Matter, 13, pp. 657-669.

Farsi, A., Xiang, J., Latham, J., Pullen, A., Carlsson, M., Stitt, E., Marigo, M. 2015. An application of the finite-discrete element method in the simulation of ceramic breakage: methodology for a validation study for alumina specimens. In PARTICLES IV: proceedings of the IV International Conference on Particle-Based Methods: fundamentals and applications, pp. 921-932.

Feng, Y., Owen, D. 2014. Discrete element modelling of large scale particle systems—I: exact scaling laws. Computational Particle Mechanics, 1, pp. 159-168.

Forsström, D., Jonsén, P. 2016. Calibration and validation of a large scale abrasive wear model by coupling DEM-FEM: Local failure prediction from abrasive wear of tipper bodies during unloading of granular material. Engineering Failure Analysis, 66, pp. 274-283.

Gabrieli, F., Cola, S., Calvetti, F. 2009. Use of an up-scaled DEM model for analysing the behaviour of a shallow foundation on a model slope. Geomechanics and Geoengineering: An International Journal, 4, pp. 109-122.

González-Montellano, C., Fuentes, J., Ayuga-Téllez, E., Ayuga, F. 2012. Determination of the mechanical properties of maize grains and olives required for use in DEM simulations. Journal of Food Engineering, 111, pp. 553-562.

Gu, M., Han, J., Zhao, M. 2017. Three-dimensional discrete-element method analysis of stresses and deformations of a single geogrid-encased stone column. International Journal of Geomechanics, 17, 04017070.

Huang, M., Chen, Y., Gu, X. 2019. Discrete element modeling of soil-structure interface behavior under cyclic loading. Computers and Geotechnics, 107, pp. 14-24.

Imre, B., Räbsamen, S., Springman, S. M. 2008. A coefficient of restitution of rock materials. Computers & Geosciences, 34, pp. 339-350.

Jaksa, M. B., Scott, B. T., Mentha, N., Symons, A., Pointon, S., Wrightson, P., Syamsuddin, E. 2012. Quantifying the zone of influence of the impact roller. ISSMGE-TC 211 International Symposium on Ground Improvement IS-GI Brussels, Belgium, 30 May – 1 June, Vol. 2, pp. 41–52.

Jiang, M., Dai, Y., Cui, L., Shen, Z., Wang, X. 2014. Investigating mechanism of inclined CPT in granular ground using DEM. Granular Matter, 16, pp. 785-796.

Kozicki, J., Tejchman, J., Mühlhaus, H. B. 2014. Discrete simulations of a triaxial compression test for sand by DEM. International Journal for Numerical and Analytical Methods in Geomechanics, 38, pp. 1923-1952.

Kuo, Y., Jaksa, M., Scott, B., Bradley, A., Power, C., Crisp, A., Jiang, J. 2013. Assessing the effectiveness of rolling dynamic compaction. Proceedings of the 18th International Conference on Soil Mechanics and Geotechnical Engineering, Paris., vol. 2, pp. 1309–1312.

Li, L., Wu, W., El Naggar, M. H., Mei, G., Liang, R. 2019. DEM analysis of the sand plug behavior during the installation process of open-ended pile. Computers and Geotechnics, 109, pp. 23-33.

Lstc. 2018. LS-DYNA KEYWORD USER'S MANUAL. Livermore, California: Livermore Software Technology Corporation, ISBN: 0-9778540-2-7.

Mahabadi, O., Lisjak, A., Grasselli, G., Lukas, T., Munjiza, A. 2010. Numerical modelling of a triaxial test of homogeneous rocks using the combined finite-discrete element method. Proc. European Rock Mechanics Symp.(EUROCK2010), Lausanne, Switzerland, pp. 173-176.

Massarsch, K., Fellenius, B. 2020. Deep Compaction of Sand Causing Horizontal Stress Change. Geotechnical Engineering Journal of the SEAGS and AGSSEA, **51**(2), pp. 9-21.

Nandanwar, M. 2015. Measurement and simulation of triaxial compression tests for a sandy loam soil.

Pinard, M. 1999. Innovative developments in compaction technology using high energy impact compactors. *In* Proceedings 8th Australia New Zealand Conference on Geomechanics: Consolidating Knowledge. Australian Geomechanics Society, pp. 775-781.

Rajarathnam, P., Masoudian, M. S., Airey, D. W., Jaksa, M. B. 2016. Model tests of rolling dynamic compaction. *In* Proc. 19th Southeast Asian Geotechnical Conf. and 2nd AGSSEA Conf., Kuala Lumpur, May 31 – June 3. pp. 505–510.

Sadek, M. A., Chen, Y. 2014. Microproperties calibration of discrete element models for soil-tool interaction. Montreal, Quebec Canada July 13–July 16, American Society of Agricultural and Biological Engineers, 1.

Salot, C., Gotteland, P., Villard, P. 2009. Influence of relative density on granular materials behavior: DEM simulations of triaxial tests. Granular matter, 11, pp. 221-236.

Scott, B., Jaksa, M. 2014. Evaluating rolling dynamic compaction of fill using CPT. Proceedings of the 3rd International Symposium on Cone Penetration Testing, pp. 941-948.

Scott, B., Jaksa, M., Syamsuddin, E. 2016. Verification of an impact rolling compaction trial using various in situ testing methods. *In* Proc. of 5th Int. Conf. on Geotechnical and Geophysical Site Characterisation, Gold Coast, Australia., pp. 735-740.

Tatsuoka, F., Goto, S., Tanaka, T., Tani, K. and Kimura, Y. 1997. Particle size effects on bearing capacity of footing on granular material. Deformation and progressive failure in geomechanics, pp.133-138.

Wang, C., Deng, A., Taheri, A. 2018. Three-dimensional discrete element modeling of direct shear test for granular rubber–sand. Computers and Geotechnics, 97, pp. 204-216.

Wang, Y.-H., Leung, S.-C. 2008. A particulate-scale investigation of cemented sand behavior. Canadian Geotechnical Journal, 45, pp. 29-44.

Wu, K., Sun, W., Liu, S., Zhang, X. 2021. Study of shear behavior of granular materials by 3D DEM simulation of the triaxial test in the membrane boundary condition. Advanced Powder Technology. **32**(4), pp.1145-1156.

Xu, W., Zeng, H., Yang, P., Zang, M. 2020. Numerical analysis on tractive performance of off-road tire on gravel road using a calibrated finite element method–discrete element method model and experimental validation. Proceedings of the Institution of Mechanical Engineers, Part D: Journal of Automobile Engineering, 234, pp. 3440-3457.

Yang, B., Jiao, Y., Lei, S. 2006. A study on the effects of microparameters on macroproperties for specimens created by bonded particles. Engineering Computations, 23, pp. 607-631.

Zhang, A., Jiang, M., Thornton, C. 2020. A coupled CFD-DEM method with moving mesh for simulating undrained triaxial tests on granular soils. Granular Matter, 22, pp. 1-13.

Zhou, W., Ma, X., Ng, T.-T., Ma, G., Li, S.-L. 2016. Numerical and experimental verification of a damping model used in DEM. Granular Matter, 18, 1.

Chapter 4.

Discrete element modelling of the 4-sided impact roller

Statement of Authorship

Title of Paper	Discrete element modelling of the 4-sided impact roller
Publication Status	☑ Published ☐ Accepted for Publication ☐ Submitted for Publication ☐ Unpublished and Unsubmitted w ork w ritten in manuscript style
Publication Details	Chen, Y., Jaksa, M., Kuo, Y., Scott, B. 2021. Discrete element modelling of the 4-sided impact roller. Computers and Geotechnics, Available from https://doi.org/10.1016/j.compgeo.2021.104250.

Principal Author

Name of Principal Author (Candidate)	Yue Chen
Contribution to the Paper	Developed the numerical model, contributed to methodology, analysis and interpretation of the data, wrote manuscript.
Overall percentage (%)	80%
Certification:	This paper reports on original research I conducted during the period of my Higher Degree by Research candidature and is not subject to any obligations or contractual agreements with a third party that would constrain its inclusion in this thesis. I am the primary author of this paper.
Signature	Date: 08 October 2021

Co-Author Contributions

By signing the Statement of Authorship, each author certifies that:

i. the candidate's stated contribution to the publication is accurate (as detailed above);
ii. permission is granted for the candidate in include the publication in the thesis; and
iii. the sum of all co-author contributions is equal to 100% less the candidate's stated contribution.

Name of Co-Author	Mark Jaksa
Contribution to the Paper	Provided primary supervision, initial concept, contributed to the methodology, helped evaluate and edit the manuscript.
Signature	Date: 12/10/21

Name of Co-Author	Yien Lik Kuo
Contribution to the Paper	Provided secondary supervision, assisted with research direction, helped edit the manuscript.
Signature	Date: 08 Oct 2021

Please cut and paste additional co-author panels here as required.

Name of Co-Author	Brendan Scott		
Contribution to the Paper	Provided secondary supervision, contributed to the methodology, helped edit the manuscript.		
Signature		Date	12/10/2021

Please cut and paste additional co-author panels here as required.

Discrete element modelling of the 4-sided impact roller (Paper 3)

Abstract

Rolling dynamic compaction (RDC) is a ground improvement technique, which involves towing a non-circular module behind a tractor to achieve soil compaction. When compared against conventional static and vibratory compaction techniques, RDC is capable of compacting thicker layers of soil and at a faster operating speed. This study validates the developed numerical scale model against a field study using the full-size RDC module. Numerical results were compared with the field data in four aspects namely, displacements at the ground surface, and at depths of 0.7 and 1.1 m, pressures at 0.7 and 1.1 m depths, energy delivered by the RDC module into the underlying soil, and the depth of improvement. It is concluded that, numerical results are in good agreement with the field data. This paper also proposes that pressure results are an imperfect indicator to assess the optimum number of RDC passes, whereas, ground settlement is recommended since it better reflects ground improvement due to RDC and it has a clear relationship with the number of passes.

4.1 Introduction

It goes without saying that, for those who knew Prof. Scott Sloan, appreciated his great fondness for and his significant expertise in numerical modelling. This paper is offered humbly in honour of that great man, who continues to be deeply missed.

Soil compaction is a process where air voids within the soil body are removed and the density of the soil is increased by the application of mechanical energy. As a result, ground performance is improved with, for example, increased bearing capacity, enhanced strength, and reduced settlements and permeability (Ranjan and Rao 2007). Rolling dynamic compaction (RDC) is a ground improvement technique which has gained

increased popularity over the past few decades. It involves towing a non-circular module, which imparts energy as it falls to impact the ground. Both potential and kinetic energies are imparted into the ground simultaneously by RDC which, when compared with conventional smooth drum rollers, enables the ground to be compacted to a greater depth and with improved efficiency due to its relatively fast operating speed. RDC has been applied in several large and open ground improvement projects in the civil and mining sectors, land reclamation projects, and highway rehabilitation (Avalle and Carter 2005; Avalle and McKenzie 2005; Bouazza and Avalle 2006).

Previous researchers have conducted field tests to assess the effectiveness of RDC (Avalle and Carter 2005; Jaksa et al. 2012; Scott and Jaksa 2014; Scott et al. 2019a, 2019b, 2020). As conducting field tests with the full-size RDC module is somewhat costly and time-consuming, and results obtained from such field testing contain some uncertainties due to the difficulty of controlling and measuring many aspects affecting the efficacy of RDC in the field. As a consequence, a 1:13 small-scale physical RDC model was investigated to assess the effectiveness of RDC in a controlled laboratory environment. Chung et al. (2017) confirmed that the small-scale model produced similar compaction results to those from the full-size model, based on the scaling laws proposed by Altaee and Fellenius (1994). Although conducting small-scale model tests is more cost effective than undertaking field tests, small-scale tests still require significant time, care and specialised equipment to prepare and undertake such testing. Therefore, numerical models have been developed by several researchers (Kuo et al. 2013; Bradley et al. 2019) to assess the effectiveness of RDC. Kuo et al. (2013) and Bradley et al. (2019) investigated the behaviour of a full-size RDC model using the finite element method (FEM) as incorporated in the LS-DYNA computer application (LSTC 2018). The FEM model was validated against field results and it showed encouraging results in terms of simulating

ground responses induced by RDC. However, one of the main disadvantages of the FEM model, due to its continuum rather than particulate nature, is that the motion of soil particles is difficult to simulate. To overcome the limitations of the FEM, the discrete element method (DEM) has been adopted by several researchers to simulate the behaviour of granular materials (Jiang et al. 2014; Chen et al. 2018; Jing et al. 2018). In the DEM, particle displacements are tracked at each time step, which provides detailed information of soil movements at the particle scale. Since the FEM has been successfully used to model the behaviour of RDC (Kuo et al. 2013; Bradley et al. 2019), but it is unable to simulate non-continuum mechanics within a soil body influenced by RDC, and the DEM is able to model particle movements and interactions, but it is difficult to simulate the behaviour of RDC. The FEM-DEM approach is used to simulate soil responses due to RDC in order to combine the advantages of these two methods. The RDC module is described by the FEM and the soil particles are simulated by the DEM. The FEM-DEM approach has been successfully adopted to assess the wear of a tipper using LS-DYNA (Forsström and Jonsén 2016) and to simulate tire-soil interactions (Yang et al. 2019; Xu et al. 2020; Zeng et al. 2020). These studies demonstrate the efficacy of the combined FEM-DEM approach in investigating problems related to geomechanics.

Air voids within the soil are reduced with each pass of the roller and therefore the performance of RDC is affected by the number of passes. As a result, settlement, shear strength and density of the soil increase with each pass of the RDC module, however, the rate of increase of these gradually diminishes with respect to the number of passes. Ultimately, when the number of passes reaches some critical value, settlement, shear strength and density will plateau. This is supported by Avalle and Grounds (2004) who identified a reducing rate of settlement change with increasing number of passes. The number of passes required is dependent on the type of soil, its initial density, and the

characteristics of the RDC module; i.e. its mass, shape and operating speed. The changes in the rate of ground improvement indicate the optimum number of passes needs to be determined to achieve the desired densification of soils without conducting excessive number of passes. However, the optimum number of passes varies depending on the soil type, moisture content, gradation, and layer thickness of the soil (Avsar et al. 2006). In addition, the optimum number of passes is often quantified using different indicators in field conditions. For example, Avsar et al. (2006) defined the optimum number of passes by measuring the dry density of soil, whereas Avalle and McKenzie (2005) determined the optimum number of passes by monitoring the average ground settlements, and Avalle and Carter (2005) used settlement, and the results of dynamic cone penetrometer (DCP) testing and cone penetrometer tests (CPTs). Some indicators can be measured in a cost-effective way; for example, ground settlement, and some are more time-consuming and costly; such as, DCP testing and CPTs. In order to determine the optimum number of passes, and in consideration of time, cost and feasibility, it is essential to obtain an indicator, which is not only easier to be measured, but also reflects the ground improvement induced by RDC. In current practice, the specified number of roller passes is often determined by the project engineer, since the optimum number of passes depends on the site conditions. Therefore, there is a need to obtain an efficient indicator that can be measured easily to determine the optimum number of passes of RDC under various field conditions.

This paper aims, firstly, to develop a FEM-DEM based model to simulate the behaviour of the 1:13 RDC scale model of the 4-sided, 8-tonne, Broons BH-1300 impact roller. Results of the developed numerical model are subsequently upscaled, using the Altaee and Fellenius (1994) scaling laws, and then validated against a field study that was conducted using the corresponding full-size RDC. Secondly, the results of the numerical

model are analysed, evaluated, and compared against each other in order to obtain an efficient indicator that can be used to quantify the optimum number of RDC passes.

4.2 Field testing

A field study was carried out by Scott et al. (2016) and Scott et al. (2019a; 2019b; 2020) using the full-size 4-sided, 8-tonne Broons BH-1300 impact roller at Monarto Quarries, Callington, South Australia. The field test was conducted on a trial pad which was filled with improved crushed rock quarry material, that was classified as a well-graded Sandy Gravel (GW) in accordance with the Unified Soil Classification System. The field particle size distribution curve is shown in Figure 4.1. As shown in Figure 4.2, the trial pad was 1.5 m deep and 4 m length, and two Geokon 3500 (230 mm diameter and 6 mm thick) earth pressure cells (EPCs) were placed at 0.7 and 1.1 m depths beneath the ground surface to measure pressures induced by RDC, respectively. Both EPCs were embedded at the centreline of the test lane. In addition, an accelerometer was attached to each EPC at Z plane to measure vertical acceleration. Both EPCs and accelerometers were connected to a custom-built data acquisition system and Labview software program. A sampling frequency of 4 kHz was used to ensure true peak pressures and accelerations could be captured. Acceleration-time responses were double integrated to quantify displacements at depths of 0.7 and 1.1 m beneath the ground surface. In addition, ground surface settlements were monitored by surveying local low points from each module face that contacted the ground. A total of 80 passes was conducted in the field trial, whilst maintaining a constant operating speed of 11 km/h.

One limitation of conducting field tests using buried EPCs is that it is not possible to capture the maximum pressure that the module imparts to the ground for every pass. To account for this, the distance between the centre of the module face and the centre of each

EPC, defined as the offset distance, was measured to account for the effects of non-direct impacts.

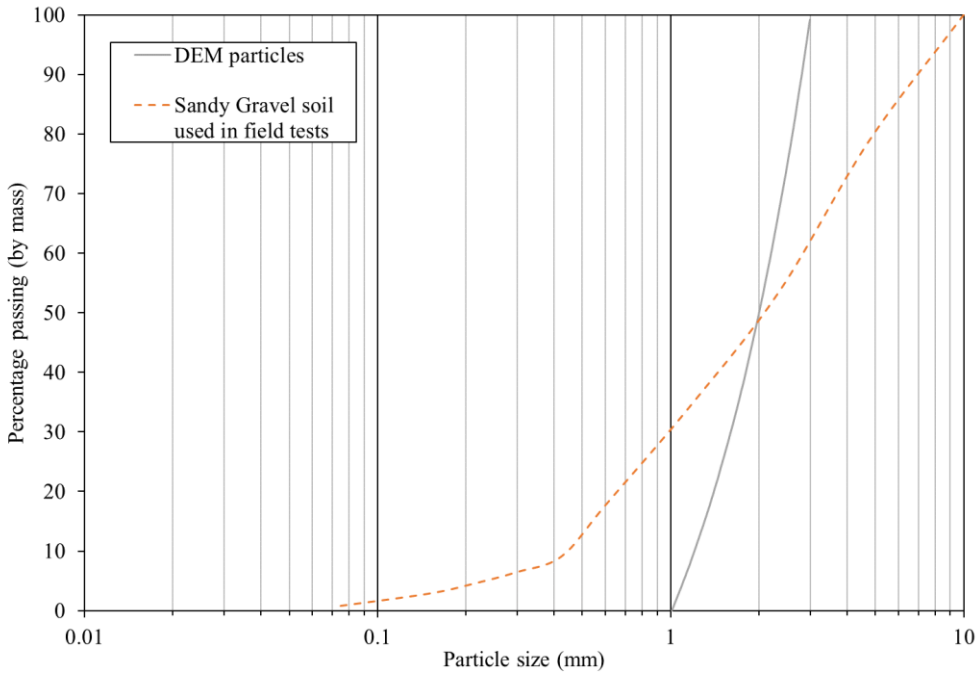

Figure 4.1: Particle size distribution curves.

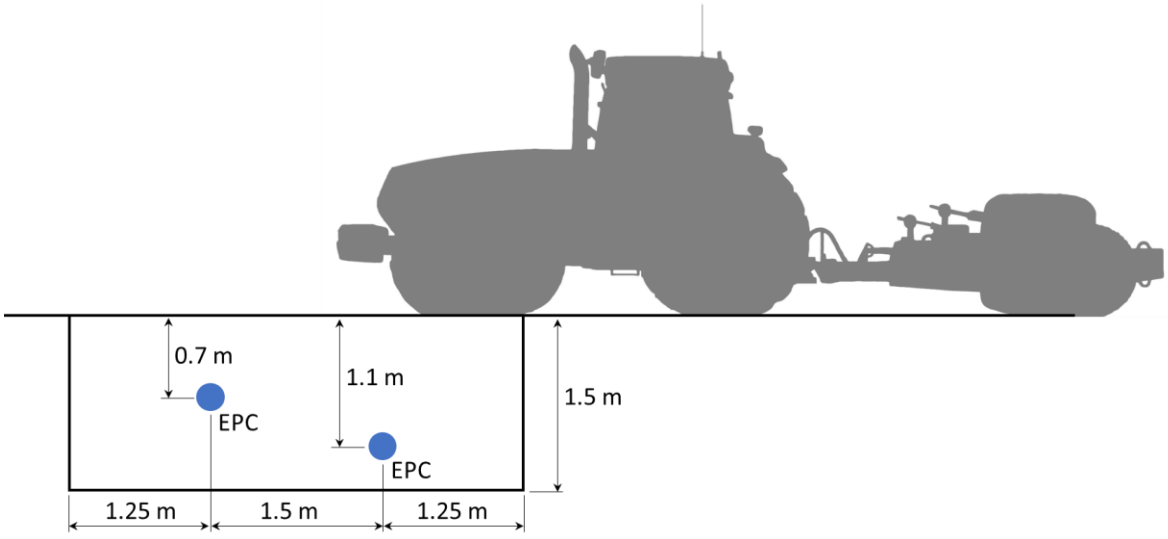

Figure 4.2: Setup of the field tests.

4.3 Numerical model development

The FEM-DEM numerical model is developed using LS-DYNA to analyse the behaviour of an impact roller model on granular materials. The 1:13 scaled RDC module, rather than the full-size module, is simulated in this study due to computational and time constraints. The full-size module requires larger soil areas to be compacted that requires a greater number of soil particles in the numerical model. This will then significantly increase the simulation running time. In the numerical model, the actual soil particles are simulated using rigid spheres with deformable contacts. The rotation of spheres is prohibited to increase the macroscopic shear strength of the numerical model (Calvetti et al. 2003). The linear contact model developed by Cundall and Strack (1979) is adopted to describe the forces between particles. As shown in Figure 4.3, the interaction between two overlapping particles is represented by two linear elastic springs in the normal and shear directions with constant stiffnesses of k_n and k_s, respectively; two viscous damping dashpots in the normal and shear directions with damping ratios of β_n and β_s, respectively; and a frictional slip in the shear direction with a coefficient of friction, μ, to limit the shear force between particles at contacts, based on Coulomb's law of friction. The interaction distance (d_{int}) between adjacent particles is defined by Equation (4.1). The contact law is active when d_{int} is less than zero. Small numerical normal and shear damping ratios (i.e. $\beta_n = \beta_s = 0.1$) are selected for the soil particles in all of the simulations, considering the value of the restitution coefficient and the simulation of the triggering of failure (Gabrieli et al. 2009).

$$d_{int} = r_1 + r_2 - |X_1 - X_2| \tag{4.1}$$

where r_1 and r_2 are the radii of two particles; and X_1 and X_2 are the coordinates of two particles.

Similar to the interaction between the particles, the interaction between finite elements and discrete particles is accommodated by a penalty-based contact algorithm, which checks each particle for penetration through the contact surface of the finite elements (LSTC 2018). If penetration is detected, the contact force is applied between the penetrating particle and the contact point of the finite elements. The magnitude of the contact force is proportional to the penetration depth. This is treated by inserting springs between the discrete particles and the contact finite elements. The stiffnesses of these springs are calculated using Equation (4.2). In the case of contact between elements with different stiffnesses, LS-DYNA adopts the lowest stiffness. If there is slide between the discrete particles and the contact finite elements, a friction force is also applied.

$$k_i = \frac{f_s \cdot A_i \cdot K_i}{V_i} \tag{4.2}$$

where k_i is the stiffness of the spring (i) placed between particles and the contact finite elements; f_s is the penalty scale factor (the default value of unity is used in this study); and A_i, V_i and K_i are the contact area, the volume and the stiffness of the contacted element, respectively.

Different from the FEM model, where the macroscopic properties of soil can be used as input parameters directly, in the DEM model, the input parameters need to be calibrated so that the numerical particles have the same macroscopic behaviour as the actual soil. Therefore, standard geotechnical tests, such as, direct shear or triaxial tests, are often undertaken to calibrate the DEM input parameters (Coetzee 2017). In this study, the DEM input parameters are calibrated against triaxial tests and then the calibrated DEM input parameters are adopted in the numerical RDC simulations. All simulations were conducted on a supercomputer (2 × Intel Xeon Gold 6248 Processor @2.4 GHz) using the ANSYS (LS-DYNA) software.

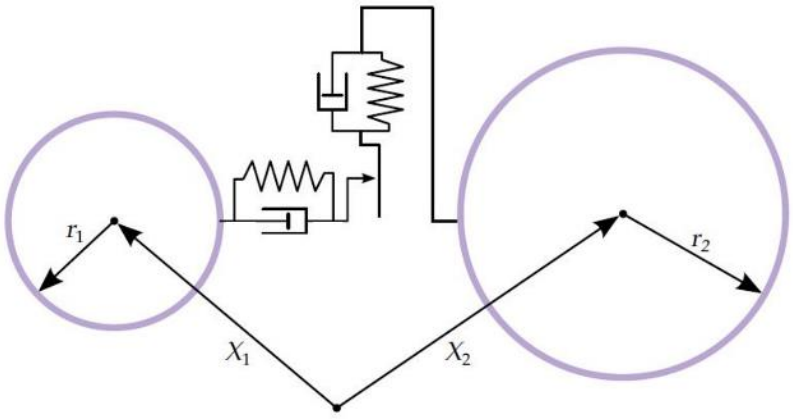

Figure 4.3: Illustration of particle-particle contact interaction (LSTC 2018).

4.3.1 Establishment of DEM input parameters

The laboratory triaxial tests under the confining pressures of 150 and 250 kPa were undertaken on Sandy Gravel soil from Monarto Quarries (as used in the field tests). The tests were drained and, hence, with no porewater pressure generated during the tests. As shown in Figure 4.1, the soil particle size range was approximately 0.1 to 10 mm, with a D_{50} value of 2 mm. In the DEM model, particles were generated by specifying minimum and maximum radii. Because of time and computational constraints, it was impossible to use the same particle sizes in the numerical simulations as those adopted in experimental tests. The selection of the maximum and minimum DEM particle sizes is limited by the total number of particles, the time step for the numerical model, the diameter of the triaxial test samples, and the dimensions of the 1:13 RDC scale model. Small particle sizes significantly increase the total number of DEM particles and decrease the numerical time step, which then increases the simulation running time. The maximum particle size is governed by the diameter of the triaxial test samples in the calibration tests and the dimensions of the RDC scale model in the numerical RDC tests (this is treated in greater detail in the following section). In addition, a wide range of particle sizes results in a greater number of particles in the model, which increases the difficulty of particle size upscaling and significantly increases the simulation running time. As a consequence, a

relatively narrow range of particle size is favoured (de Bono et al. 2015; Chen et al. 2018). Therefore, the minimum and maximum radii of the numerical particles are selected to be 0.5 and 1.5 mm, respectively, which yielded a D_{50} = 2 mm. The value of D_{50} is chosen to represent the Sandy Gravel soil used in the field tests. The particle size distribution curve of DEM particles is shown in Figure 4.1.

As shown in Figure 4.4, the numerical triaxial test model consists of two loading caps, a flexible membrane and soil particles. The numerical triaxial test sample has a diameter of 50 mm and a height of 100 mm, which are the same as those adopted in the laboratory triaxial tests. The loading caps and the flexible membrane are simulated using the FEM as rigid and rubber materials, respectively.

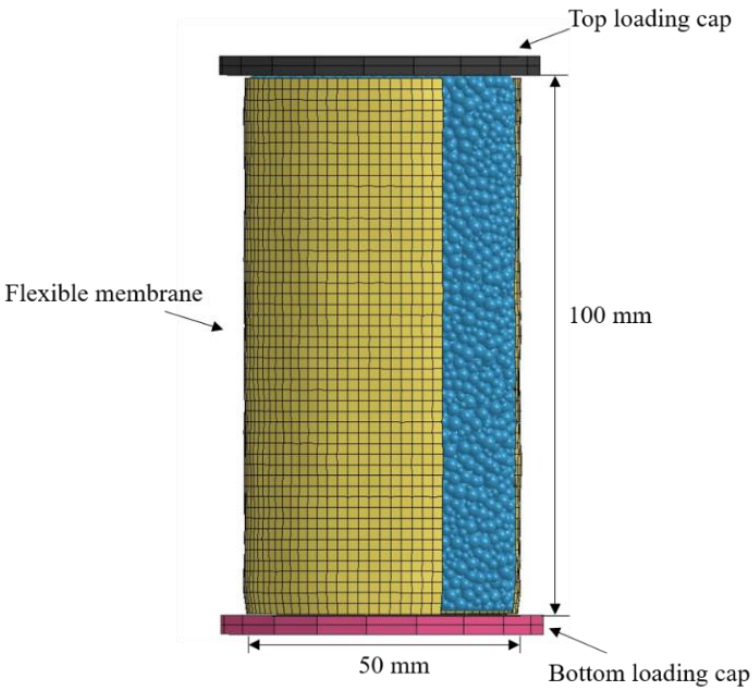

Figure 4.4: Numerical triaxial tests.

The input parameters for the loading caps are referred to Zeng et al. (2020) and are presented in Table 4.1. The material properties of the membrane are defined by inputting

the stress-strain curve obtained from uniaxial tension experiments reported by Thakur and Penumadu (2020) into the numerical model. The friction coefficient between the particles and the membrane, and between the particles and the loading caps are obtained from a numerical inclined plane test that has been employed by several researchers (Chou et al. 2012; González-Montellano et al. 2012; Coetzee 2016), which are 0.67 and 0.7, respectively. The bottom loading cap is fixed and the top loading cap displaces in the vertical direction.

Similar to the laboratory triaxial tests, the numerical triaxial tests are simulated in three stages. Firstly, the DEM particles are generated randomly to fill an enclosed cylinder and then fall into the membrane under gravity. The top loading cap slightly moves up and down to compact the particles to match the laboratory porosity value. In the second stage, the confining pressures (150 and 250 kPa) are applied to the loading caps and the membrane simultaneously in all directions and are maintained during the tests. In the third stage, the top loading cap displaces vertically at a constant rate to shear the sample. A series of different loading rates are tested and a loading rate of 10 mm/s is used in all of the triaxial test simulations to optimise computational time and simulation accuracy while ensures the model is in a quasi-static condition during the shearing stage.

By trial-and-error, the numerical and laboratory results are shown in Figure 4.5. It can be seen that, the numerical model provides similar stress-strain curves to those obtained experimentally, at both 150 and 250 kPa confining pressures. Prior to reaching the peak, the numerical results are slightly higher than those obtained experimentally at both confining pressures. For a confining pressure of 150 kPa, the peak strength predicted by the numerical model is slightly lower than that measured in the laboratory. Some differences between the numerical and laboratory volumetric responses are observed in

Figure 4.5b, which may be explained by the adoption of spherical particles in the numerical model (Zhou et al. 2021). In general, however, the numerical results are in very good agreement with the laboratory results. Table 4.1 summarises the calibrated DEM input parameters.

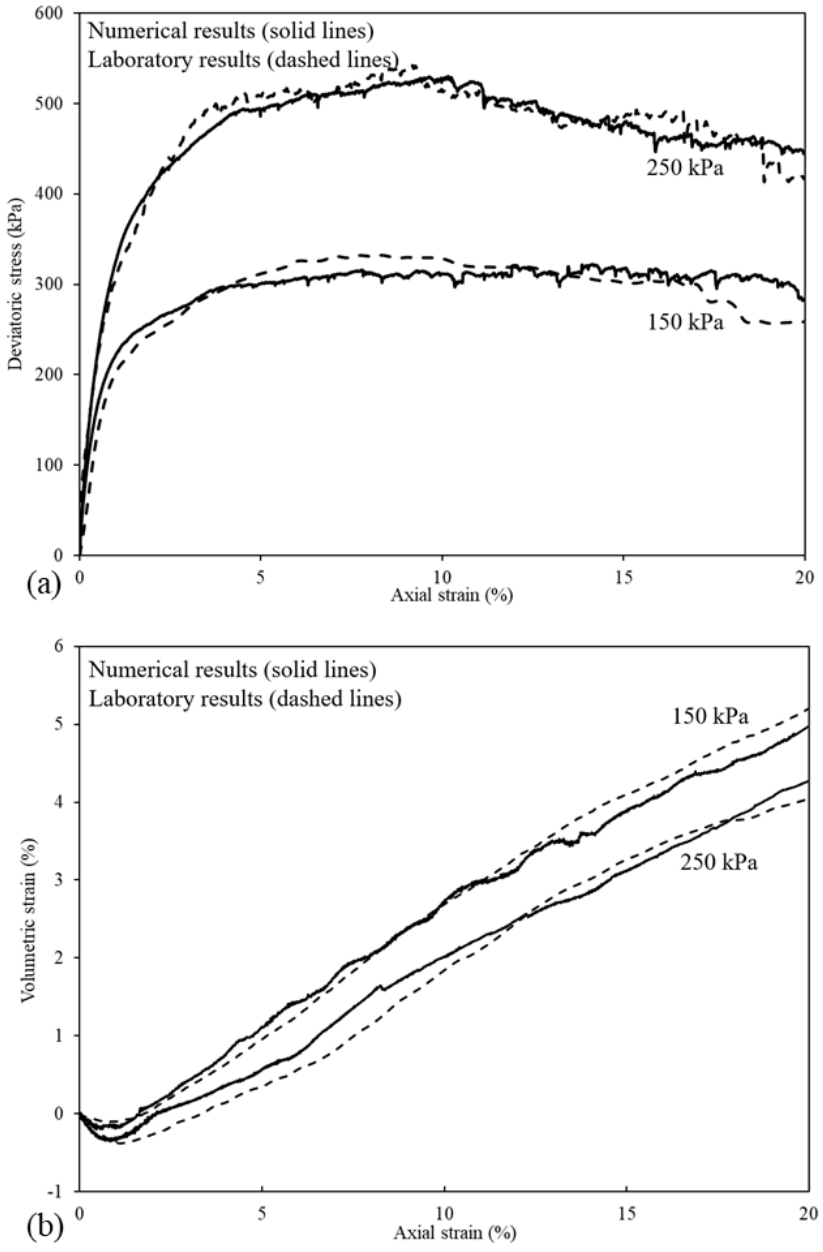

Figure 4.5: Experimental and numerical triaxial test results at confining pressures of 150 and 250 kPa: (a) stress-strain curves, (b) volumetric curves.

Table 4.1: Calibrated DEM input parameters.

Parameter	Value
Particle density (kg/m^3)	2,620
Particle diameter (mm)	1–3
Coefficient of friction	0.25
Normal and shear stiffnesses (k_n and k_s) (N/m)	6.5 ×10^5
Normal and shear damping ratios (β_n and β_s)	0.1
Young's modulus of loading caps (MPa)	7,200
Poisson's ratio of loading caps	0.25

4.3.2 Numerical RDC simulations

The calibrated DEM input parameters are adopted in the numerical RDC simulations. As shown in Figure 4.6, the numerical RDC model consists of a simplified 1:13 scale model of the roller, a chamber filled with soil particles and two timber frames. The chamber and timber frames are simulated using the FEM as rigid bodies and fixed at their initial locations, with no movement or deformation permitted during the compaction process. The size of the chamber is selected as 600 × 280 × 125 mm (length × width × height), considering the width of the module and the total number of particles in the numerical model. The height of the chamber has been demonstrated to be sufficient for compaction simulations, since the displacements of the soil particles located near the bottom of the chamber are negligible after 25 module passes, and it was reported by Chen et al. (2021), that the most significant compactive effects occur within the upper 100 mm depth. In addition, non-reflecting boundary conditions are applied to the DEM particles located near the boundaries of the chamber to prevent stress wave reflections. Since soil displacements are constrained by the edges of the chamber, ground improvement

occurred in the middle region of the chamber is analysed extensively to quantify the effectiveness of RDC.

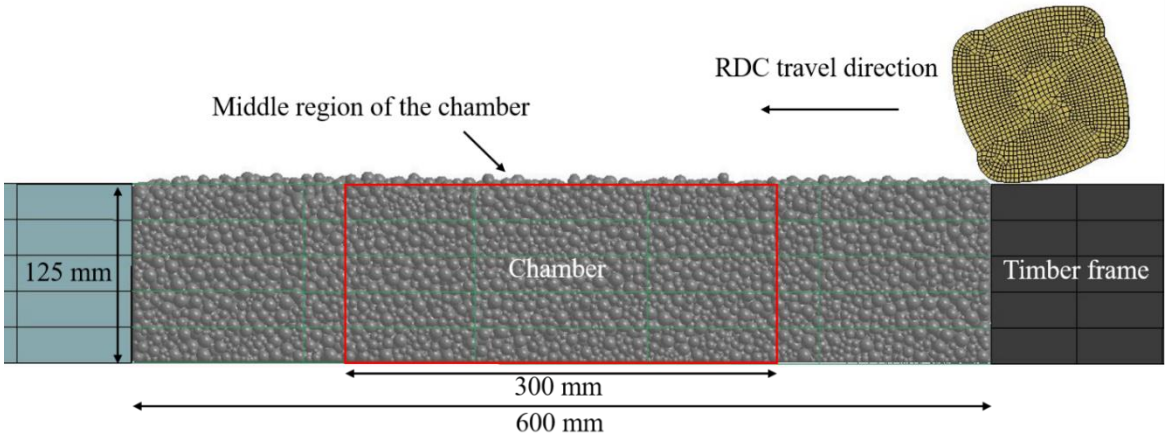

Figure 4.6: Setup of numerical RDC simulations.

The roller module with dimensions of 115 × 115 × 100 mm (height × length × width) is modelled using finite elements and defined to be a rigid body with a Young's modulus of elasticity of 210 GPa and Poisson's ratio of 0.28. As stated by Kuo et al. (2013) and Bradley et al. (2019), the roller deformation during compaction is negligible, since the roller is effectively rigid relative to the stiffness of the underlying soil. The friction coefficient between the particles and the roller module is 0.57, which is again obtained from the numerical inclined plane test. The motion (both horizontal and rotational speeds) of the roller module is defined in the numerical RDC model according to the operating speed of the full-size module in the field trial. The vertical speed is not constrained in the simulations, i.e. the numerical model predicts the module behaviour with respect to soil deformation. The initial starting position of the module for each pass was varied to simulate the same phenomenon that occurs in field operation.

In the numerical RDC simulations, the DEM particles are generated in a similar manner to that adopted in the numerical triaxial tests. Particles are generated randomly to fill a

rectangular box and fall into the chamber under gravity. Subsequently, a rigid plate is placed on the top of DEM particles and it is moved up and down to compact the particles slightly to assist the particles to settle in the chamber. After the particle assembly reaches a static and steady state, the rigid plate is removed and the RDC process commences.

Because of limitations associated with computational resources, the scaling approach proposed by Evans and Valdes (2011) is adopted to upscale the particle size distribution curve used in the calibration tests to reduce the total number of particles in the model and the simulation time. This scaling approach has been adopted in several DEM studies (e.g. Ciantia et al. 2015; Ciantia et al. 2016; Chen et al. 2018; Zhang et al. 2019) and has been demonstrated to be useful in replicating the behaviour of particle assemblies. The upper limit of particle scaling is governed by the relevant dimensions of the model (Ciantia et al. 2015). It is stated that the D_{50} of the scaled particles should be at least one order of magnitude lower than the relevant dimensions of the model. In addition, soil with maximum particle sizes of approximately 10 mm was adopted in the physical 1:13 RDC scale model tests performed by Chung et al. (2017) and no particle size effects were observed. Therefore, all DEM particles are upscaled uniformly to 3.5–10.5 mm, which then yields approximately 54,000 particles in the simulations (the soil initial void ratio in the numerical RDC simulations is 0.76). As mentioned above, to avoid size effects, the D_{50} of the scaled particles (7 mm) is one order of magnitude lower than the width of the roller module (100 mm). In order to preserve the macroscopic response of the particle assembly after scaling, the calibrated DEM input parameters are scaled accordingly, to account for the particle scaling factor (Feng and Owen 2014; Ciantia et al. 2015), which is 3.5 in this study. Table 4.2 displays the upscaled DEM input parameters.

Table 4.2: Scaled DEM input parameters.

Parameter	Value
Particle density (kg/m^3)	2,620
Particle diameter (mm)	3.5–10.5
Coefficient of friction	0.25
Normal and shear stiffnesses (k_n and k_s) (N/m)	2.275 ×10^6
Normal and shear damping ratios (β_n and β_s)	0.1

The stability of the numerical model is related to the adopted time step. The equations of motion in LS-DYNA are solved based on the explicit central difference scheme. Since both the FEM and DEM are used in this study, the critical time step (Δt) is calculated using the Equations (4.3)–(4.6) (Nakashima and Oida 2004; Lei and Zang 2010; LSTC 2018). In this study, the time step is controlled by Δt_{DEM}, which is 2.87×10^{-6} s.

$$\Delta t \leq min\{\Delta t_{DEM}, \Delta t_{FEM}\} \tag{4.3}$$

$$\Delta t_{DEM} = TSSFAC \cdot 0.2 \cdot \pi \cdot \sqrt{\frac{m}{k_n}} \tag{4.4}$$

$$\Delta t_{FEM} = \frac{l_{min}}{c} \tag{4.5}$$

$$c = \sqrt{\frac{E(1-\nu)}{(1+\nu)(1-2\nu)\rho}} \tag{4.6}$$

where Δt_{DEM} and Δt_{FEM} are the critical time steps for the discrete and finite elements, respectively; $TSSFAC$ is a time step scale factor in LS-DYNA, and the default value of $TSSFAC$ = 0.9 is used in this simulation; m and k_n are the mass and normal stiffness of the DEM particles, respectively; l_{min} is the minimum effective length of the finite elements; c is the velocity of the elastic wave; and E, ν and ρ are the Young's modulus, Poisson's ratio and the mass density of the finite elements, respectively.

4.3.3 Scaling laws

In order to compare the scale model results against those of the full-size RDC, the standard scaling laws for scale model testing under a normal (1*g*) gravity condition developed by Altaee and Fellenius (1994) were adopted. These scaling laws have been successfully used to upscale the results of the physical 1:13 RDC scale model tests conducted by Chung et al. (2017). The scaling laws are not only used to scale properties of the scale module itself, e.g. converting properties of the full-size model to the scaled module [Equations (4.7) to (4.9)], but are also used to upscale the results obtained from the scale model [Equations (4.10) to (4.12)]. Under 1-*g* conditions, the soil shows different behaviour since it is subjected to different stress conditions in the full-scale and the small-scale models. As proposed by Altaee and Fellenius (1994), the constitutive similarity is preserved in the small-scale model, if the initial soil states in the full-scale and the small-scale models have equal proximity to the steady state line. The steady state of soil is selected as the reference state since soil at the steady state is independent of the initial state. Since Chung et al. (2017) employed the same soil as the present study and found that the slope of the steady state line, $\lambda = 0.11$, that value has been adopted here. The geometric scale ratio, *n*, is 1/13 in this study.

$$\frac{L_m}{L_p} = n \tag{4.7}$$

$$\frac{M_m}{M_p} = n^3 \tag{4.8}$$

$$\frac{V_m}{V_p} = n \tag{4.9}$$

$$\frac{D_m}{D_p} = n \cdot \frac{\frac{\Delta e_m}{1+e_{0m}}}{\frac{\Delta e_p}{1+e_{0p}}} \tag{4.10}$$

$$\frac{\sigma_m}{\sigma_p} = \exp\left(\frac{e_{0p}-e_{0m}}{\lambda}\right) \tag{4.11}$$

$$\frac{E_m}{E_p} = \exp\left(\frac{e_{0p}-e_{0m}}{\lambda}\right) \times n^3 \quad (4.12)$$

where L is the characteristic length; M is the mass of the roller module; V represents the operating speed; D is soil vertical displacement; σ is the imposed stress in the soil; E is the energy imparted by the roller module; n is the geometric scale ratio; e_0 is the initial void ratio; Δe is the change in void ratio; λ is the slope of the steady state line in the e – log σ plane; and the subscripts m and p denote the scale model and prototype (full-size module in this context), respectively.

Therefore, based on Equations (4.7) to (4.9), the numerical 1:13 RDC scale model simulations are conducted with a 3.64 kg module operated at a speed of 235 mm/s, which corresponds to the 8-tonne prototype module travelling at 11 km/h, as adopted in the field tests. Pressures and accelerations were measured at 0.7 and 1.1 m depths below the ground in the field trial. Therefore, measurements are taken at 55 and 85 mm depths beneath the ground in the numerical simulations. In field trial, soil initial void ratio varied with depth due to the complex natural of the soil. The average initial void ratio and the initial void ratio of the soil near 0.7 and 1.1 m depths were approximately 0.52, 0.507 and 0.5, respectively (Scott et al. 2016). The average void ratio after 25 module passes in the numerical tests is approximately 0.66. The average void ratio after 25 module passes in the field tests was approximately 0.46, which is inferred from the change in ground settlement with respect to the number of passes, since the void ratio was measured only before and after 80 module passes in the field tests. These void ratios are substituted into Equations (4.10) to (4.12) to obtain the scaling factor for each parameter. Due to time and computational constraints, the numerical RDC simulations consist of 25 module passes. As a point of reference, one RDC simulation, consisting of 25 passes and approximately 54,000 particles, typically took approximately 30 days to run at 12 CPU cores using the

supercomputer mentioned above. It is worth mentioning that, the number of employed CPU cores is constrained by the number of available ANSYS licenses.

4.4 Comparisons between numerical model and field trial

Numerical results are compared with those from the field trials by examining four different parameters namely, displacements at the ground surface, and at depths of 0.7 and 1.1 m, pressures at 0.7 and 1.1 m depths, energy delivered by the RDC module into the underlying soil, and the depth of major improvement. These are each presented in turn.

4.4.1 Soil vertical displacements

Soil displacement is an important indicator of the soil behaviour as a consequence of RDC. Soil displacements at different depths within the numerical simulations are calculated by averaging all particle displacements at the depth of interest within the middle region of the chamber as shown in Figure 4.6. These are presented in Figures 4.7 to 4.9 and are upscaled using Equation (4.10) based on average void ratios of the soil measured before and after compaction in the field study (0.52 and 0.46, respectively) and in the numerical model (0.76 and 0.66, respectively). Ground settlements obtained from the numerical model, together with field tests, are displayed in Figure 4.7. As can be seen from both the numerical simulations and the field tests, the ground settlement increases with the number of passes. Two trend lines are used to fit the numerical and field results, and the shape of the two trend lines is very similar. It can be observed that the numerical model predicts the field test results very well. The numerical model predicts the ground settlement of 71.7 mm after 25 module passes, which is very close to that measured in field tests of 66.2 mm, with a difference of 5.5 mm (8.3%). This discrepancy can be explained by the limitations of the less accurate surveying method used in the field and the simplification

of adopting spherical DEM particles in the numerical model. In summary, the results show that the numerical model is able to predict, reasonably well, soil settlements induced by RDC.

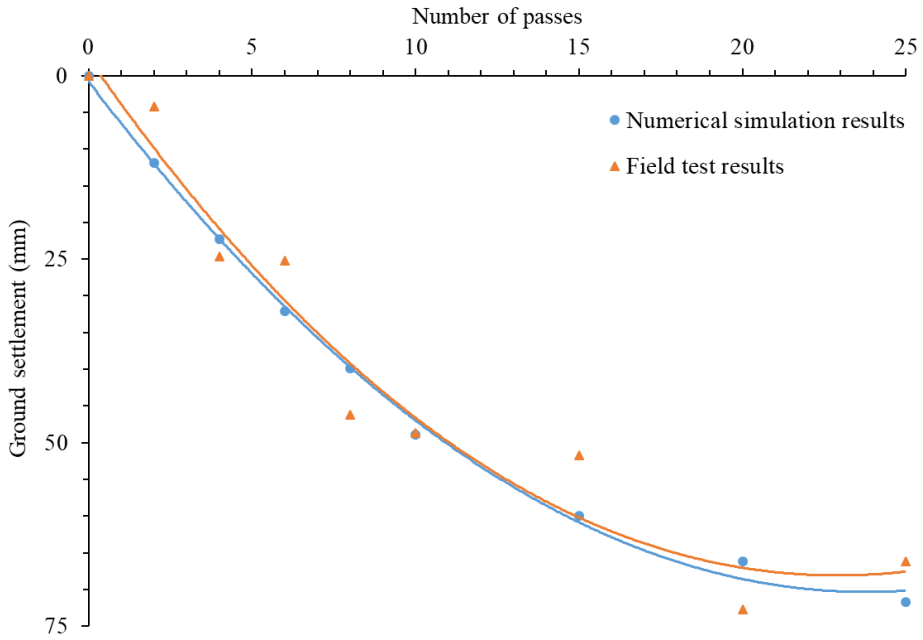

Figure 4.7: Ground settlements obtained from the numerical model and field tests with respect to number of passes.

Vertical displacements obtained from the numerical model and field tests at 0.7 and 1.1 m depths are presented in Figure 4.8. It is important to note that field displacements were calculated by integrating vertical accelerations, measured by accelerometers, with respect to time. As shown in Figure 4.2, the length of field test pad was 4 m, and each accelerometer was placed 1.25 m from the edge of the test pad. As a result, field displacements are obtained from one location along the entire length of the test pad and, as such, do not represent average soil displacements at the test depths of 0.7 and 1.1 m. Therefore, the field displacements are also presented in Figure 4.8 for reference purposes. This also highlights a significant limitation with field testing, which is the difficulty of obtaining high fidelity measurements of internal soil displacements. In contrast, the numerical model provides great flexibility in this regard as it enables the movement of

every individual particle to be tracked. In general, the soil displacements increase with increasing compactive effort. When compared against the field results, the numerical model yields much smoother vertical displacement results since the numerical displacements at 0.7 and 1.1 m depths are calculated by averaging the displacements of all of the soil particles at each depth (approximately 500 particles) within the central region of the chamber.

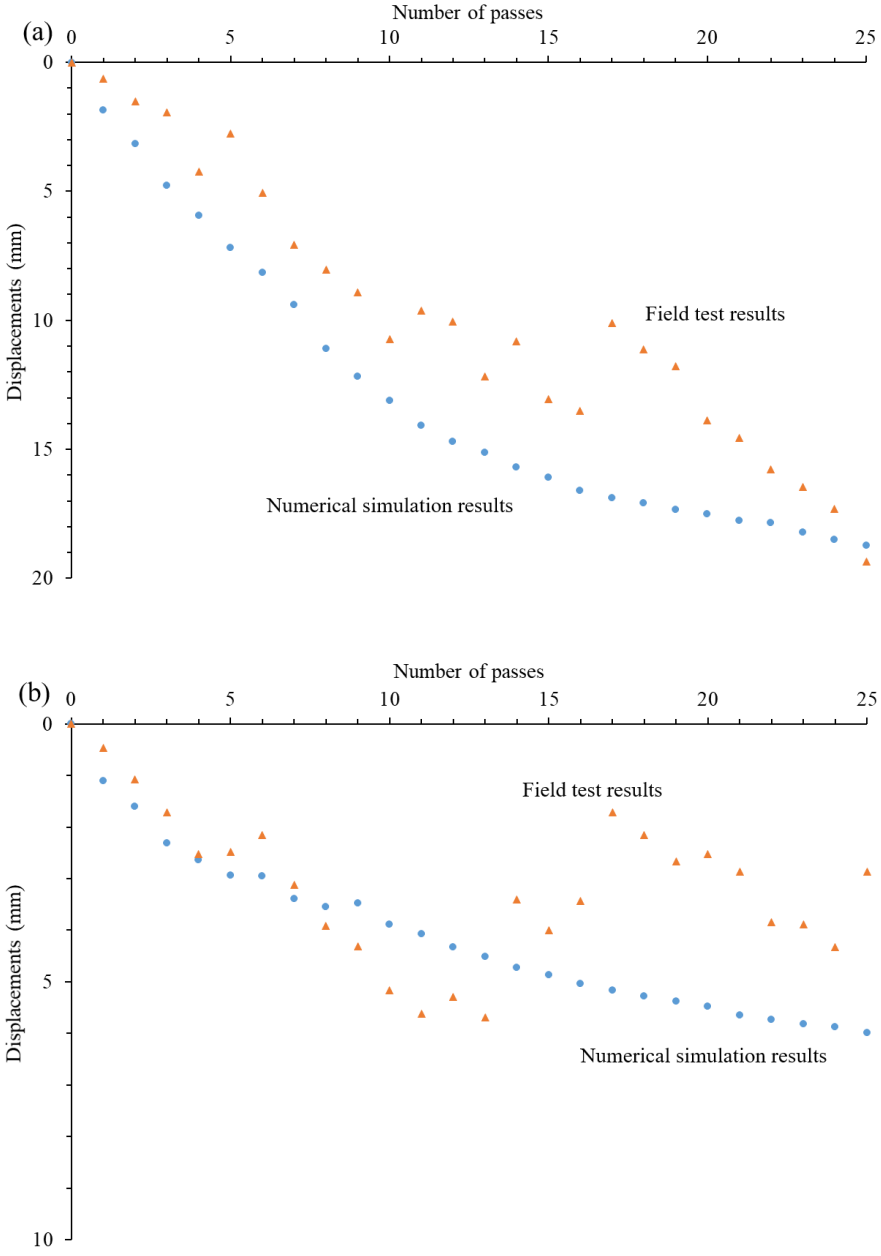

Figure 4.8: Vertical displacements obtained from the numerical model and field tests, with respect to number of passes, at: (a) 0.7 m depth, (b) 1.1 m depth.

The numerical vertical displacements with depth, as presented in Figures 4.7 and 4.8, are combined and superimposed in Figure 4.9. As can be seen, each of the three curves show a trend of increasing vertical displacement with number of passes, but tends to plateau after approximately 20 passes. In addition, it can be observed that, as expected, the soil displacements decrease with increasing depth due to the dissipation of compactive energy with depth.

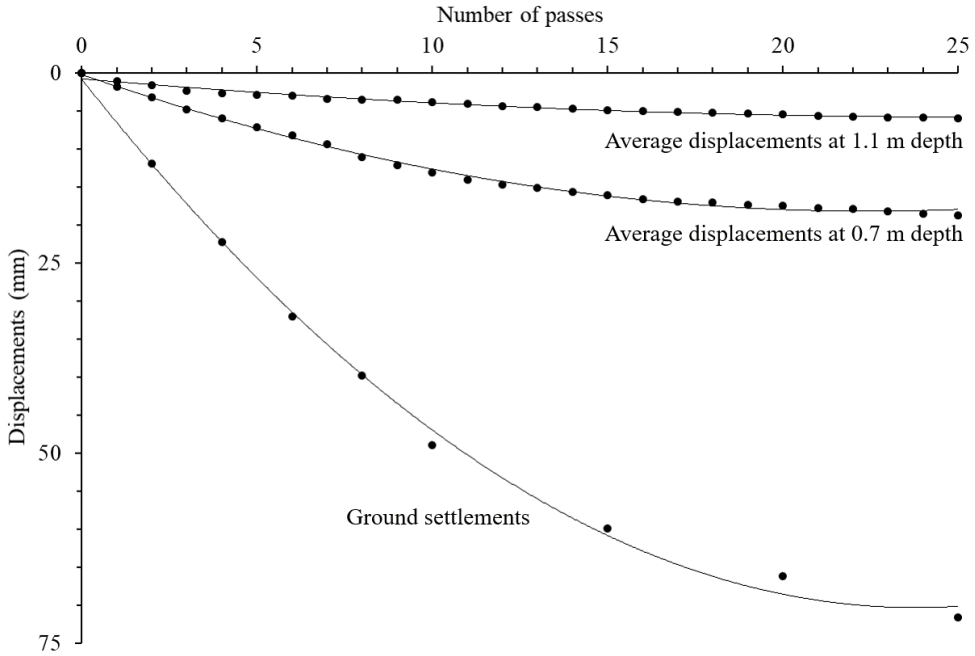

Figure 4.9: Average vertical displacements at different depths with respect to number of passes from the numerical model.

4.4.2 Peak pressures

The peak pressure recorded at different depths below the ground surface reflects the influence of RDC within the soil body. As mentioned above, pressures induced by RDC were measured by EPCs in the field tests. The diameter of the EPCs is 230 mm, which equates to approximately 17.7 mm at the scale of the numerical model [Equation (4.7)]. The D_{50} of the particles is approximately 7 mm, therefore, pressures are averaged over three adjacent particles. It is worth mentioning that, numerical pressures obtained from

one particle are calculated based on the resultant force acting on that particle, and the resultant force is determined by summing the contact forces and externally applied forces acting on that particle (Davidson et al. 2015). A single particle interacts with at least 4 to 5 surrounding particles in the simulations. Therefore, the numerical pressures are calculated from the contact forces between up to 15 particles. Additionally, the pressures induced by the module are significantly affected by the offset distance (this is presented in detail below), hence, the particles used to determine the average pressures should be limited to a relatively small number to ensure accuracy at a given offset distance. This is similar to the measurement of pressures in the field tests. At each depth, the EPCs were placed at a single location over the 4 m length trial pad to measure pressures with respect to offset distance (Figure 4.2). Peak pressures recorded at each module pass from numerical simulations are included in Figures 4.10 to 4.12 and are upscaled using Equation (4.11) in order to facilitate comparison with the field measurements.

Figure 4.10 shows the measured numerical and field peak pressures versus the number of passes at 0.7 and 1.1 m depths. There is no clear relationship between the peak pressures and the number of passes for both the numerical results and field data. It is evident that the value of recorded peak pressure varies for each pass. The reason for this is that the RDC module typically impacts the ground at a different location with each pass, which results in the offset distance between the centre of the module and EPC varying with each pass. The peak pressure measured for each pass from the numerical model cannot be directly compared with those recorded in field tests, since the offset distance for each pass is different in the numerical model and the field tests.

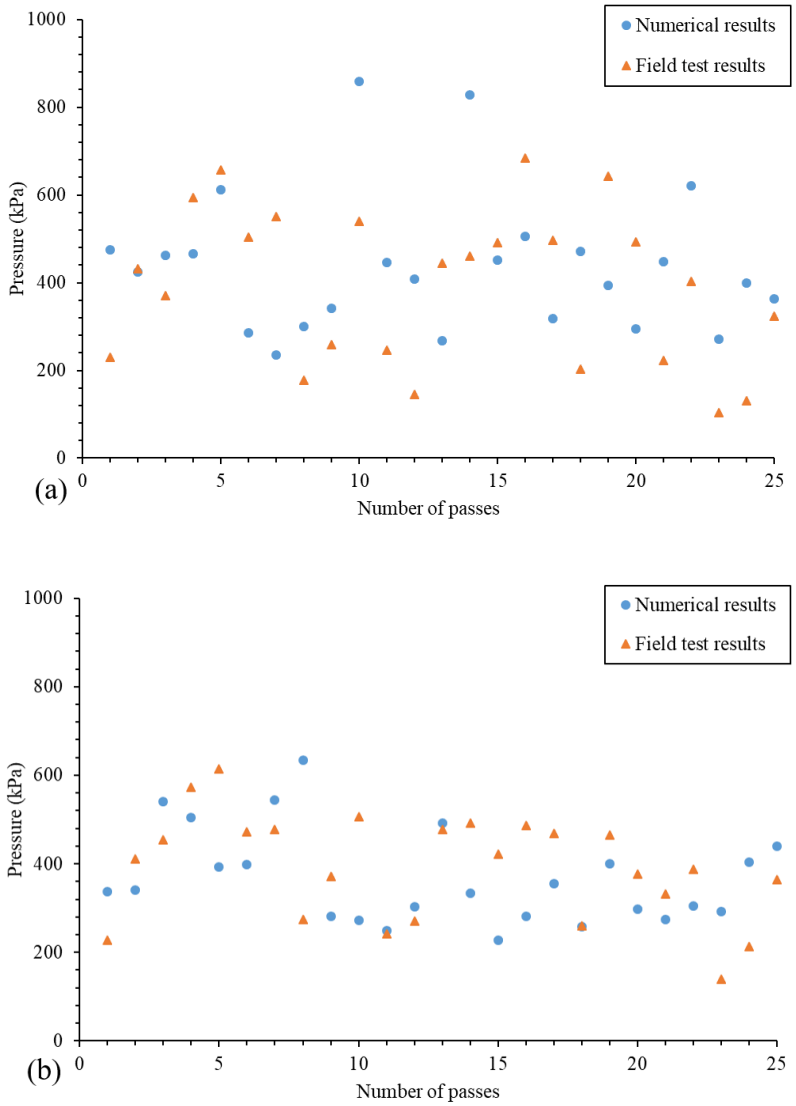

Figure 4.10: Pressures obtained from the numerical and field tests, at: (a) 0.7 m depth, (b) 1.1 m depth.

Figure 4.11 presents box plots of the measured numerical and field peak pressures. The field peak pressures at 0.7 m depth have minimum and maximum pressures of 104 and 685 kPa, respectively, with a mean value of 392 kPa and standard deviation of 177 kPa. Numerical peak pressures at 0.7 m depth have minimum and maximum pressures of 235 and 858 kPa, respectively, with a mean value of 438 kPa and standard deviation of 158 kPa. Although the numerical results yield a greater maximum pressure than that measured in the field at 0.7 m depth, the results from the numerical model have a similar mean and standard deviation values as those calculated from the field tests. The numerical results at a depth of 1.1 m have mean and standard values of 366 and 107 kPa, respectively,

whereas, the field measurements have a mean of 391 kPa and standard deviation of 121 kPa. The average pressure at 1.1 m depth from the numerical model is consistent with that measured in field study.

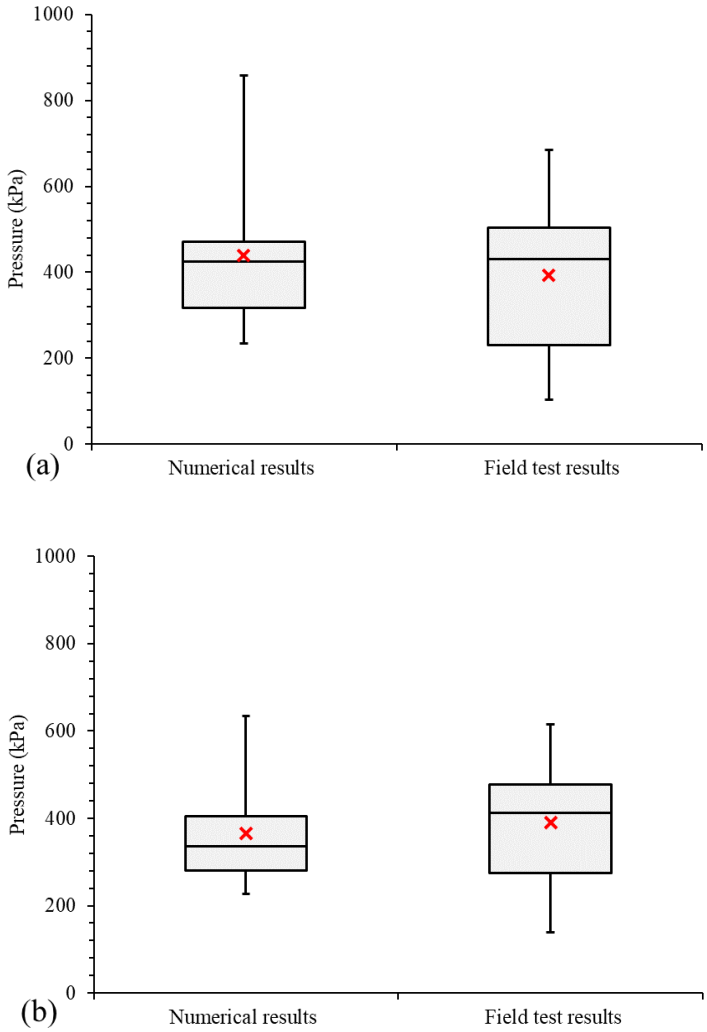

Figure 4.11: Box plots of peak pressures obtained from the numerical and field tests, at: (a) 0.7 m depth, (b) 1.1 m depth.

It can be observed that the average pressures predicted by the numerical model are consistent with those recorded in the field trial at both 0.7 and 1.1 m depths. However, as indicated by the quartiles, the numerical peak pressures have a narrower range of variation when compared with those recorded in the field. One possible reason may be the adoption of spherical particles in the numerical model which results in a wider load distribution

angle that spreads the imposed pressure over a greater area and subsequently reduces the variation in pressure. Another reason may relate to the variation in the void ratios of the soil in the field. As mentioned above, the field void ratio of the soil varies with depth, as a natural consequence of its placement, which may affect the propagation of pressure waves within the soil body and this is likely to cause greater variation in the pressure measurements.

In the numerical simulations, pressures are averaged over three particles located adjacent to each other. The coordinates of these three particles are also averaged, and the distance between the averaged coordinates and the centre of the module face, is taken as the offset distance for each module pass. The relationship between peak pressures and offset distance is presented in Figure 4.12. It can be seen that recorded peak pressures have a strong relationship with the offset distance in the field tests. In addition, the variation of offset distance confirms that the RDC module impacts the ground at a different location at each pass, and it is a random process for the module to strike the ground either in front of or behind the EPCs. As can be observed, the same conclusion can be drawn from the numerical results. As shown in Figure 4.12, higher pressures are imparted to the soil when the EPCs are located in front of the roller, and the distance between the EPCs and the centre of the module is between 200 and 650 mm in the numerical model and field tests at both 0.7 and 1.1 m depths. Figure 4.12 also demonstrates the pressure distribution beneath the contact face between the roller module and the soil is non-uniform. As shown in Figure 4.12a, numerical peak pressures with respect to the offset distance exhibit similar trends to those of the field data at 0.7 m depth. At 1.1 m depth (Figure 4.12b), when compared with the field data, the numerical model yields smaller peak pressures and this may be explained by a wider load distribution angle caused by spherical particles in numerical simulations that lowers the pressures at deeper depths, as suggested earlier.

Therefore, in general, it can be concluded that the numerical model provides reasonable predictions of the peak pressures imparted by the module, and the distribution of peak pressures with respect to offset distance. In addition, the plots of peak pressures against offset distance in Figure 4.12 also show that the offset distance has a greater influence on peak pressures at shallow depths (0.7 m). A similar observation was reported by Scott et al. (2020), who plotted peak pressures with offset distance at 0.5, 1.0, and 1.5 m depths below the ground. They stated that the effects of offset distance on peak pressure decrease with increasing depth because the energy imparted by RDC diminishes radially from the centre of the impact with depth.

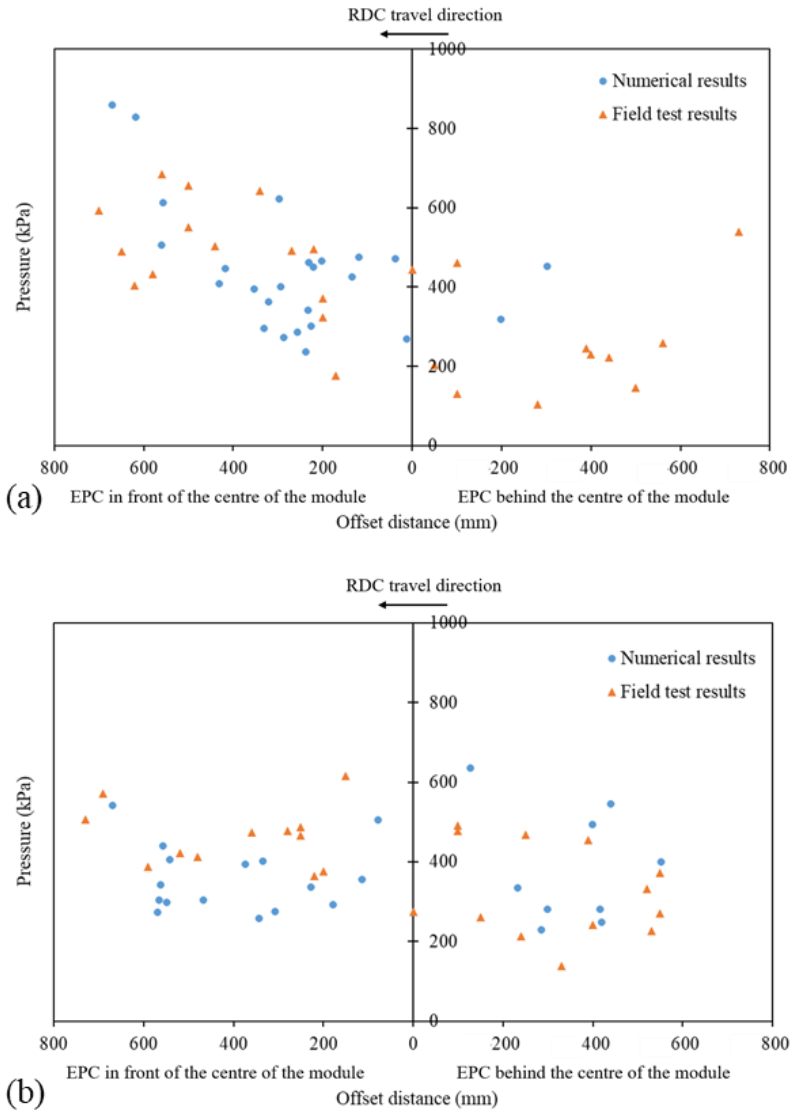

Figure 4.12: Peak pressures versus offset distance obtained from the numerical and field tests, at: (a) 0.7 m depth, (b) 1.1 m depth.

4.4.3 Energy imparted by RDC

Scott et al. (2019b) quantified the effects of RDC in terms of the work done on the soil from measured force-displacement data obtained from the field tests. They calculated the force-displacement data from the pressure-displacement measurements obtained from EPCs and accelerometers, and the plot of the force versus displacement was integrated to quantify the work done on the soil at a single location. If the force-displacement curves for all of the soil particles within the module influenced region are plotted, the total work done on the subsurface profile by a single module impact can be calculated, and then the total energy delivered to the ground can be quantified. However, the process of obtaining force-displacement curves for all soil particles within the module influenced region is impractical and unnecessary. In fact, the energy imparted by the module at each impact is calculated directly by LS-DYNA, based on the motion of the roller module. As mentioned above, the motion (horizontal and rotational speeds) of the roller module is defined in the numerical RDC model according to the full-size module speed used in the field tests. The vertical speed of the roller module is calculated by the numerical model, based on the horizontal and rotational module speeds, the ground conditions and the undulating surface induced by the module. The drop height of the module at each impact is also predicted by the numerical model. The energy results from LS-DYNA are interrogated from several module impacts and then upscaled using Equation (4.12). It is determined, with 95% confidence, that the module delivers approximately 24 ± 3 kJ to the ground at each impact. This value is compared with the energy equation proposed by Bradley et al. (2019) shown in Equation (4.13):

$$E_{Roller} = \frac{1}{2} \times M_{Roller} \times \left({v_y}^2 + {v_z}^2\right) + \frac{1}{2} \times I_{Roller} \times {\omega_y}^2 + M_{Roller} \times g \times h_{Roller} \quad (4.13)$$

where E_{Roller} is the energy of the roller; M_{Roller} is the mass of the roller; I_{Roller} is the mass moment of inertia of the roller; h_{Roller} is the height of the roller's centroid above

the ground surface; and v_y, v_z, and ω_y are the horizontal, vertical, and angular velocities, respectively.

The energy delivered to the ground is a result of the changes in the energy of the roller during each impact. Therefore, the relationship shown in Equation (4.14) can be derived from Equation (4.13), and is used to calculate the energy transferred by the roller to the underlying soil.

$$\Delta E = \frac{1}{2} \times M_{Roller} \times \left({v_{zi}}^2 - {v_{zf}}^2\right) + \frac{1}{2} \times I_{Roller} \times \left({\omega_{yi}}^2 - {\omega_{yf}}^2\right) + M_{Roller} \times g \times \Delta h_{Roller} \quad (4.14)$$

where v_{zi} and v_{zf} are the vertical velocities before and after the roller impact, respectively; ω_{yi} and ω_{yf} are the angular velocities before and after the roller impact, respectively; and Δh_{Roller} is the module drop height after impact.

In the simulations, the horizontal velocity of the module is constant (235 mm/s), and the vertical velocity changes with respect to time, which results in changes in angular velocity. A random impact is selected to calculate the energy delivered to the soil using Equation (4.14). The vertical velocities before and after this impact are 46.7 and –30 mm/s, respectively, where a positive vertical velocity implies that the module moves upwards and vice versa. Therefore, angular velocities before and after this module impacts the soil are 4.11 and 2.99 rad/s, respectively. Equation (4.9) is then applied to upscale the velocities. The Δh_{Roller} is approximately 10.5 mm during this impact, which corresponds to 0.14 m in the full-size module. The I_{Roller} is 2.631×10^9 kg.mm^2 for the full-size module (Bradley et al. 2019). By substituting the full-size module values of velocities, Δh_{Roller}, I_{Roller} and M_{Roller} into Equation (4.14), the energy imparted by a single impact is calculated as approximately 22 kJ. Based on Equation (4.13), the peak kinetic energy

of the roller at impact is also calculated as approximately 61 kJ. As a result, the energy delivered to the soil at each module impact calculated from Equation (4.14) is thus consistent with that obtained from LS-DYNA. In addition, Scott et al. (2020) reported the energy delivered to the ground by RDC is approximately 27 kJ for an operating speed of 11 km/h. It is important to note that the 27 kJ is the maximum theoretically possible energy imparted into the ground, and this value may not be achieved at every impact since ground conditions affect the delivery of potential energy. The energy imparted to the soil predicted by LS-DYNA fits well with that stated by Scott et al. (2020). Therefore, it can be concluded that the LS-DYNA predicts well the RDC impact energy.

4.4.4 Depth of major improvement

The improvement of the underlying soil can be inferred from pressure readings, however, as the soil density increases, pressure waves are more readily able to be propagated, which results in measurable pressure readings at deeper depths. However, soil particles located at those deeper depths may not experience any permanent displacements (hence, increase in density). On the other hand, several researchers have focussed on the depth of influence, which was defined by Kim (2011) as being equivalent to the depth at which the soil has a vertical stress equal to approximately 10% of the applied stress at the ground surface. In contrast, Scott et al. (2019a) suggested that the depth of major improvement (DMI) is a more appropriate measure to determine the thickness of layers that can be compacted by RDC. DMI implies the depth of soil over which, the soil is improved to meet the target criterion that can be achieved by conventional compaction equipment in thin lifts. The relationship shown in Equation (4.15) is proposed by Scott et al. (2019a) to calculate DMI.

$$\text{DMI} = r \cdot k \cdot (n\sqrt{m\Delta h}) \tag{4.15}$$

where r is a constant (0.5 – 0.67); k is the ratio of the energy delivered to the ground divided by the change in gravitational potential energy at each impact; n is an empirical factor which relates to soil conditions (0.3 – 0.8); m is the mass of the roller module in tonnes; and Δh is module drop height after impact in metres.

The DMI in the numerical RDC model is calculated using Equation (4.15). The average module drop height after impact (Δh) is approximately 11.5 mm in the numerical model, which corresponds to 0.15 m in the full-size module. Therefore, the average change in potential energy due to the lift height of the roller per module impact ($mg\Delta h$) is approximately 11.7 kJ. The k value is then obtained based on the ratio between energy imparted to the underlying soil (24 kJ demonstrated in the previous section) and the average change in potential energy (11.7 kJ), which is approximately 2.05. The value of n varies between 0.3 and 0.8. As proposed by Mayne et al. (1984) and Scott et al. (2019a), for granular soil, higher values of n apply. Sandy gravel soil is used in this study, therefore, n = 0.8 is adopted. By substituting the values of k, n, m and Δh into Equation (4.15), for the full-size model, DMI = 0.9 to 1.2 m. For the 1:13 scale model [Equation (4.7) is adopted to account for the 1:13 geometric ratio], DMI = 69 to 92 mm.

The calculated value of DMI proposed by Scott et al. (2019a) is compared against that obtained from the numerical model based on movement of soil particles. As stated earlier, RDC improves the density of the ground by applying mechanical energy to reduce air voids and rearrange, and in some cases fracture, the soil particles. Therefore, the movement of the underlying soil is a direct indicator of the effectiveness of RDC. Velocity vectors and force chains obtained from the numerical model at the 25th module pass are shown in Figure 4.13. From Figure 4.13, it is clear that there is a region where soil particles located within this zone have greater velocities (hence, displacements). The

depth of this zone is approximately 70 mm, which sits within the range of DMI calculated from Equation (4.15). Forces acting on soil particles are transmitted through contacts between the particles and, in order to visualize the propagation of forces, lines are used to represent contact forces between particles, which are known as force chains (LSTC 2018). During the compaction processes, former force chains collapse and new force chains are established. According to Muthuswamy and Tordesillas (2006), a force chain is formed by a set of contacts between particles that carries the majority of the load. The main direction of the force chain is generally consistent with the orientation of the applied stress (Majmudar and Behringer 2005). From Figure 4.13b, greater contact forces can be observed within the DMI. Although there are contact forces developed below the DMI region, these low contact forces are likely not to induce any significant soil improvement.

In addition, in order to investigate the relationship between induced pressures, soil displacements and DMI, the maximum pressures measured over 25 passes, and the soil displacements recorded after 25 module passes, are plotted with respect to depth in Figure 4.14. The numerical soil displacements and pressures presented in Figure 4.14 were upscaled using Equations (4.10) and (4.11), respectively. The trend line is obtained from the numerical peak pressures, and the field peak pressures are superimposed for reference purposes. In the field tests, the pressures were measured at only two depths, hence only two field points are available. As one would expect, both pressures and soil displacements decrease with increasing depth because the compactive energy dissipates with depth. It can be seen that, the pressure and soil displacement plots follow similar trends, which suggests that soil displacements are strongly related to the induced pressures, as one would expect. The major difference between the pressure and soil displacement plots is that soil displacement is less than 5 mm after 25 passes below 1.2 m and it closes to zero near 1.5 m depth, however, the trend line of pressure suggests that pressure is still

measureable below 1.5 m depth. This is consistent with the force chains plot presented earlier in Figure 4.13b. As suggested previously, these low pressures at greater depths are unlike to produce any significant improvement in soil density. Additionally, pressures presented in Figure 4.14a are peak pressures recorded over 25 module passes and these values cannot be achieved with each module pass. It is worth noting that soil displacements less than 5 mm result in a reduction in void ratio of only 0.005 in the field tests, which is negligible. Therefore, the majority of soil displacements occur above 1.2 m depth, which is within the range of DMI calculated from Equation (4.15). Hence, it is concluded that DMI calculated from Equation (4.15) is consistent with that deduced from the numerical RDC model.

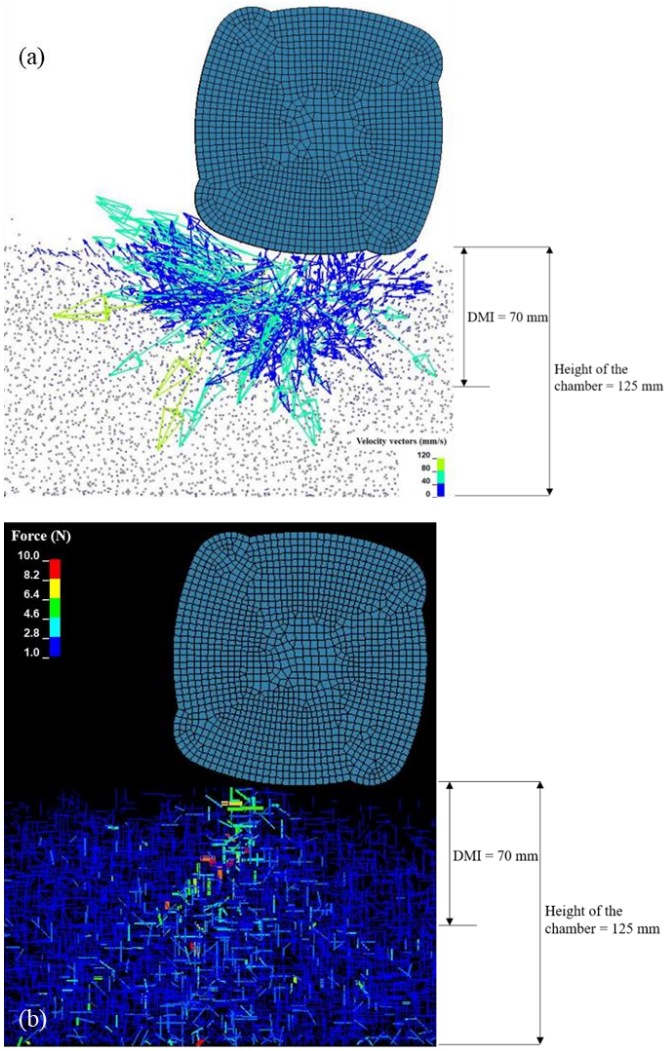

Figure 4.13: Numerical results of soil particles at the 25th module pass: (a) velocity vectors, (b) force chains.

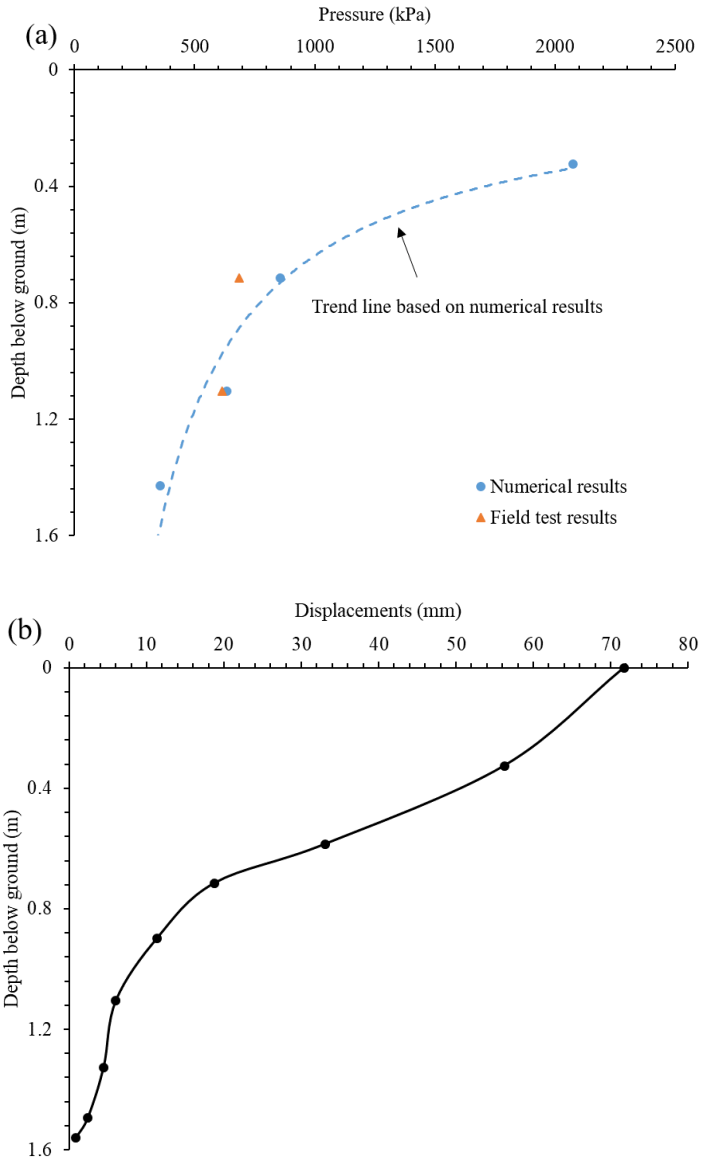

Figure 4.14: Pressures and displacements at different depths: (a) peak pressures over 25 module passes, (b) soil displacements predicted by the numerical model after 25 module passes.

4.5 Optimum number of passes

In the field, several in situ tests are typically undertaken such as nuclear density tests, DCP testing and CPTs, to quantify the optimum number of RDC passes. However, the application of these in situ tests are limited due to the budget and time constraints, and difficulties with the testing process (Jaksa et al. 2012). Ground settlement is commonly adopted as a key indicator of ground improvement due to RDC, since the measurement of ground settlement is efficient and cost-effective. However, Scott et al. (2016) proposed

that ground settlements are an inadequate indicator of ground improvement within the soil mass. As a consequence, Scott et al. (2016) buried EPCs and accelerometers in the soil at targeted depths to quantify the level and extent of ground improvement. EPCs and accelerometers provide insights into the influence of RDC within the soil body. However, their deployment and post-processing is not straightforward. Alternatively, in the present study, the numerical model is interrogated to assess whether or not it provides any insights into the optimum number of RDC passes.

Earlier, Figure 4.10 presented the numerically observed peak pressures with respect to the number of passes. Theoretically, peak pressures rise with increasing passes and soil density. However, due to variations in the offset distance, the relationship is unclear. Perhaps a more helpful indicator is the displacement at different depths with respect to number of passes, which was shown earlier in Figure 4.9. As can be seen, in general, soil displacements increase with the number of passes. Displacements at 0.7 and 1.1 m depths show no obvious increase after approximately 20 passes. The ground settlement increases significantly up to the first 15 passes, and thereafter it increases modestly. Velocity vectors and force chains of soil particles at the 5^{th} pass are displayed in Figure 4.15. It can be observed that, the magnitudes of the velocity vectors are greater, and the DMI is smaller at the 5^{th} module pass when compared against the 25^{th} pass shown in Figure 4.13. Additionally, comparing with the 5^{th} module pass, the compactive energy induced by the module at the 25^{th} pass is transmitted to greater depths, as evidenced by more force chains formed at deeper depths, which confirms that the pressures rise with the increasing passes and soil density. However, due to the influence of the offset distance, it is difficult to obtain this relationship from the field tests. The DMI calculated at each module pass is plotted against the number of passes in Figure 4.16. As can be seen, the DMI increases with the number of passes, and the most significant increase occurs during the first 5

passes and, after approximately 20 passes, the DMI plateaus. Hence, both the DMI and settlements indicate that after 20 passes, the soil has been effectively compacted and that additional passes provide only modest improvement.

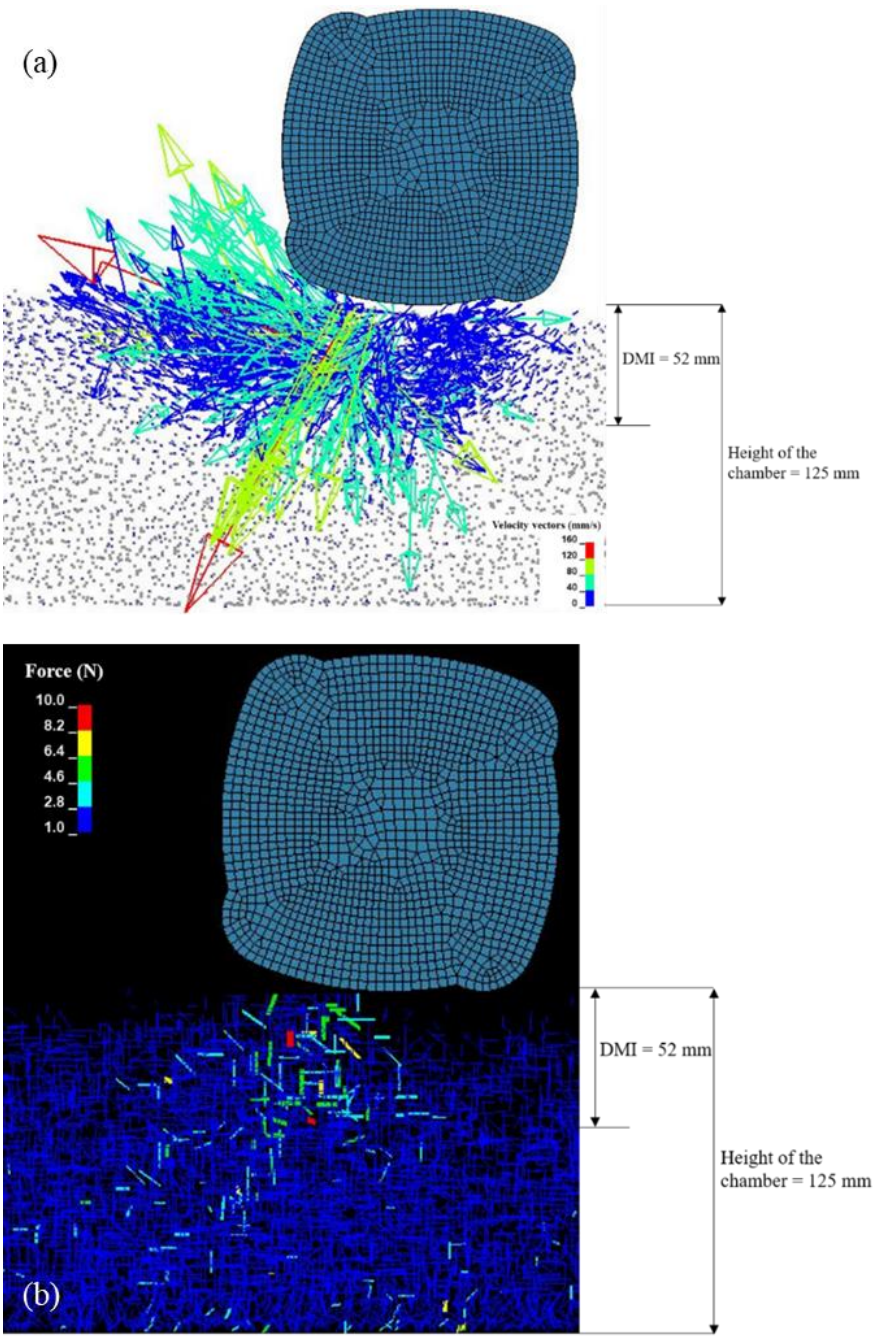

Figure 4.15: Numerical results of soil particles at the 5th module pass: (a) velocity vectors, (b) force chains.

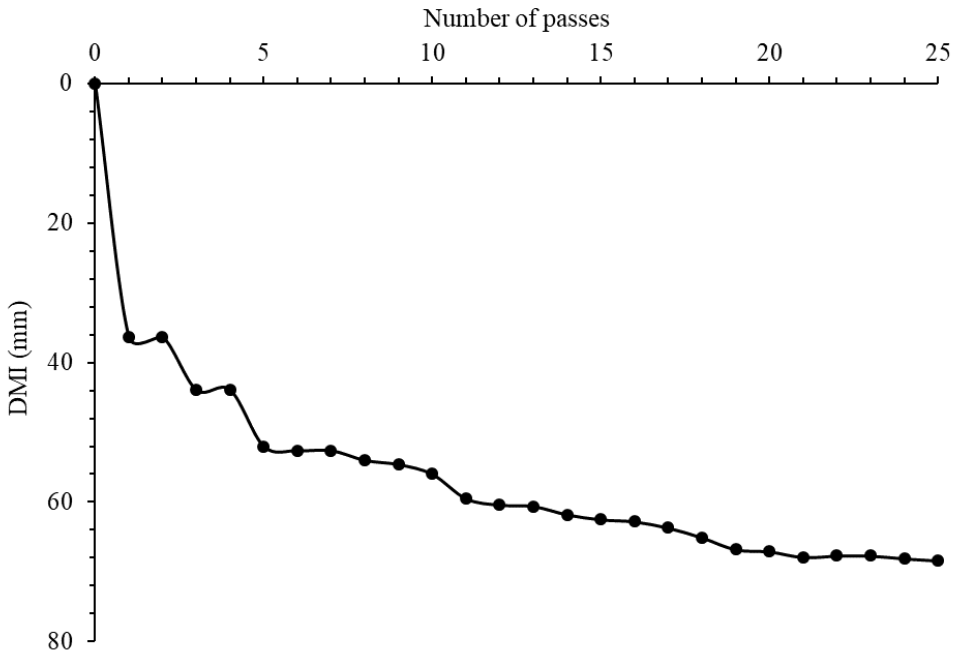

Figure 4.16: DMI versus number of passes.

In summary, pressure results are an imperfect indicator on which to assess the optimum number of RDC passes, whereas, in contrast, both DMI and soil displacements are helpful in this regard.

4.6 Summary and Conclusions

This paper has developed and validated a FEM-DEM numerical scale model of the 4-sided, 8-tonne, Broons BH-1300 impact roller against field tests. The numerical input parameters were calibrated against laboratory triaxial tests performed on the same type and grading of soil that was used in field tests. In the numerical RDC simulations, the RDC module, the chamber and two timber frames were described by the FEM and the soil particles were simulated by the DEM. The numerical results were compared against the field data from four aspects, namely soil displacements at different depths, peak pressures measured at each pass, the energy delivered to the underlying soil, and the depth of major improvement. It has been demonstrated that the numerical results are in very

good agreement with the field observations, which suggests that the numerical model provides reasonable predictions of ground improvement due to RDC. The results obtained from the numerical model were analysed and evaluated to obtain an efficient indicator to determine the optimum number of passes. Ground settlement was recommended, since it reflected ground improvement due to RDC and it exhibited a clear relationship with the number of passes. In addition, ground settlement can be measured in a more efficient and cost-effective manner in the field.

In general, the results of this study suggest that the FEM-DEM model provides a promising and reliable means for understanding and assessing the effectiveness of RDC. It provides several benefits over field- and laboratory-based testing but, due to its heavy reliance on supercomputing facilities will, for the time being, remain a research rather than a practical tool. In addition, conclusions drawn from this study are based on one module mass and a single operating speed. Future work will extend this model by examining the optimal operating speed and also explore the effectiveness of different RDC modules.

4.7 Acknowledgements

The authors wish to acknowledge the computational resources provided by the Phoenix HPC service at the University of Adelaide. The authors are also wish to thank the following final year undergraduate students who contributed to the test results referred to within this paper: Stefan Chenoweth, Jordan Colbert, Julianne Saw, Ross Vince, Dan Nguyen, Keegan Steele, Samuel Brown and Thomas Muecke.

4.8 References

Altaee, A., Fellenius, B. H., 1994. Physical modeling in sand. *Canadian Geotechnical Journal*. 31, 420-431.

Avalle, D., Carter, J., 2005. Evaluating the improvement from impact rolling on sand. Proc. 6th Int. Conf. on Ground Improvement Techniques, Coimbra, Portugal, pp. 1-8.

Avalle, D., Grounds, R., 2004. Improving pavement subgrade with the" square" impact roller. *SATC 2004*.

Avalle, D. L., McKenzie, R. W., 2005. Ground improvement of landfill site using the square impact roller. *Australian Geomechanics*. 40, 15-21.

Avsar, S., Bakker, M., Bartholomeeusen, G., van Mechelen, J., 2006. Six sigma quality improvement of compaction at the New Doha International Airport Project. *Terra et aqua*. 103, 14.

Bouazza, A., Avalle, D. L., 2006. Effectiveness of rolling dynamic compaction on an old waste tip. *ISSMGE 5th International Congress on Environmental Geotechnics*, Cardiff, 1.

Bradley, A. C., Jaksa, M. B., Kuo, Y.-L., 2019. Examining the kinematics and energy of the four-sided impact roller. *Proceedings of the Institution of Civil Engineers - Ground Improvement*. 172, 297-304.

Calvetti, F., Viggiani, G., Tamagnini, C., 2003. A numerical investigation of the incremental behavior of granular soils. *Rivista italiana di geotecnica*. 37, 11-29.

Chen, Y., Deng, A., Wang, A., Sun, H., 2018. Performance of screw–shaft pile in sand: Model test and DEM simulation. *Computers and Geotechnics*. 104, 118-130.

Chen, Y., Jaksa, M., Kuo, Y., Airey, D., 2021. Experimental Analysis of Rolling Dynamic Compaction Using Transparent Soils and Particle Image Velocimetry. *Canadian Geotechnical Journal*, Available from http://dx.doi.org/10.1139/cgj-2020-0573.

Chou, H., Lee, C., Chung, Y., Hsiau, S., 2012. Discrete element modelling and experimental validation for the falling process of dry granular steps. *Powder technology*. 231, 122-134.

Chung, O., Scott, B., Jaksa, M., Kuo, Y., Airey, D., 2017. Physical modeling of rolling dynamic compaction. *Proceedings of the 19th Int. Conf. on Soil Mechanics and Geotechnical Engineering*, Seoul, Korea, Sept. 18–22, 905–908.

Ciantia, M., Arroyo Alvarez De Toledo, M., Calvetti, F., Gens Solé, A., 2015. An approach to enhance efficiency of DEM modelling of soils with crushable grains. *Géotechnique*. 65, 91-110.

Ciantia, M. O., Arroyo, M., Butlanska, J., Gens, A., 2016. DEM modelling of cone penetration tests in a double-porosity crushable granular material. *Computers and Geotechnics*. 73, 109-127.

Coetzee, C., 2016. Calibration of the discrete element method and the effect of particle shape. *Powder Technology*. 297, 50-70.

Coetzee, C. J., 2017. Review: Calibration of the discrete element method. *Powder Technology*. 310, 104-142.

Cundall, P. A., Strack, O. D., 1979. A discrete numerical model for granular assemblies. *geotechnique*. 29, 47-65.

Davidson, M. T., Chung, J. H., Teng, H., Han, Z., Le, V., 2015. Volume-Averaged Stress States for Idealized Granular Materials using Unbonded Discrete Spheres in LS-DYNA®. *10th European LS-DYNA Conference*, Würzburg, Germany.

de Bono, J., McDowell, G., Wanatowski, D., 2015. Investigating the micro mechanics of cemented sand using DEM. *International Journal for Numerical and Analytical Methods in Geomechanics*. 39, 655-675.

Evans, T. M., Valdes, J. R., 2011. The microstructure of particulate mixtures in one-dimensional compression: numerical studies. *Granular Matter*. 13, 657-669.

Feng, Y., Owen, D., 2014. Discrete element modelling of large scale particle systems—I: exact scaling laws. *Computational Particle Mechanics*. 1, 159-168.

Forsström, D., Jonsén, P., 2016. Calibration and validation of a large scale abrasive wear model by coupling DEM-FEM: Local failure prediction from abrasive wear of tipper bodies during unloading of granular material. *Engineering Failure Analysis*. 66, 274-283.

Gabrieli, F., Cola, S., Calvetti, F., 2009. Use of an up-scaled DEM model for analysing the behaviour of a shallow foundation on a model slope. *Geomechanics and Geoengineering: An International Journal*. 4, 109-122.

González-montellano, C., Fuentes, J., Ayuga-téllez, E., Ayuga, F., 2012. Determination of the mechanical properties of maize grains and olives required for use in DEM simulations. *Journal of Food Engineering*. 111**,** 553-562.

Jaksa, M. B., Scott, B. T., Mentha, N., Symons, A., Pointon, S., Wrightson, P., Syamsuddin, E., 2012. Quantifying the zone of influence of the impact roller. *ISSMGE-TC 211 International Symposium on Ground Improvement IS-GI Brussels*, 30 May – 1 June, Vol. 2, pp. 41–52.

Jiang, M., Dat, Y., Cui, L., Shen, Z., Wang, X., 2014. Investigating mechanism of inclined CPT in granular ground using DEM. *Granular Matter*. 16, 785-796.

Jing, X. Y., Zhou, W. H., Zhu, H. X., Yin, Z. Y., Li, Y., 2018. Analysis of soil-structural interface behavior using three-dimensional DEM simulations. *International Journal for Numerical and Analytical Methods in Geomechanics*, 42, 339-357.

Kim, K., 2011. Numerical simulation of impact rollers for estimating the influence depth of soil compaction. Dissertation in partial fulfilment of the requirements for the degree of Master of Science, Texas A & M University.

Kuo, Y., Jaksa, M., Scott, B., Bradley, A., Power, C., Crisp, A., Jiang, J., 2013. Assessing the effectiveness of rolling dynamic compaction. *Proceedings of the 18th*

International Conference on Soil Mechanics and Geotechnical Engineering, Paris., pp. 1309–1312.

Lei, Z., Zang, M., 2010. An approach to combining 3D discrete and finite element methods based on penalty function method. *Computational Mechanics*. 46, 609-619.

LSTC., 2018. LS-DYNA KEYWORD USER'S MANUAL. Livermore, California: Livermore Software Technology Corporation, ISBN: 0-9778540-2-7.

Majmudar, T. S., Behringer, R. P., 2005. Contact force measurements and stress-induced anisotropy in granular materials. *Nature*. 435, 1079-1082.

Mayne, P. W., Jones Jr, J. S., Dumas, J. C., 1984. Ground response to dynamic compaction. *Journal of Geotechnical Engineering*. 110, 757-774.

Muthuswamy, M., Tordesillas, A., 2006. How do interparticle contact friction, packing density and degree of polydispersity affect force propagation in particulate assemblies? *Journal of Statistical Mechanics: Theory and Experiment*. 2006, P09003.

Nakashima, H., Oida, A., 2004. Algorithm and implementation of soil–tire contact analysis code based on dynamic FE–DE method. *Journal of Terramechanics.* 41, 127-137.

Ranjan, G., Rao, A., 2007. *Basic and applied soil mechanics*. New Age International.

Scott, B., Jaksa, M., 2014. Evaluating rolling dynamic compaction of fill using CPT. *Proceedings of the 3rd International Symposium on Cone Penetration Testing*, pp. 941-948.

Scott, B., Jaksa, M., Mitchell, P., 2019a. Depth of influence of rolling dynamic compaction. *Proceedings of the Institution of Civil Engineers-Ground Improvement*. 1-10.

Scott, B., Jaksa, M., Mitchell, P., 2019b. Ground response to rolling dynamic compaction. *Géotechnique Letters*. 9, 99-105.

Scott, B., Jaksa, M., Syamsuddin, E., 2016. Verification of an impact rolling compaction trial using various in situ testing methods. *Proc. of 5th Int. Conf. on Geotechnical and Geophysical Site Characterisation*.

Scott, B. T., Jaksa, M. B., Mitchell, P. W., 2020. Influence of towing speed on effectiveness of rolling dynamic compaction. *Journal of Rock Mechanics and Geotechnical Engineering*. 12, 126-134.

Thakur, M. M., Penumadu, D., 2020. Triaxial compression in sands using FDEM and micro-X-ray computed tomography. *Computers and Geotechnics*. 124, 103638.

Xu, W., Zend, H., Yang, P., Zang, M., 2020. Numerical analysis on tractive performance of off-road tire on gravel road using a calibrated finite element method–discrete element method model and experimental validation. *Proceedings of the Institution of Mechanical Engineers, Part D: Journal of Automobile Engineering*. 234, 3440-3457.

Yang, P., Zang, M., Zeng, H., 2019. DEM–FEM simulation of tire–sand interaction based on improved contact model. *Computational Particle Mechanics*. 1-15.

Zeng, H., Xu, W., Zang, M., Yang, P., 2020. Calibration of DEM-FEM model parameters for traction performance analysis of an off-road tire on gravel terrain. *Powder Technology*. 362, 350-361.

Zhang, N., Arroyo, M., Ciantia, M. O., Gens, A., Butlanska, J., 2019. Standard penetration testing in a virtual calibration chamber. *Computers and Geotechnics*. 111, 277-289.

Zhou, Q., Xu, W.-J., Lubbe, R., 2021. Multi-scale mechanics of sand based on FEM-DEM coupling method. *Powder Technology*. 380, 394-407.

Chapter 5.

A parametric study of the 4-sided impact roller

Statement of Authorship

Title of Paper	A parametric study of the 4-sided impact roller.
Publication Status	☐ Published ☐ Accepted for Publication ☑ Submitted for Publication ☐ Unpublished and Unsubmitted w ork w ritten in manuscript style
Publication Details	Chen, Y., Jaksa, M., Scott, B., Kuo, Y. 2021. A parametric study of the 4-sided impact roller. Acta Geotechnica, Submitted for Review

Principal Author

Name of Principal Author (Candidate)	Yue Chen
Contribution to the Paper	Developed the numerical model, contributed to methodology, analysis and interpretation of the data, wrote manuscript.
Overall percentage (%)	80%
Certification:	This paper reports on original research I conducted during the period of my Higher Degree by Research candidature and is not subject to any obligations or contractual agreements with a third party that would constrain its inclusion in this thesis. I am the primary author of this paper.
Signature	Date: 08 October 2021

Co-Author Contributions

By signing the Statement of Authorship, each author certifies that:

i. the candidate's stated contribution to the publication is accurate (as detailed above);
ii. permission is granted for the candidate in include the publication in the thesis; and
iii. the sum of all co-author contributions is equal to 100% less the candidate's stated contribution.

Name of Co-Author	Mark Jaksa
Contribution to the Paper	Provided primary supervision, initial concept, contributed to the methodology, helped evaluate and edit the manuscript.
Signature	Date: 12/10/21

Name of Co-Author	Brendan Scott
Contribution to the Paper	Provided secondary supervision, assisted with research direction, helped edit the manuscript.
Signature	Date: 12/10/2021

Please cut and paste additional co-author panels here as required.

Name of Co-Author	Yien Lik Kuo		
Contribution to the Paper	Provided secondary supervision, contributed to the methodology, helped edit the manuscript.		
Signature		Date	08 Oct 2021

Please cut and paste additional co-author panels here as required.

A parametric study of the 4-sided impact roller (Paper 4)

Abstract

Rolling dynamic compaction (RDC) is a specific type of dynamic compaction, which involves towing a heavy non-circular module at relatively constant speed. This paper investigates the effects of module mass, operating speed and varying ground conditions on the effectiveness of the 4-sided impact roller using a developed finite element method (FEM)-discrete element method (DEM) model. Numerical results were analysed from four aspects, namely the energy imparted to the ground, soil velocity vectors, module imprint lengths and soil displacements at different depths. It is found that, a heavier module mass induces greater ground improvement in terms of both energy delivered to the soil per impact and the magnitude of soil displacements. The energy imparted to the underlying soil by the module increases with greater operating speed. The rotational dynamics of the module also change with increasing operating speed, whereby the impacts are delivered by the face of the module at typical operating speeds; however, at faster speeds the impacts are delivered towards the corners of the module and the behaviour is less reproducible. The modelling showed that soil with a higher initial Young's modulus and a higher internal angle of friction decreases the magnitude of soil displacements, which confirms that the impact roller is less able to significantly improve soils that are stiff or have a high initial shear strength.

5.1 Introduction

With the growing demand for infrastructure development, there is an increasing need to construct on sites, which were previously considered to be difficult or unsuitable. In order to facilitate construction, soils at marginal sites typically require improvement. Compaction is the most frequently used method to improve the ground mechanically, as it is both efficient and cost-effective. Rolling dynamic compaction (RDC), is a specific

type of dynamic compaction, which involves towing a heavy non-circular module at relatively constant speed. As it is towed, the module rotates and falls to impact the ground dynamically, whereby both potential and kinetic energies are imparted to the underlying soil during this process. RDC has been applied successfully in various ground improvement contexts, such as, civil and mining projects, land reclamation projects and highway rehabilitation (Avalle and Carter, 2005; Avalle and McKenzie, 2005; Bouazza and Avalle, 2006). Although RDC has been employed in several projects, as reported by Scott and Jaksa (2008), there are situations, after compaction, in which the soil did not meet the expected requirements. A key reason why it is not more widely used, is that the use of RDC is based, to a large extent, on previous experience in similar ground conditions (Scott and Jaksa, 2008). Therefore, there is a need to investigate factors that affect the performance of RDC and then provide practical recommendations for applications of RDC.

The effectiveness of RDC is mainly affected by three aspects: the ground conditions, RDC operation and the characteristics of RDC module. Scott et al. (2019) reported that the effective depth of influence of RDC is affected by the soil conditions and the operating speed. A greater effective depth of influence is achieved in coarse soil and at a faster operating speed. Scott et al. (2020) examined the influence of RDC operating speed (5–15 km/h) using buried earth pressure cells (EPCs) in field tests. It was found that the recorded peak pressure increased as the operating speed grew from 5 to 12 km/h, and the peak pressure reduced at operating speed greater than 12 km/h. They also reported that a greater energy was imparted by RDC at faster operating speeds. Previous studies on the effectiveness of RDC were mainly conducted in the field and over several years (Avalle and Carter, 2005; Jaksa et al., 2012; Scott and Jaksa, 2014; Scott et al., 2016; Jaksa et al., 2019). Whilst there are many benefits of conducting field tests, they are expensive

because they require a significant amount of time and effort to prepare and carry out the field tests. Measurement and instrumentation is usually complex and provides limited insights into the performance of RDC. In addition, homogeneous soils need to be employed in the field tests in order to quantify the effect of a single factor on the ground improvement results and also to ensure the accuracy of test results. The influence of the operation of RDC and the characteristics of RDC module, such as the operating speed, the number of RDC passes, and the weight and the shape of RDC module are easier to assess since these are factors that can be controlled by the RDC operator. However, the effects of site conditions on the performance of RDC are difficult to be assessed in field tests since ground conditions, such as the type, the initial dry density and the particle size range of the soil are site-specific, complex and difficult to control in field tests.

Since conducting field tests suffers from several disadvantages, as mentioned above, an alternate approach, which is capable of assessing factors that influence the effectiveness of RDC, is highly desirable. In recent years, numerical modelling has been successfully adopted by several researchers to investigate the performance of RDC (Kuo et al., 2013; Bradley et al., 2019; Chen et al., 2021). Based on their studies, it can be concluded that the developed numerical models provide reasonable predictions of ground improvement due to RDC and the effectiveness of RDC is able to be quantified based on the numerical results. In addition, parameters that affect the soil properties can be varied and controlled with relative ease in a numerical model, which facilitates enhanced understanding of the effects of these parameters on the ground improvement results.

By the use of a numerical model developed by Chen et al. (2021), this study seeks to explore the influence of module mass, operating speed and varying ground conditions on the performance of a 4-sided impact roller. The numerical model is used to quantify the

energy imparted to the ground, soil velocity vectors, module imprint lengths and soil displacements at different depths, and these are used to study the effectiveness of RDC with different module weights, at various operating speeds and in different ground conditions, as is discussed below.

5.2 Numerical model

The numerical RDC scale model adopted in this study was developed by Chen et al. (2021) using the LS-DYNA computer application (LSTC 2018). The model consists of a simplified 1:13 scaled roller module, a chamber filled with soil particles and two rigid frames at each end of the chamber, as shown in Figure 5.1. The scaled roller module, the chamber and two frames are simulated using the finite element method (FEM), while the soil particles are simulated using the discrete element method (DEM). The chamber and two frames are modelled as rigid materials and fixed at their initial locations in the model, with no displacement or deformation during the roller compaction process. The scaled module is a 1:13 scale replica of the Broons' 4-sided impact roller and the properties of the scaled module are calculated according to scaling laws proposed by Altaee and Fellenius (1994) [Equations (5.1)–(5.5)]. The roller module is modelled as a rigid body with no deformation during compaction, since the roller is relatively rigid compared with the stiffness of the soil (Kuo et al., 2013; Bradley et al., 2019). The size of the chamber is 600 × 280 × 125 mm (length × width × height) to accommodate the 1:13 scaled module with dimensions of 115 × 100 × 115 mm (length × width × height). The actual soil particles are simulated as rigid spheres with soft contacts, which implies that the particles are permitted to overlap at the contacts. The contact forces between particles are evaluated using a contact model. In Chen et al. (2021), the linear contact model was adopted, since it is simple, reliable and efficient. The linear contact model contains two linear elastic springs in the normal and shear directions with constant normal (k_n) and shear (k_s)

stiffnesses, respectively; two viscous damping dashpots in the normal and shear directions with normal (β_n) and shear (β_s) damping ratios, respectively; and a frictional slip in the shear direction with a coefficient of friction, μ. Input parameters of the linear contact model were calibrated through numerical triaxial tests to ensure the numerical particles exhibit similar macroscopic behaviour to the actual soil particles. In addition, the rotation of the numerical particles was prohibited to simulate the irregular shape of soil particles and increase the macroscopic shear strength of the numerical particles (Calvetti et al., 2003; Calvetti et al., 2004; Gabrieli et al., 2009). In the numerical model, soil particles were generated to fill an enclosed box and then fell into the chamber under gravity from a relatively constant height.

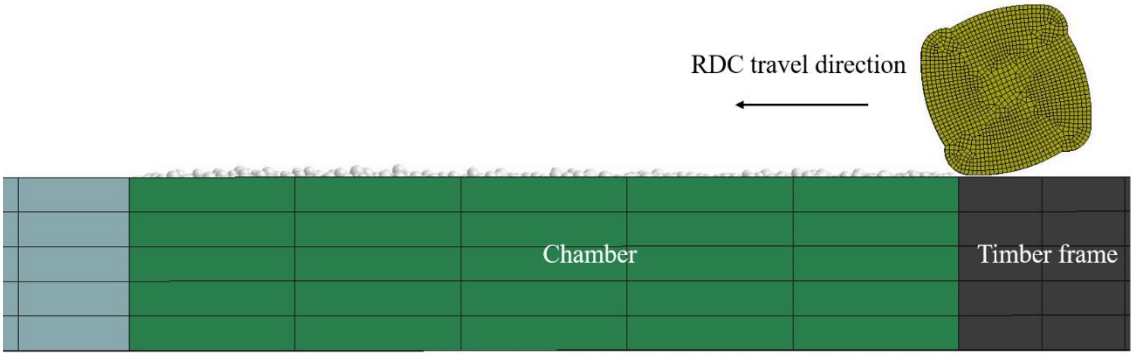

Figure 5.1. Numerical model setup.

The developed numerical scale model was validated against results obtained from field tests conducted by Scott et al. (2016). The numerical results were upscaled based on the scaling laws developed by Altaee and Fellenius (1994) [Equations (5.6)–(5.8)]. The upscaled numerical results were then compared against field data obtained from the same soil properties using a full-size RDC module. It was concluded that, the upscaled numerical results were in good agreement with the field data and the numerical scale model was demonstrated to be able to simulate reliably the behaviour of the full-size RDC

model. Consequently, the numerical scale model can be used to provide practical recommendations for the application of the full-size RDC module.

$$\frac{L_m}{L_p} = n \tag{5.1}$$

$$\frac{V_m}{V_p} = n^3 \tag{5.2}$$

$$\frac{M_m}{M_p} = n^3 \tag{5.3}$$

$$\frac{T_m}{T_p} = 1 \tag{5.4}$$

$$\frac{S_m}{S_p} = n \tag{5.5}$$

$$\frac{D_m}{D_p} = n \cdot \frac{\frac{\Delta e_m}{1+e_{0m}}}{\frac{\Delta e_p}{1+e_{0p}}} \tag{5.6}$$

$$\frac{\sigma_m}{\sigma_p} = \exp\left(\frac{e_{0p}-e_{0m}}{\lambda}\right) \tag{5.7}$$

$$\frac{E_m}{E_p} = \exp\left(\frac{e_{0p}-e_{0m}}{\lambda}\right) \times n^3 \tag{5.8}$$

where L is the characteristic length; V and M are the volume and mass of the roller module, respectively; T is the operating time; S is the operating speed; D is the vertical displacement; σ is the imposed stress; E is the energy imparted by the module; e_0 is the initial void ratio; Δe is the change in void ratio; λ is the slope of the critical state line in the e – log σ plane; n is the geometric scale ratio (1/13); and the subscripts m and p denote the scale model and prototype (i.e. the full-size module), respectively.

The soil used in this study is the same as that adopted by Chen et al. (2021), therefore, the DEM input parameters calibrated by Chen et al. (2021) are used. In addition, similar to Chen et al. (2021), in the numerical RDC tests, due to the computational and time constraints, the particles are upscaled to be 3.5 times greater than the particle size used in the calibration triaxial tests. The calibrated DEM input parameters were then upscaled

using the mass scaling law developed by Gabrieli et al. (2009). The upscaled DEM input parameters are shown in Table 5.1, and these are the input parameters used in numerical RDC tests in this study.

Table 5.1. DEM input parameters used in numerical RDC tests.

Parameter	Value
Particle density (kg/m^3)	2,620
Particle diameter (mm)	3.5–10.5
Coefficient of friction (μ)	0.25
Normal and shear stiffnesses (k_n and k_s) (N/m)	2.275 ×10^6
Normal and shear damping ratios (β_n and β_s)	0.1

Two different weights (3.64 and 5.46 kg) of 4-sided scale modules are studied, which represent the 8- and 12-tonne impact rollers (Broons BH-1300 and BH-1300 HD), respectively. Operating speeds of 192, 214, 235, 256, 278, 299 and 321 mm/s, corresponding to the full-size operating speeds of 9, 10, 11, 12, 13, 14 and 15 km/h, respectively, are evaluated. The matrix of numerical simulations, which investigates the effects of module weight and operating speed, is shown in Table 5.2. Each simulation consists of 5 module passes. As with Chen et al. (2021), the numerical simulations are performed using a University of Adelaide's supercomputer (2 × Intel Xeon Gold 6248 Processor @2.4 GHz) using the ANSYS (LS-DYNA) software. Due to ANSYS license constraints, 12 CPU cores were used for these simulations. Typically, each simulation took approximately 5 days to run. The influence of varying the ground conditions on RDC performance is presented later in the paper.

Table 5.2. Simulation matrix.

Simulation no.	Scaled module weight (kg)	Full-size module weight (tonne)	Scaled module operating speed (mm/s)	Full-size module operating speed (km/h)
1	5.46	12	235	11
2	3.64	8	235	11
3	3.64	8	192	9
4	3.64	8	214	10
5	3.64	8	256	12
6	3.64	8	278	13
7	3.64	8	299	14
8	3.64	8	321	15

5.3 Module weight

Simulations 1 and 2 are conducted to assess the effect of module weight on the ground improvement results. The energy imparted to the ground by a single module impact is an important indicator of the effectiveness of RDC (Scott and Jaksa, 2008; Li et al., 2020). LS-DYNA provides the energy imparted by the module during compaction process based on the motion of the module. In the numerical model, horizontal and initial rotational speeds of the module are defined, and the vertical speed is calculated by the model according to the defined horizontal and initial rotational speeds, the soil properties and the undulating surface left by previous module impacts. It is worth restating that the numerical simulations are conducted using the 1:13 RDC scaled module and the numerical results need to be upscaled to replicate the field data. Therefore, the energy scaling factor [Equation (5.8)] is used to upscale the numerical results. The initial void ratio of the soil in the numerical model is approximately 0.764, and the average initial void ratio of the soil in the field tests was reported as 0.52 (Scott et al. 2016). Consistent

with Chen et al. (2021), $\lambda = 0.11$ is adopted in this study. The energy results are interrogated from several module impacts from Simulations 1 and 2 and then upscaled using the energy scaling factor [Equation (5.8)]. As a consequence, it is determined, with 95% confidence, that the 8- and 12-tonne modules deliver approximately 24 ± 3 and 35 ± 4 kJ to the soil per impact, respectively, for an operating speed of 11 km/h.

Velocity vectors of soil particles directly reflect the soil's response to the influence of RDC. Figures 5.2 and 5.3 display velocity vectors of soil particles as a result of RDC for both the 8- and 12-tonne modules. In general, it can be seen that the overall soil displacement pattern induced by the 8-tonne module is similar to that of the 12-tonne module. By comparing the two, the heavier module (i.e. 12-tonne) induces larger velocity vectors before and after the module's impact, which is evidenced by Figures 5.2b and 5.3b. In addition, the 12-tonne module has a greater influence region, which means more soil particles are affected by the heavier module, as one might expect. This is again shown by the velocity vectors observed at deeper depths and greater lengths from the contact point between the module and the soil in Figures 5.2b and 5.3b.

As indicated by the soil movements in Figures 5.2 and 5.3, the energy imparted to soil as a consequence of RDC dissipates in all directions (i.e. spread from top to bottom and from the centre of impact to both sides). This phenomenon was also reported by Li et al. (2020), who stated that the energy induced by a 3-sided RDC module dissipates in all directions based on particle movements captured by a high-speed camera.

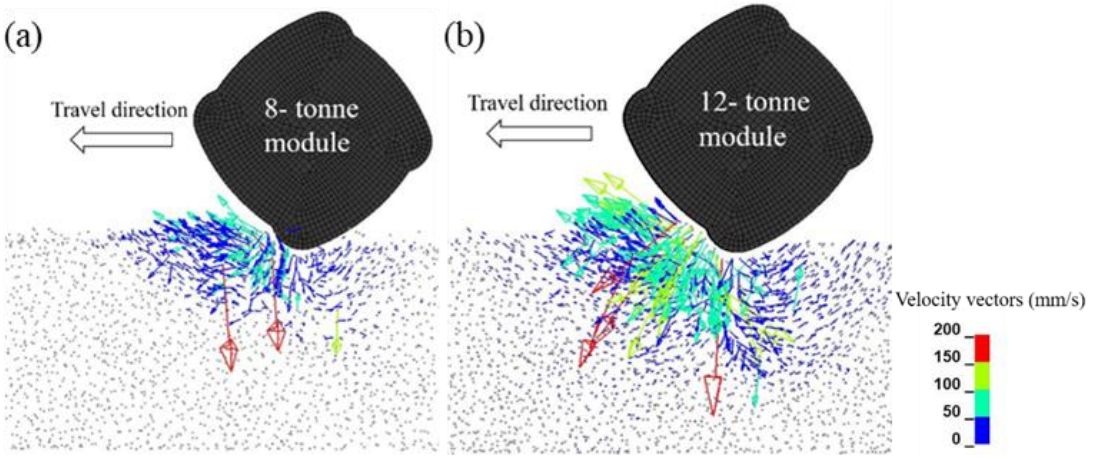

Figure 5.2: Velocity vectors of soil particles before the module's impact: (a) 8-tonne module, (b) 12-tonne module.

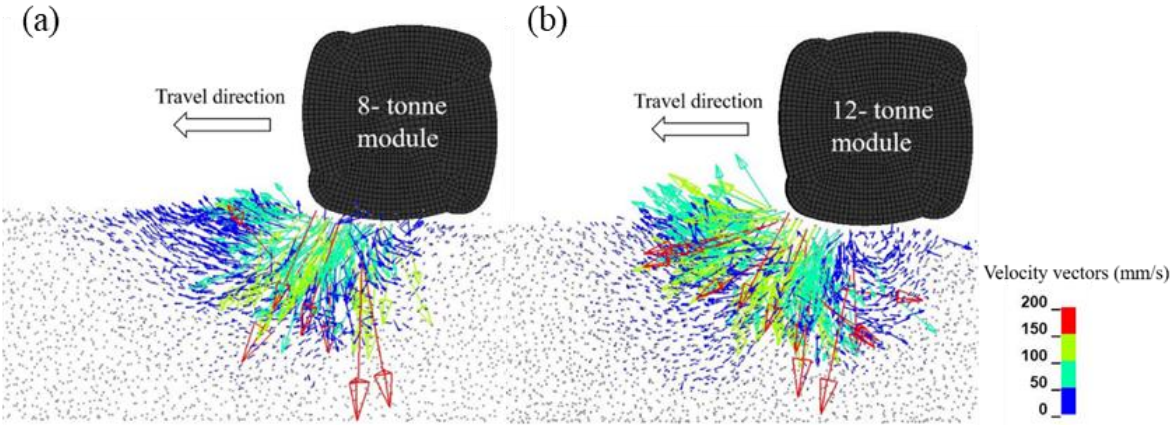

Figure 5.3: Velocity vectors of soil particles just after the module's impact: (a) 8-tonne module, (b) 12-tonne module.

In general, from the numerical results, it can be concluded that, the 12-tonne module achieves greater efficacy in compacting the ground when compared with the 8-tonne module, in terms of imparting a greater amount of energy to the ground and inducing larger soil displacements. However, in practice, the decision between using an 8- or 12-tonne module is often made based on several other factors. For example, the heavier module induces greater ground vibrations, which may result in the need for a greater buffer zone to settlement sensitive infrastructure to minimise the effects of vibrations. A field trial is recommended before the actual application to assess the effects of ground vibrations to nearby structures. In addition, the heavier module is less mobile than the

lighter one, which adds to the cost of transporting and operating the module. The heavier module also imposes greater surface pressures and may be a more marginal option at traversing the ground surface at sites containing loose sands, or soft clays, or where the water table may be close to the surface. Therefore, the choice between the 8- and 12-tonne modules should be made by giving due consideration to all of these factors.

5.4 Operating speed

Simulations 3-8 were conducted and the results of Simulations 2-8 are analysed to investigate the influence of operating speed on the performance of RDC. The energy delivered to the ground is again adopted as a measure of the effectiveness of RDC. As stated in the previous section, the energy imparted to the soil from LS-DYNA is interrogated from several module impacts and then upscaled. Table 5.3 shows the summary of the energy imparted per module impact with varying operating speed. In general, the energy increases with faster operating speeds. Bradley et al. (2019) quantified the energy delivered by RDC by analysing the motion of the 4-sided module from a field test using high-speed photography. The authors concluded that the energy imparted by the module per impact was reported as 23 ± 4 kJ at an operating speed of 10 km/h, which is consistent with the energy results obtained in the present study. In addition, Table 5.4 presents the energy imparted to the ground per module impact for operating speeds between 9–12 km/h reported by Scott et al. (2020). From Table 5.4, it again shows that the imparted energy increases with greater operating speed. It can be further seen that the energy results obtained by Scott et al. (2020) are slightly greater than those from the results of the numerical simulations in the present study. The reason is that energies delivered to the soil reported by Scott et al. (2020) are the theoretically possible maximum values, and these values may not be imparted to the ground at each module impact, since the ground conditions vary at each site and this affects the full delivery of potential energy.

Table 5.3. Energy imparted by the module at different operating speeds with 95% confidence.

Operating speed (km/h)	9	10	11	12	13	14	15
Energy absorbed by the ground per module impact (kJ)	21 ± 2	22 ± 2	24 ± 3	26 ± 3	30 ± 3	32 ± 4	33 ± 4

Table 5.4. Energy imparted by the module at operating speeds between 9 to 12 km/h (Scott et al., 2020).

Operating speed (km/h)	9	10	11	12
Energy imparted per module impact (kJ)	22	25	27	30

Operating speed not only affects the amount of energy delivered to the underlying soil, but also influences the way that the energy is imparted to the ground. Clifford (1980) stated that the 4-sided roller can deliver sufficient energy to the ground, per impact blow, when the operating speed is within the range of 9–12 km/h. At operating speeds slower than this range, may result in sliding of the module on the ground, since the roller has insufficient momentum to keep the module rotating. Again, according to Clifford (1980), when the operating speed is greater than this range, the module starts to skip on the ground and the energy is delivered by the corners rather than the faces of the module. Avalle et al. (2009) and Scott et al. (2020) reported the same phenomenon. Scott et al. (2020), further confirmed these findings by measuring the spacing between contact imprints left on the ground after each impact. The authors stated that, when the operating speed is within the recommended range, the energy is delivered by the face of the module, the imprints left on the ground are relatively uniform and the spacings between them are approximately equal to the length of the module's face (i.e. 1,450 mm). At higher speeds than those recommended, the module tends to skip on the ground from corner to corner,

the imprints become non-uniform, and the spacings between them varies within a wide range and they are generally greater than the module face length. Therefore, the module imprint lengths on the ground are measured in the numerical simulations and upscaled using Equation (5.1) in order to compare them with those of Scott et al. (2020).

As illustrated in Figure 5.4, the module imprint length shows an increasing trend as the operating speed grows. As indicated, the solid line represents the length of the module's face (1,450 mm). The cross symbols in Figure 5.4 represent the average of the imprint lengths obtained from around ten module impacts from the numerical simulations. It can be seen that the average of the module imprint lengths obtained from speeds of 9–11 km/h are smaller than the module face length due to insufficient kinetic energy of the roller module. On the other hand, the average module imprint length is greater than the module face length at an operating speed of 15 km/h, due to the erratic movements of the module at higher speeds. For speeds between 12 to 14 km/h, the average module imprint lengths are close to the module face length. The trend of the changes of module imprint length with respect to the operating speed is similar to that reported by Scott et al. (2020). However, Scott et al. (2020) found that the imprint length is greater than the module face length at speeds greater than 13 km/h. This discrepancy is likely due to the following two reasons. Firstly, the soil properties in the numerical model and the field tests, such as soil grading, particle sizes and initial relative density, are not identical, and the soil was simulated as spherical particles in the numerical models, while the soil used in the field tests was angular in shape. Furthermore, Kim (2011) reported that the roller skipped on the ground with stiff soils at a speed of 10 km/h, which indicates that the operating speed also depends on the soil conditions. Secondly, the double-spring-linkage system which is incorporated in the full-sized module may increase the likelihood of the module skipping behaviour. On the other hand, the discrepancy confirms the observation reported by Scott

et al. (2020) that the recommended operating speed should be varied based on the site-specific ground conditions.

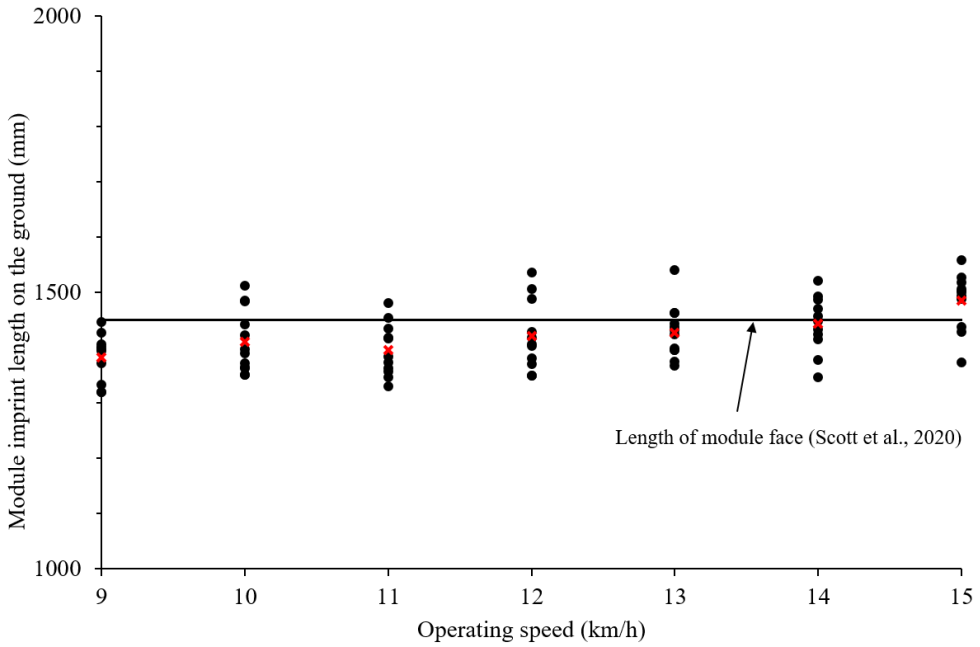

Figure 5.4: Module imprint lengths at each operating speed obtained from numerical simulations. (Red cross indicates the average of the module imprint lengths.)

Based on the numerical results, it is concluded that the operating speed influences the energy imparted to the ground and the behaviour of the RDC module. The effect of operating speed on the performance of RDC also depends on the site conditions. Based on the results of module imprint lengths in Figure 5.4, an operating speed range between 10 to 14 km/h is recommended. However, this suggested operating speed range needs to be further verified by field trials, since the operating speed also causes wear-and-tear on the mechanical components and discomfort for operator. As reported by Avalle et al. (2009), speeds above 12 km/h may result in an uncomfortable ride for the operator and may induce damage to the module frame. In addition, there are some sites that contain several small working areas and, in such situations, the operating speed of the roller is difficult to be maintained within the typical range (Scott et al., 2020). In general,

conducting a field trial is encouraged prior to the actual tests to examine whether the recommended operating speed range can be achieved and used at each particular site.

5.5 Ground conditions

5.5.1 Relationships between the microscopic parameters and macroscopic properties of soil

As mentioned above, the linear contact model was adopted to describe the interaction between the particles in the numerical model. Five input parameters are required in the linear contact model, namely normal and shear stiffnesses, normal and shear damping ratios and the coefficient of friction. According to Chen et al. (2021), for quartzose materials, the ratio between the normal and shear stiffnesses is unity and the damping ratios are 0.1. Therefore, the numerical macroscopic behaviours of the soil particles are mainly affected by the contact stiffness (normal and shear stiffnesses) and the coefficient of friction, if the initial porosity and particle size remain constant.

The relationships between DEM input parameters (contact stiffness and coefficient of friction) and soil macroscopic behaviour are obtained by conducting several numerical triaxial tests, with one input parameter being changed in-turn, while the others remain constant. As mentioned above, the soil used in this study is the same as that adopted by Chen et al. (2021), therefore, similar to Chen et al. (2021), the numerical particles used in numerical triaxial tests were generated with diameters between 1 and 3 mm. The triaxial test sample had a diameter of 50 mm and a height of 100 mm. Similar to the experimental triaxial tests, the numerical triaxial simulations incorporated three stages. Firstly, the DEM particles were generated randomly to fill an enclosed cylinder and then fell under gravity from a constant height. The top loading cap moved up and down to compact particles to help them settle and to match the experimental porosity. After all

particles reached a static and steady state, the target confining pressure was then applied during the second stage. In the third stage, the axial strain was increased by displacing the top plate vertically at a constant velocity (10 mm/s in this study), and the confining pressure was maintained at the same time.

In order to investigate the effects of contact stiffness on the macroscopic behaviour of the soil, several numerical triaxial simulations were conducted at a confining pressure of 250 kPa with a contact stiffness varied from 450 to 1050 kN/m, while maintaining the coefficient of friction constant at 0.25 in all simulations. In general, it can be seen from Figure 5.5 that the value of the contact stiffness has a significant influence on the slope of the stress-strain curves. The peak deviatoric stress is less affected by the contact stiffness. The influence of the contact stiffness on the slope of the stress-strain curves shows a decreasing trend when the value of contact stiffness increases to a certain value. In other words, the contraction of sample during the triaxial tests is affected by the variation of contact stiffness. As the contact stiffness increases, the value and the duration of the compression of the sample gradually reduces, whereas the contact stiffness has less influence on the dilatancy of the sample. The same phenomenon was observed by Plassiard et al. (2009), Gabrieli et al. (2009), Tapias et al. (2011) and Marczewska et al. (2016). They performed a series of numerical DEM triaxial tests and reported that, the initial slope of the stress-strain curves increases with the increasing contact stiffness values for lower values of contact stiffness. In terms of higher contact stiffness values, the effect of contact stiffness on the initial slope of the stress-strain curves is very small.

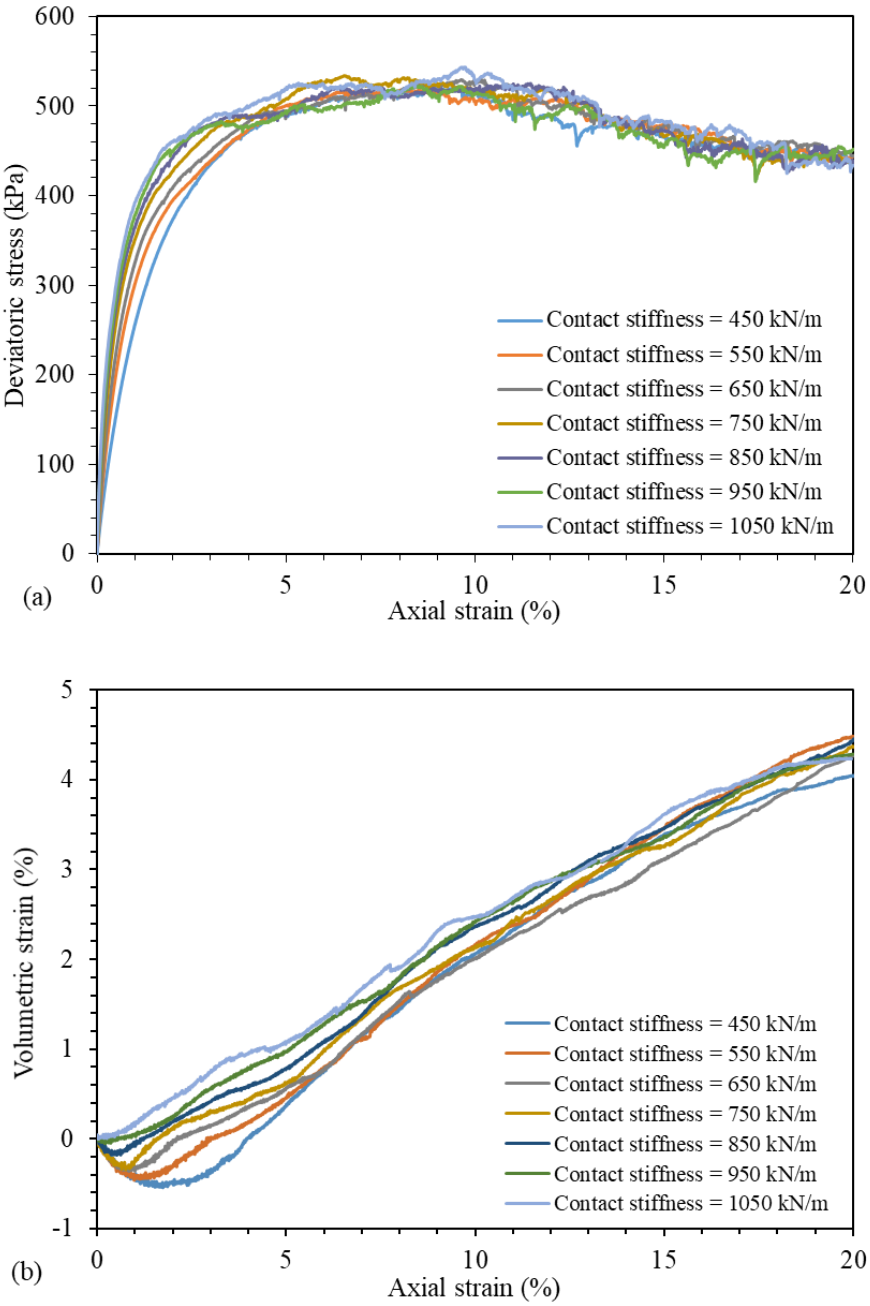

Figure 5.5: Triaxial tests at a confining pressure of 250 kPa with different contact stiffness values: (a) stress-strain curves; (b) volumetric curves.

According to Plassiard et al. (2009) and Wang and Li (2014), the initial Young's modulus (E), Poisson's ratio (v) and the internal angle of friction (φ) can be determined from the stress-strain curves, as shown in Figure 5.6. The effect of Poisson's ratio on the soil macroscopic behaviour is not investigated in this study, since Poisson's ratio is the ratio between the soil's lateral and longitudinal strains and it mainly relates to soil deformation behaviour. In this study, the soil particles are placed in a chamber and the horizontal

deformation of the soil is constrained by the chamber. Therefore, the effect of Poisson's ratio is difficult to investigate.

Based on Figure 5.6, it can be seen from Figure 5.5 that the soil's initial Young's modulus increases with rising contact stiffness and the peak stress value is not affected by the variation of contact stiffness. In this study, the effect of contact stiffness on the initial Young's modulus is examined since the soil's stiffness is directly related to soil displacement and the performance of the impact roller. Figure 5.7 shows the relationship between the DEM input contact stiffness value and the soil's initial Young's modulus, and an almost linear relationship is observed. Therefore, the maximum and minimum values of contact stiffness (1050 and 450 kN/m), which correspond to a soil's initial Young's modulus of approximately 69 and 25 MPa, respectively, are adopted in the numerical RDC simulations that follow.

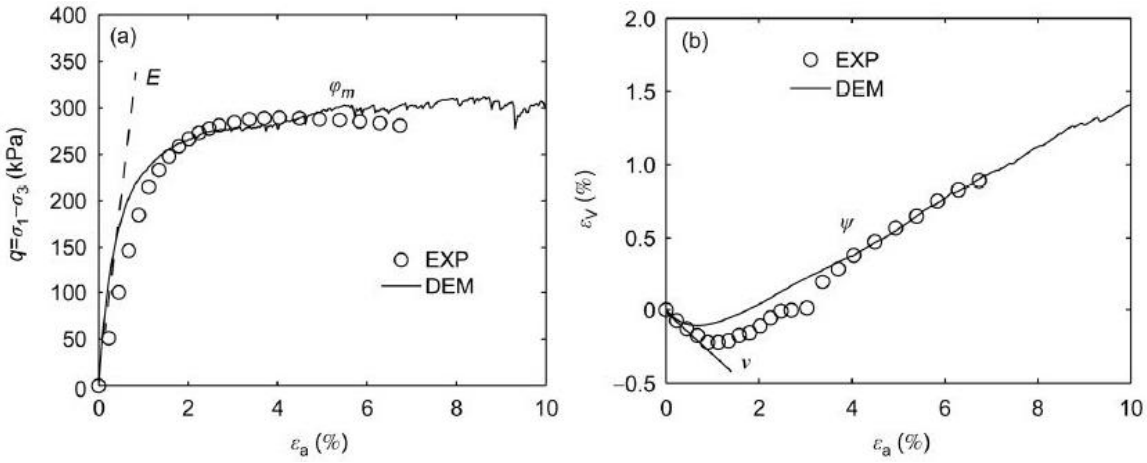

Figure 5.6: Soil properties obtained from triaxial tests (Wang and Li, 2014).

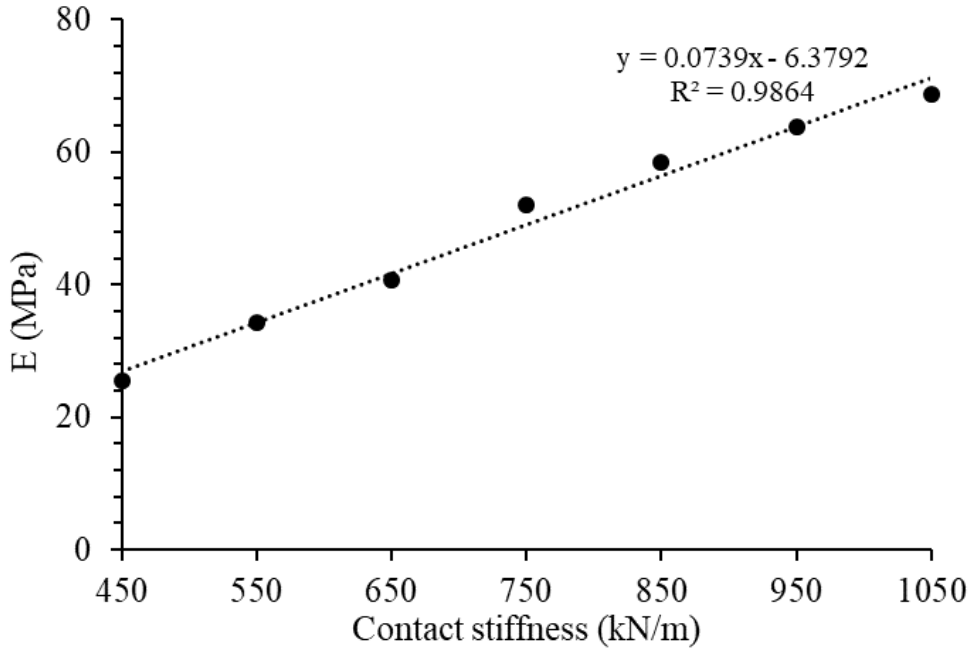

Figure 5.7: The effect of contact stiffness on the soil's initial Young's modulus.

A similar process was performed to investigate the effect of the coefficient of friction on the macroscopic stress-strain behaviour of the soil. A series of numerical triaxial simulations were conducted at a confining pressure of 250 kPa with a coefficient of friction varying from 0.23 to 0.27, while the contact stiffness was maintained constant at 650 kN/m. The results of the numerical triaxial simulation with various coefficients of friction are shown in Figure 5.8. It can be seen that the soil's elastic response is not affected by the variation in the coefficient of friction. The values of peak stress and soil dilatancy response increase with rising coefficient of friction. In terms of the soil's macroscopic parameters, the coefficient of friction has a negligible effect on the initial Young's modulus and Poisson's ratio. The internal angle of friction and the dilatancy angle show an increasing trend as the coefficient of friction increases. These are consistent with the findings from Coetzee and Els (2009), Gabrieli et al. (2009), Kozicki and Tejchman (2009) and Wang and Li (2014). They stated that the increase in coefficient of friction results in the internal angle of friction increasing, while the soil elastic response is not affected by changes in the coefficient of friction.

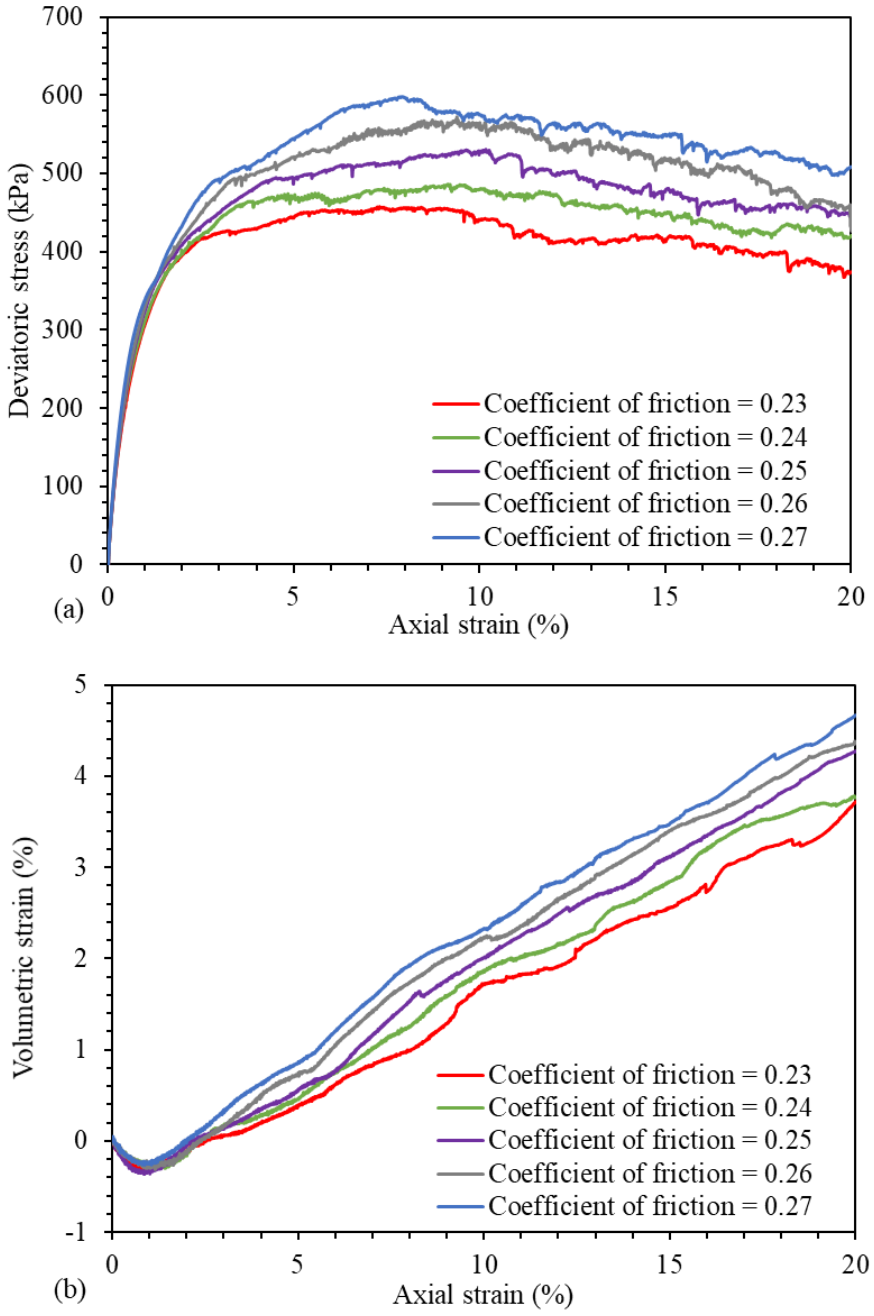

Figure 5.8: Triaxial tests at a confining pressure of 250 kPa with different coefficient of friction values: (a) stress-strain curves; (b) volumetric curves.

In order to obtain the Mohr-Coulomb failure envelope to evaluate the soil internal angle of friction, numerical triaxial simulations were conducted at a confining pressure of 150 kPa in the same manner as those performed at the 250 kPa confining pressure. Figure 5.9 illustrates the relationship between the microscopic coefficient of friction and the soil's macroscopic internal angle of friction. From Figure 5.9, it is clear that the coefficient of friction and soil internal angle of friction have an almost linear relationship

with each other. Again, the maximum and minimum microscopic coefficient of friction (0.27 and 0.23), which correspond to macroscopic internal angles of friction of 28° and 20°, respectively, are used to conduct the numerical RDC simulations that follow.

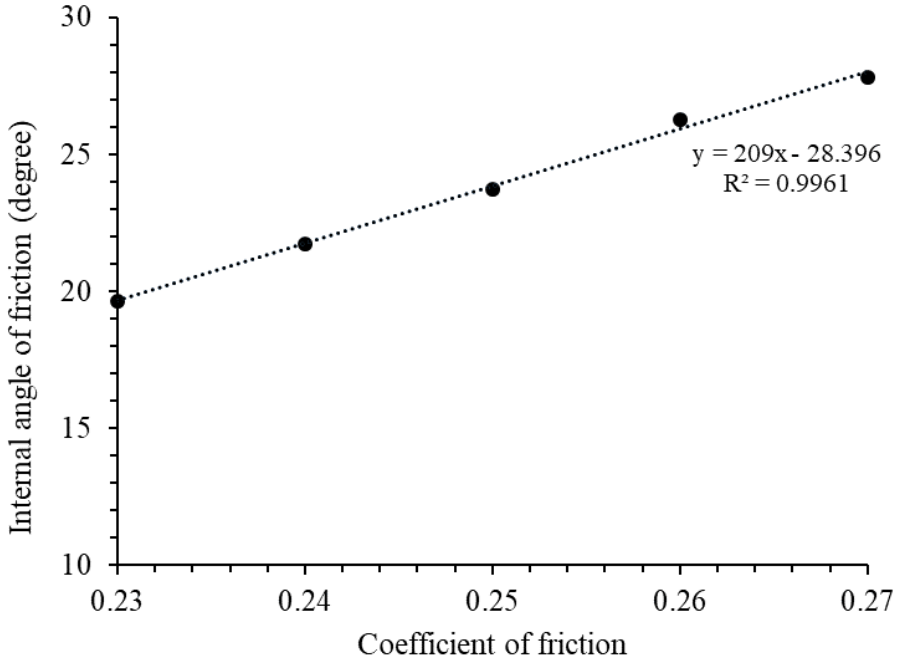

Figure 5.9: The effect of coefficient of friction on soil internal angle of friction.

Table 5.5 presents the matrix of numerical RDC simulations with different ground conditions. In this case, all numerical RDC simulations were conducted at an operating speed of 256 mm/s, which corresponds to a prototype speed of 12 km/h. In total, eight simulations were performed for the 3.64 and 5.46 kg scaled modules at two different normal contact stiffnesses and two different coefficients of friction, with each simulation being carried out up to 10 module passes.

Table 5.5. Simulation matrix for various ground conditions.

Simulation no.	Scale module mass (kg)	DEM microscopic normal contact stiffness (kN/m)	Soil macroscopic initial Young's modulus (MPa)	DEM microscopic coefficient of friction	Soil macroscopic internal angle of friction
9	3.64	450	25	0.25	24°
10	3.64	1050	69	0.25	24°
11	5.46	450	25	0.25	24°
12	5.46	1050	69	0.25	24°
13	3.64	650	52	0.23	20°
14	3.64	650	52	0.27	28°
15	5.46	650	52	0.23	20°
16	5.46	650	52	0.27	28°

5.5.2 Effects of initial Young's modulus and internal angle of friction on soil densification

Plots of soil displacements after ten module passes and the pressures induced by the module at 55 mm depth below the ground obtained from Simulations 9–12 are shown in Figures 5.10 and 5.11. It can be seen that a higher soil's initial Young's modulus results in smaller soil displacements, as one would expect, and increased pressures for both the 3.64 and 5.46 kg modules. In addition, as the soil's initial Young's modulus increases, the soil becomes stiffer and pressure waves are able to be more readily propagated through the soil body, which then results in greater pressure values. Comparing soil displacements and induced pressure values obtained from Simulations 9 and 10, with

those obtained from Simulations 11 and 12, it is clear that, the heavier module produces greater displacements and higher pressures, which is consistent with the conclusion drawn earlier in the paper.

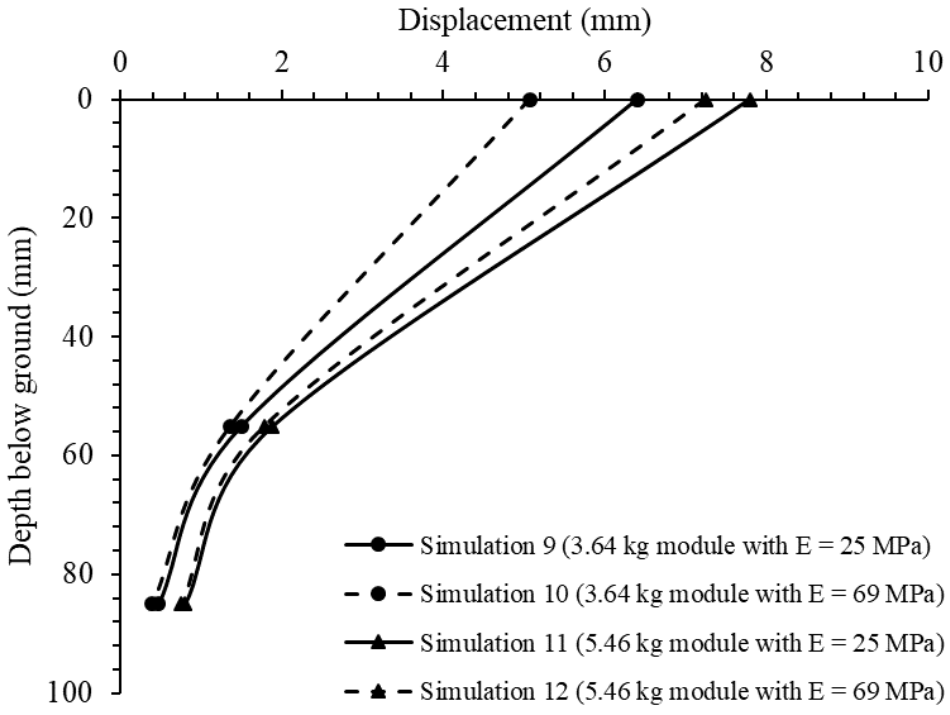

Figure 5.10: The effect of soil initial Young's modulus on soil displacements after 10 module passes.

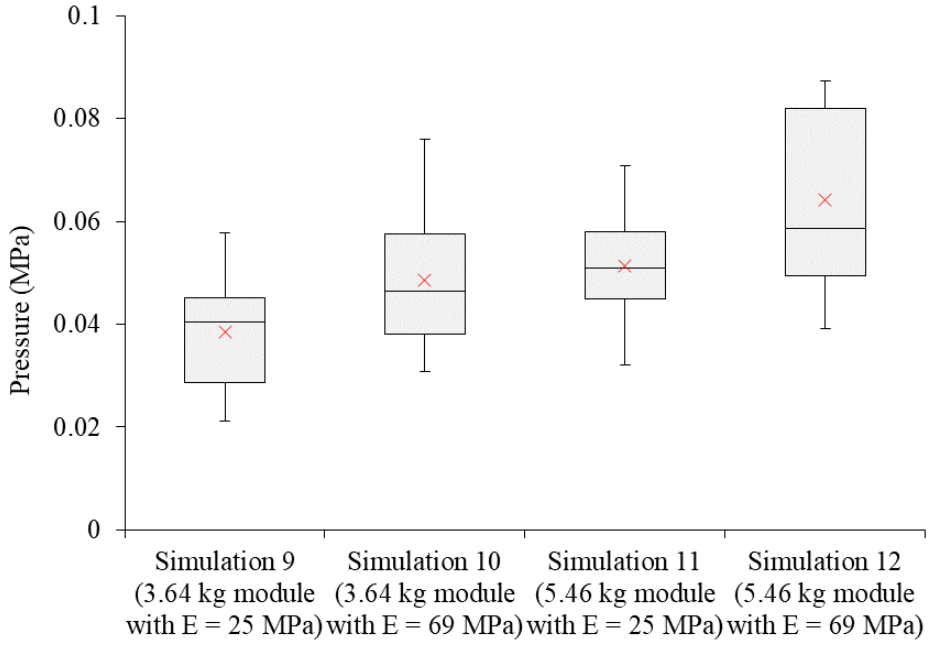

Figure 5.11: The effect of soil initial Young's modulus on the induced pressures at 55 mm depth below the ground.

A similar phenomenon is observed with respect to soil displacements after 10 module passes and pressures at 55 mm depth below the ground from Simulations 13–16, as shown in Figures 5.12 and 5.13. A reduced internal angle of friction results in increased soil displacements and lower pressure values. This is expected, as lower values of internal angle of friction are associated with less dense soil.

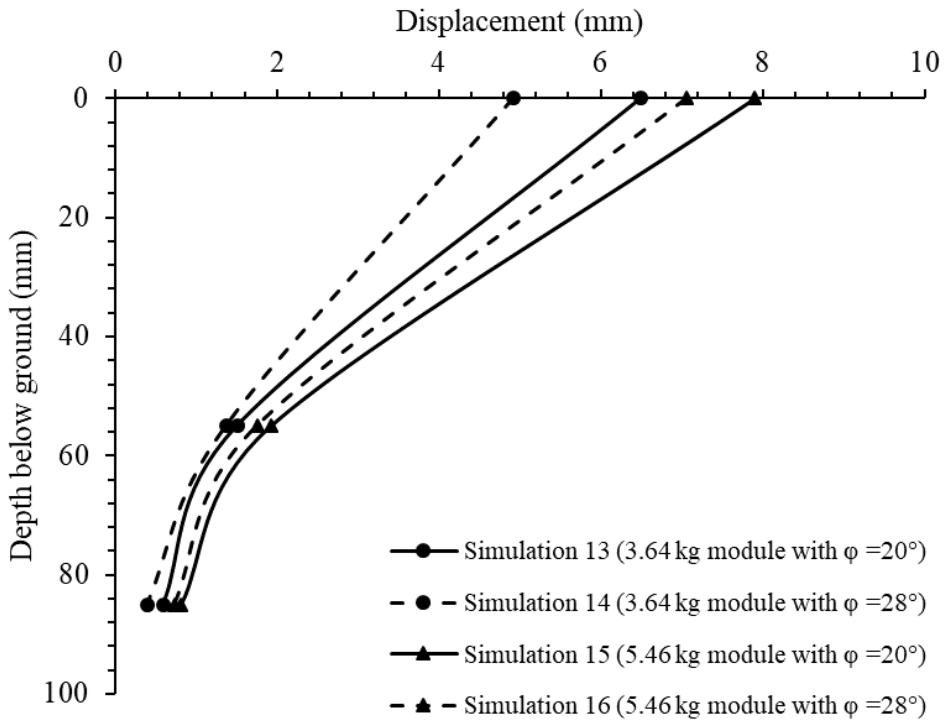

Figure 5.12: The effect of soil internal angle of friction on soil displacements after 10 module passes.

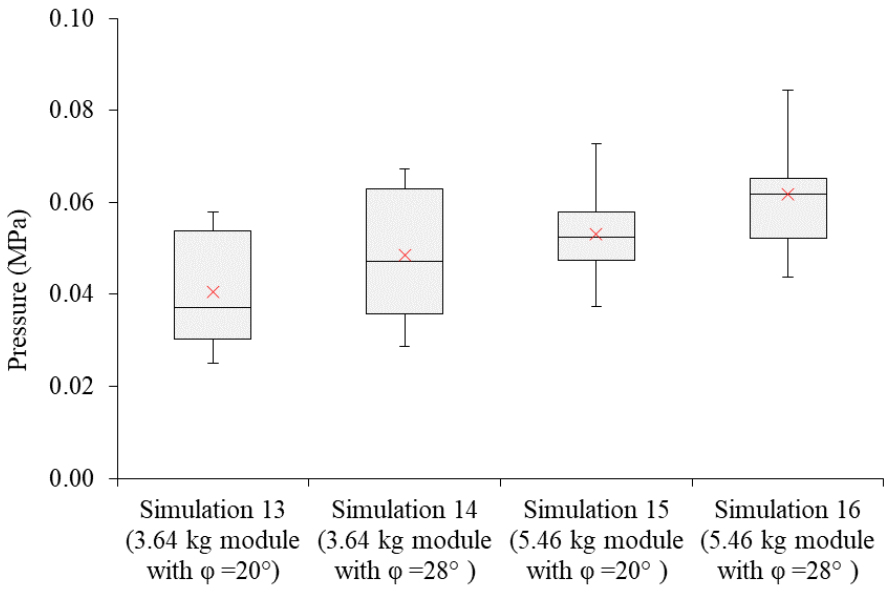

Figure 5.13: The effect of soil internal angle of friction on the induced pressures at 55 mm depth below the ground.

In general, based on the results from Simulations 9 to 16, shown in Figures 5.10 to 5.13, it is evidenced that different soil properties (soil initial Young's modulus and internal angle of friction) can affect the soil response due to the impact roller compaction. A greater soil initial Young's modulus and a higher internal angle of friction decrease soil displacements and increase pressures. In addition, these results further confirm the conclusion that the greater module weight imparts a greater amount of energy to the ground and produces greater soil displacements. It is also worth mentioning that all of the conclusions drawn from this study are based on a limited number of roller passes and a relatively narrow range of soil initial Young's moduli and internal angles of friction. An extensive parametric study on each parameter is encouraged, however, due to time and computational constraints, only a limited number of numerical RDC simulations could be conducted. For reference purposes, one RDC simulation, consisting of 25 passes and approximately 54,000 particles, typically took approximately 30 days to run on the aforementioned supercomputer. Although a limited number of numerical parametric studies have been conducted, the obtained relationships between the microscopic DEM input parameters and the macroscopic soil behaviour are in good agreement with those reported by previous researchers (e.g. Plassiard et al., 2009; Gabrieli et al., 2009; Tapias et al., 2011; Wang and Li, 2014; Marczewska et al., 2016). The results obtained from Simulations 9–16 provide guidance on the performance of RDC in different ground conditions. However, extrapolating data and drawing conclusions beyond the range of these simulations should be treated with caution. Based on the obtained results, it is suggested that the roller is less able to significantly improve stiff soil or soil with greater initial shear strength.

5.6 Summary and conclusions

This paper has examined the effects of module weight, operating speed and different ground conditions on the effectiveness of the 4-sided impact roller using a developed numerical FEM-DEM model. Results of the numerical model were assessed from four aspects, namely the energy imparted to the ground, soil velocity vectors, module imprint lengths and soil displacements at different depths. It was found that the heavier module produces greater ground improvement results in terms of a greater energy delivered to the soil per impact and larger induced soil displacements. The operating speed influences the amount of energy and the manner by which the energy is delivered to the ground. The imparted energy increases with operating speed. The roller module tends to skip on the ground at high operating speeds and in this case, the energy is delivered by the corners rather than the faces of the module. A greater soil initial Young's modulus and a higher internal angle of friction decrease soil displacements and increase pressure readings induced by the roller.

Overall, this study facilitates improved understanding of the factors that affect the effectiveness and application of RDC. It is important to note that, as this numerical model relies heavily on supercomputing facilities, it remains a research, rather than a practical, tool. In addition, the effects of different designs (3- and 5-sided modules) on ground improvement results will be investigated in future work.

5.7 Acknowledgements

The authors wish to acknowledge the computational resources provided by the Phoenix HPC service at the University of Adelaide.

5.8 Funding

This research did not receive any specific grant from funding agencies in the public, commercial, or not-for-profit sectors.

5.9 Compliance with ethical standards

5.9.1 Conflict of interest

The authors declare that they have no conflict of interest.

5.10 References

Altaee, A., Fellenius, B. H., 1994. Physical modeling in sand. *Canadian Geotechnical Journal*, 31, 420-431.

Avalle, D., Carter, J., 2005. Evaluating the improvement from impact rolling on sand. Proc. 6th Int. Conf. on Ground Improvement Techniques, Coimbra, Portugal, 8pp.

Avalle, D. L., Mckenzie, R. W., 2005. Ground improvement of landfill site using the square impact roller. *Australian Geomechanics*. 40, 15-21.

Avalle, D. L., Scott, B. T., Jaksa, M. B. 2009. Ground energy and impact of rolling dynamic compaction e results from research test site. *In: Proceedings of the 17th International Conference on Soil Mechanics and Geotechnical Engineering*, Vol. 3, Alexandria, Egypt, pp. 2228-2231.

Bouazza, A., Avalle, D. L., 2006. Effectiveness of rolling dynamic compaction on an old waste tip. ISSMGE 5th International Congress on Environmental Geotechnics, Cardiff, 1.

Bradley, A. C., Jaksa, M. B., Kuo, Y.-L., 2019. Examining the kinematics and energy of the four-sided impact roller. *Proceedings of the Institution of Civil Engineers - Ground Improvement*. 172, 297-304.

Calvetti, F., Di Prisco, C., Nova, R., 2004. Experimental and numerical analysis of soil–pipe interaction. *Journal of geotechnical and geoenvironmental engineering*. 130, 1292-1299.

Calvetti, F., Viggiani, G., Tamagnini, C., 2003. A numerical investigation of the incremental behavior of granular soils. *Rivista italiana di geotecnica*. 37, 11-29.

Chen, Y., Jaksa, M., Kuo, Y., Scott, B., 2021. Discrete element modelling of the 4-sided impact roller. *Computers and Geotechnics*. Available from https://doi.org/10.1016/j.compgeo.2021.104250.

Clifford, JM. 1980. The development and use of impact rollers in the construction of earthworks in southern Africa. *CSIR Report 373. Pretoria, South Africa: National Institute for Transport and Road Research*.

Coetzee, C., Els, D., 2009. Calibration of granular material parameters for DEM modelling and numerical verification by blade–granular material interaction. *Journal of Terramechanics*. 46, 15-26.

Gabrieli, F., Cola, S., Calvetti, F., 2009. Use of an up-scaled DEM model for analysing the behaviour of a shallow foundation on a model slope. *Geomechanics and Geoengineering: An International Journal*. 4, 109-122.

Jaksa, M. B., Airey, D. W., Scott, B. T., Kuo, Y. L., Ranasinghe, R. A. T. M., Bradley, A. C., Chung, O. Y., Li, Y., Chen, Y., 2019. Quantifying the Effect of Rolling Dynamic Compaction. *Proceedings of the 4th World Congress on Civil, Structural, and Environmental Engineering.* Rome, Italy. doi: 10.11159/icgre19.1.

Jaksa, M. B., Scott, B. T., Mentha, N., Symons, A., Pointon, S., Wrightson, P., Syamsuddin, E., 2012. Quantifying the zone of influence of the impact roller. ISSMGE-TC 211 International Symposium on Ground Improvement IS-GI Brussels, Vol. 2, pp. 41–52.

Kim, K., 2011. Numerical simulation of impact rollers for estimating the influence depth of soil compaction. Dissertation in partial fulfilment of the requirements for the degree of Master of Science, Texas A & M University.

Kozicki, J., Tejchman, J., 2009. Numerical simulations of triaxial test with sand using DEM. *Archives of Hydro-Engineering and Environmental Mechanics*. 56, 149-172.

Kuo, Y., Jaksa, M., Scott, B., Bradley, A., Power, C., Crisp, A., Jiang, J., 2013. Assessing the effectiveness of rolling dynamic compaction. *Proceedings of the 18th International Conference on Soil Mechanics and Geotechnical Engineering*, Paris., pp. 1309–1312.

Li, Y., Airey, D., Jaksa, M., 2020. Evaluating the effective depth of rolling dynamic compaction with a three-sided compactor. *International Journal of Physical Modelling in Geotechnics*. 0, 1-15.

LSTC., 2018. LS-DYNA KEYWORD USER'S MANUAL. Livermore, California: Livermore Software Technology Corporation, ISBN: 0-9778540-2-7.

Marczewska, I., Rojek, J., Kačianauskas, R., 2016. Investigation of the effective elastic parameters in the discrete element model of granular material by the triaxial compression test. *Archives of Civil and Mechanical Engineering*. 16, 64-75.

Plassiard, J.-P., Belheine, N., Donzé, F.-V., 2009. A spherical discrete element model: calibration procedure and incremental response. *Granular Matter*, 11, 293-306.

Scott, B., Jaksa, M., 2008. Quantifying the influence of rolling dynamic compaction. *Proc. 8YGPC*, 199-204.

Scott, B., Jaksa, M., 2014. Evaluating rolling dynamic compaction of fill using CPT. Proceedings of the 3rd International Symposium on Cone Penetration Testing, 941-948.

Scott, B., Jaksa, M., Mitchell, P., 2019. Depth of influence of rolling dynamic compaction. *Proceedings of the Institution of Civil Engineers-Ground Improvement*. 1-10.

Scott, B., Jaksa, M., Syamsuddin, E., 2016. Verification of an impact rolling compaction trial using various in situ testing methods. Proc. of 5th Int. Conf. on Geotechnical and Geophysical Site Characterisation.

Scott, B. T., Jaksa, M. B., Mitchell, P. W., 2020. Influence of towing speed on effectiveness of rolling dynamic compaction. *Journal of Rock Mechanics and Geotechnical Engineering*. 12, 126-134.

Tapias, M. A., Alonso Pérez De Agreda, E., Gili Ripoll, J. A., 2011. Analysis of micro-properties for triaxial behaviour on coarse aggregates using DEM. PARTICLES II: proceedings of the II International Conference on Particle-Based Methods: fundamentals and applications, CIMNE, 550-561.

Wang, X., Li, J., 2014. Simulation of triaxial response of granular materials by modified DEM. *Science China Physics, Mechanics & Astronomy*. 57, 2297-2308.

Chapter 6.

Summary and Conclusions

As described in Chapters 2–5, the ground improvement due to RDC has been investigated by means of physical scale model tests and numerical simulations. This chapter summarises the key findings drawn from Chapters 2–5 and provides research directions for future studies.

6.1 Research Contributions

This research presents a comprehensive study of RDC in terms of physical scale model tests and numerical simulations, which has made important contributions to the current knowledge of RDC. This thesis has provided a greater understanding of the effectiveness of RDC, from some aspects that are difficult to measure using conventional investigation methods, such as, the energy imparted to the ground and soil velocity vectors, but has also demonstrated the significant benefits of combining transparent soils with a numerical FEM-DEM model to quantify the effectiveness of RDC. The research contributions, which have addressed the five objectives of this thesis, are as follows:

1. This research proposed a novel physical scale model to study the soil response using a 1:13 scale, 4-sided impact roller. A series of laboratory tests were performed using transparent soils, high speed photography and the particle image velocimetry technique. The internal soil response due to RDC was captured in real-time and then quantified to help understand how soil reacts to a single roller impact, and behaviour upon subsequent roller passes. The soil internal displacement field obtained from the first roller pass was plotted to reveal the mechanism of particle movement with respect to the roller's motion. It is concluded that, when the roller traverses close to the soil, soil particles are pushed in the direction of the roller's travel and displace downwards. When the roller travels away, the soil is lightly pushed upwards and moves in the opposite

direction of the roller. The displacements of five selected regions of interest were also traced and plotted with respect to the time and motion of the module during the first pass to understand better the soil displacement patterns due to RDC. It is observed that, soil displacements induced by a single roller pass consist of both plastic and elastic components due to the loading and unloading of compactive forces applied by the roller.

2. This research has determined that operating speed influences soil displacements and improvement depth due to the 4-sided impact roller. The vertical displacements of soil at all depths increase as the operating speed increases from 214 to 299 mm/s, corresponding to the full-size RDC speeds of 10 to 14 km/h. When the roller is operated at 342 mm/s, corresponding to the full-size RDC speed of 16 km/h, the soil near the ground surface is pushed upwards and shows significant horizontal displacements in the direction of the roller's motion, and the soil at greater depths has reduced displacements. This is mainly due to the changes of the kinematics of the roller at greater operating speed. At higher operating speeds, for example, at 16 km/h, the roller tends to bounce along the ground from corner to corner, and the compactive force is delivered by the corners rather than the faces of the roller. This results in the soil near the ground surface being ploughed by the corner of the module and not being compacted effectively. The improvement depth increases as the operating speed rises from 214 to 299 mm/s, and it shows no further improvement at speeds greater than 299 mm/s. Two, 1:13 scale models of the 8- and 12-tonne, 4-sided impact rollers were investigated, and it is concluded that, the heavier module induces better ground improvement results in terms of larger horizontal and vertical soil displacements and greater improvement depth for each operating speed.

3. The research has developed a FEM-DEM combined numerical model to analyse the behaviour of soil particles subjected to the 4-sided impact roller. The results obtained from the numerical model are compared against experimental results and the numerical model is shown to be able to simulate ground improvement induced by RDC. Porosities were quantified by placing measurement spheres at regions of interest in the numerical model. Results of the numerical model show that soil movement with respect to the motion of the roller influences porosity changes. When the roller impacts the ground, the soil beneath the roller is compacted by the roller and moves downwards, which results in porosities of these regions decreasing, and the soil in front of and behind the roller is pushed by the roller and displaces upwards; therefore, the porosities increase at these regions. The porosities measured at different depths were plotted with respect to the number of passes to identify the optimum number of passes. It was observed that, the most significant porosity changes occur within the first 30 roller passes and there is no noticeable porosity change after approximately 35 passes. In addition, the maximum porosity changes occur within the top 150 mm depth, and the porosity below this depth is less affected by the roller, since the energy delivered to the ground dissipates with depth.
4. The results of the numerical scale model were upscaled to compare against field data. The comparison between the numerical results and the field measurements was conducted by examining four parameters namely, displacements at the ground surface, and at depths of 0.7 and 1.1 m, pressures measured at 0.7 and 1.1 m depths, the energy delivered to the ground by RDC, and the depth of improvement. The numerical results are in good agreement with the field observations, which suggests that the numerical model provides reasonably reliable predictions of ground improvement due to RDC. This is a significant

contribution to the current knowledge of RDC, since it shows the potential of applying the numerical model in predicting the performance of RDC prior to the application of RDC in practice. Results of the numerical model also suggest that ground settlement as an efficient indicator to determine the optimum number of passes, among several parameters, since it reflects ground improvement induced by RDC and it has a clear relationship with the number of passes. In addition, ground settlement is able to be measured in a more efficient and cost-effective manner in the field.

5. A series of numerical simulations have been conducted to investigate the influence of module mass, operating speed and various ground conditions on the effectiveness of the 4-sided impact roller based on some aspects that are not easy to be measured in the field, such as, the energy imparted to the ground, soil velocity vectors, module imprint lengths and soil displacements at different depths of interest. It is concluded that a heavier roller mass induces greater ground improvement in terms of higher energy delivered to the soil per impact, and larger soil displacements. The energy imparted to the underlying soil by the roller increases with greater operating speed. The rotational dynamics of the roller also change with increasing operating speed, whereby the impacts are delivered by the faces of the roller at typical operating speeds; however, at faster speeds the impacts are delivered towards the corners of the roller and the behaviour is less reproducible. The modelling demonstrates that soil with a higher initial Young's modulus and a higher internal angle of friction decreases the magnitude of soil displacements, which confirms that the impact roller is less able to significantly improve soils that are stiff or have a high initial shear strength.

6.2 Limitations and recommendations for future work

In order to capture and quantify soil internal displacements, transparent soil was adopted in the physical scale model tests. Considering the translucency of the transparent soil, the size of the chamber and the availability of fused quartz sizes, the fused quartz size range was selected to be between 3 and 5 mm. A limited fines proportion in the fused quartz reduces the total number of particles and significantly increases the transparency of the soil. Therefore, the physical scale model tests were limited to a single particle size range. There is a need to test a wider range of particle sizes, for example, soil with different particle size ranges and the same D_{50} value, to investigate the effects of particle size distribution on the effectiveness of RDC. In addition, the soil used in the physical scale model tests is considered as a uniform soil condition, which allows the influence of individual factors on ground improvement due to RDC to be quantified. However, this uniform soil condition seldom occurs in practice; instead, a soil body consists of multiple soil layers with each having distinct properties. It is suggested, in a single physical scale model, to explore the use of different particle sizes to form a transparent soil sample with multiple layers. This is likely to augment the understanding of the effectiveness of RDC in more realistic ground conditions. The refractive index of fused quartz was reported as 1.458 in Chapter 2. The transparency of the soil can be improved by increasing the precision of the refractive index of fused quartz, e.g. the refractive index is 1.4585. In Chapter 2, a plastic vertical displacement of 0.1 mm was adopted to represent the minimum quantifiable soil displacement. The 0.1 mm was selected considering the precision constraints of the adopted *GeoPIV_RG* algorithm. As described by Stanier et al. (2015), the *GeoPIV_RG* algorithm can detect the rigid-body displacement with a precision of approximately 0.001 pixel. In Chapter 2, 0.001 pixel represents approximately 8.33×10^{-4} mm, which is conservatively rounded up to 0.1 mm, allowing for other test uncertainties.

In practice, dynamic compaction, as well as RDC, is best performed on soils with moisture contents at or below the optimum moisture content (Scott et al. 2012). However, in the present study, fused quartz is required to be fully saturated in order to achieve sample transparency. According to Pak et al. (2005), dynamic compaction is effective on saturated soils if the soil is free draining, since the porewater has low compressibility when compared with the soil skeleton. In the physical scale model tests, drainage occurs at the top surface to facilitate soil compaction. In addition, the viscosity of the selected pore fluid (STSI solution) is relatively low, which is comparable to that of water (Carvalho et al. 2015). Furthermore, completely dry fused quartz was used to conduct further physical scale model tests to quantify the effect of pore fluid on RDC compaction. Since dry fused quartz is opaque, it is not possible to track internal soil displacements. Instead, the surface settlement was adopted to compare the compactive effects of the saturated and dry fused quartz. The 3.64 kg module was operated at two speeds, 256 and 299 mm/s and a 3D surface scanner was used to scan the ground surface after every 10 passes of the module. The results showed that the dry fused quartz exhibited greater surface settlements, however, the maximum differences between the surface settlement of the saturated and dry fused quartz induced by the module travelling at 256 and 299 mm/s speeds (after 40 passes) were 11.2% and 8.9%, respectively. It can be seen that ground settlements obtained from dry fused quartz tests are similar to those measured from saturated fused quartz tests. Given only the ground settlement was investigated, more in-depth studies are needed to investigate the effect of pore fluid on compaction in terms of quantifying effective stress, shear strain, permeability and other geotechnical properties of dry and saturated fused quartz particles.

As stated in Section 2.2.2, the chamber was tipped for testing. However, depositing soil in this way may result in the sample having a directional distribution of stresses, which

depends on the orientation of the deposited layers with respect to the direction of the gravity and applied stresses. To minimise this issue, the chamber was carefully tipped and the soil sample was allowed to age for at least 24 hours after rotation. Since the chamber was constructed with two detachable panels at its front and top sides, the chamber was only allowed to be tipped in one direction for testing. In future research, it is suggested that the chamber be reconstructed with three detachable panels at its front, top and bottom sides, so the chamber can be tipped in other directions to quantify the effect of deposition direction of fused quartz. In addition, advanced equipment may be adopted in future studies, for example, a powerful laser can be used to illuminate the targeted plane to generate a speckled pattern without tipping the chamber. This was trialled early in the research program, but limited success was achieved with the lasers adopted.

In the numerical simulations, the linear contact model developed by Cundall and Strack (1979) was adopted to simulate contact forces between soil particles. This contact model was used as it is simple, efficient and has been successfully adopted by others. Further research could explore other contact models to simulate soil behaviour, and compare the obtained numerical results with those measured in field tests to achieve better simulation of the soil. In addition, the effect of the particle size distribution curve on the formation of force chains needs to be further investigated.

The physical scale model tests and numerical simulations conducted in this thesis were limited to the use of the 4-sided impact roller. However, as mentioned in Chapter 1, there are three different module shape designs of RDC (3, 4, and 5 sides). It is suggested to investigate the performance of impact rollers with different numbers of sides, and also assess the effects of operating speed, module mass and the number of passes on ground improvement induced by the 3- and 5-sided rollers. A comparison of different module

shapes is also recommended to provide a better understanding of the similarities and differences between them. This will provide a significant contribution to the current knowledge of RDC and may benefit the ground improvement industry, since there is significant potential to optimise the design of the roller in the future to achieve better efficacy of RDC.

The energy delivered to the ground is a direct indicator of the effectiveness of RDC since soil compaction is achieved by the compactive energy, and RDC is able to deliver greater energies to the ground compared with conventional static or vibratory rollers. The numerical model has been shown to be able to predict the energy delivered to the ground by a single roller impact. The energy delivered to the ground per impact has been shown to relate to the depth of improvement in previous research studies. However, there is still very limited understanding regarding how compactive energy is transmitted in the soil body and the relationship between energy dissipation and soil displacement patterns. It is suggested to explore the energy transmission within the soil under the roller based on the current proposed numerical model. In addition, there is a need to quantify the proportion of delivered energy used to induce soil displacements, the energy stored in the contacts between particles and the energy dissipated through the interactions between soil particles. The efficiency of RDC (energy causing densification of the soil divided by the total energy imparted by the roller) can be then calculated. In addition, the effects of operating speed, module mass and module shape on the efficiency of RDC can also be explored in the future.